2011

Measurement of the differential cross-section with respect to momentum and rapidity of the J/psi meson and the non-prompt J/psi cross-section fraction in pp collisions at sqrt(s)=7 TeV with the ATLAS detector

Andrew Nelson
Iowa State University

Measurement of the differential cross-section with respect to momentum and rapidity of the J/ψ meson and the non-prompt J/ψ cross-section fraction in pp collisions at $\sqrt{s}$=7 TeV with the ATLAS detector

by

Andrew James Nelson

A dissertation submitted to the graduate faculty

in partial fulfillment of the requirements for the degree of

DOCTOR OF PHILOSOPHY

Major: High Energy Physics

Program of Study Committee:

Sören Prell, Major Professor

James Cochran

Mani Mina

Craig Ogilvie

German Valencia

Iowa State University

Ames, Iowa

2011

TABLE OF CONTENTS

LIST OF TABLES

LIST OF FIGURES

ABSTRACT

The inclusive production of the J/ψ resonance is studied with the ATLAS detector in LHC proton-proton collisions at $\sqrt{s} = 7$ TeV using the J/ψ decay mode to two muons. Using the first 2.3 pb^{-1} of data, two related physics measurements are performed: the double-differential production cross section with respect to the transverse momentum and rapidity of the J/ψ, and the fraction of J/ψ mesons produced from b hadron decays with respect to the J/ψ transverse momentum and rapidity. These two measurements are combined to produce the prompt and non-prompt J/ψ cross-sections.

CHAPTER 1. Overview

The J/ψ meson is made of two charm quarks. The J/ψ's mass places its production mechanism at the boundary between perturbative and non-perturbative QCD (quantum chromodynamics). Non-perturbative QCD is still not well understood, particularly in hadron collisions. The Large Hadron Collider (LHC), built in the old Large Electron Positron (LEP) accelerator tunnel, started colliding proton-proton bunches at the end of 2009. While the primary goal of the LHC is to find evidence of the Higgs boson, its two general purpose detectors (ATLAS and CMS) have a wide physics program. We present two measurements on J/ψ production in proton-proton collisions at a new energy level using the ATLAS detector.

The first measurement we present is the inclusive differential cross-section for producing a J/ψ meson in pp collisions with respect to its transverse momentum and direction with respect to the beam line. In general, the inclusive differential cross-section of the J/ψ meson with respect to the variables x and y is defined as $\frac{d^2\sigma}{dxdy} = \frac{N_{J/\psi}}{\mathcal{L}\Delta x\Delta y}$, where $N_{J/\psi}$ is the number of produced J/ψ; $\mathcal{L}$ is the luminosity, a measure of beam intensity, which is the number of protons passing through the colliding area of the proton beams; and Δx (Δy) is the size of the bin in the variable x (y). "Inclusive" here means we measure all J/ψ, regardless of how they are produced and "differential" means that the measurement is done with respect to certain variables. The total cross-section is related to the differential cross-section according to the equation $\sigma = \int dxdy \frac{d^2\sigma}{dxdy}$.

The J/ψ meson can be produced promptly in two ways: directly in the proton-proton collision through the strong interaction and indirectly through strong or electromagnetic decays of higher-energy states composed of two charm quarks. The J/ψ meson can also be produced non-promptly through weak decays of b hadrons. The second measurement we present is the fraction of J/ψ mesons produced non-promptly, $\mathcal{R}$. The b-hadron lifetime is long enough that

the distance from its creation in the proton-proton collision to the b-hadron decay point can be measured. We distinguish between J/ψ mesons produced non-promptly and promptly by reconstructing the decay vertex of the b hadron and determining its distance from the collision point.

This thesis is organized as follows. Chapter 2 continues a short review of the theoretical framework of particle physics in general, and J/ψ production in particular. Chapter 3 has a brief description of the LHC accelerator complex, and an overview of the ATLAS detector. Chapter 4 goes into more detail about the Pixel detector, which is crucial for the vertexing used in the measurement of the non-prompt to inclusive J/ψ fraction. Chapter 5 details the inclusive cross-section analysis, and chapter 6 details the ratio measurement. In chapter 7 we present our conclusions, and give an outlook on future related measurements.

CHAPTER 2. Theory

The Standard Model accurately describes all of the observed phenomena known to modern elementary particle physics. It describes three of the four fundamental forces (gravity is left out): the strong, the weak, and the electromagnetic. The Standard Model uses these forces, along with a small number of fundamental particles to describe the production of and the interactions between hundreds of compound particles observed at particle accelerators. One of these particles is the J/ψ, which was discovered in 1974 [1]. Even though it was discovered more than thirty years ago, the mechanism of its production in hadron collisions is still not well understood. By varying the J/ψ production parameters, such as the beam energy, more can be learned about the J/ψ production mechanism.

2.1 Standard Model

The Standard Model is the theory of the strong, weak, and electromagnetic forces. It is the most successful description of matter at the subatomic scale. Every fundamental particle is either a boson or a fermion; fermions have spin with odd multiples of $\frac{1}{2}$, and bosons have integer spin. The symmetry group of the Standard Model is $\mathrm{SU(3)}_{\mathrm{color}} \otimes \mathrm{SU(2)}_L \otimes \mathrm{U(1)}_Y$. The $\mathrm{SU(2)}_L \otimes \mathrm{U(1)}_Y$ symmetry group describes the unification of the electromagnetic and weak forces, and $\mathrm{SU(3)}_{\mathrm{color}}$ describes the strong force [2].

Fermions have either left or right handed helicity; the left handed ones are represented by doublets in the weak isospin space $\mathrm{SU(2)}_L$, like $\binom{\nu_e}{e}_L$ and $\binom{u}{d}_L$, and the right handed by singlets, like $(e)_R$ and $(u)_R$. There are two types of fundamental fermions: quarks and leptons. The quarks make up strongly-bound particles, called hadrons, like the proton and neutron, and interact via all three forces. The leptons interact electromagnetically and weakly, but not

Table 2.1 Standard model fermions [4].

	Flavor	Symbol	Charge	Mass (GeV)
First Generation				
Lepton	Electron	ν_e	0	$< 2 \times 10^{-9}$
		e^-	-1	0.511×10^{-3}
Quark	up	u	$\frac{2}{3}$	$2.6^{+0.8}_{-1.1} \times 10^{-3}$
	down	d	$-\frac{1}{3}$	$5.0^{+1.0}_{-1.5} \times 10^{-3}$
Second Generation				
Lepton	Muon	ν_μ	0	$< 0.19 \times 10^{-3}$
		μ^-	-1	0.106
Quark	charm	c	$\frac{2}{3}$	$1.27^{+0.07}_{-0.11}$
	strange	s	$-\frac{1}{3}$	$0.104^{+0.026}_{-0.034}$
Third Generation				
Lepton	Tau	ν_τ	0	$< 18.2 \times 10^{-3}$
		τ^-	-1	1.78
Quark	top	t	$\frac{2}{3}$	171 ± 2
	bottom	b	$-\frac{1}{3}$	$4.20^{+0.17}_{-0.07}$

strongly. The only stable charged lepton is the electron, which pairs up with protons and neutrons to make atoms. There are three generations of fermions, and each one has identical properties, except that the masses are increased. The fermion properties are summarized in Table 2.1. Note that for each lepton generation there are two particles: the charged lepton and the neutral lepton. The neutral leptons are called neutrinos. The charges given in the table are for the particles. For each particle there is an oppositely charged antiparticle (e.g. antielectron, antitau). [1]

Standard Model bosons mediate interactions between the fermions and each other. The symmetry groups of the Standard Model were already mentioned, and each generator of the symmetry group gets a massless force carrying field. The number of generators for a special unitary symmetry of N dimensions, SU(N), is $N^2 - 1$. $\mathrm{SU(3)_{color}}$ symmetry generates the strong force, so that there are $3^2 - 1 = 8$ strong force bosons, collectively called gluons. For the electroweak force, the $\mathrm{SU(2)}_L \otimes \mathrm{U(1)}_Y$ generates 4 massless force fields ($2^2 - 1 = 3$ and 1). However, three of the electroweak bosons are massive through a process called spontaneous symmetry breaking, in which the $\mathrm{SU(2)}_L \otimes \mathrm{U(1)}_Y$ symmetry is broken by the Higgs potential.

[1] Precisely, antiparticles have the opposite-sign values of all additive quantum numbers.

Table 2.2 Standard Model bosons [4].

Name	Symbol	Charge	Mass (GeV)
photon	γ	0	0
gluon	g	0	0
$W^{\pm}$	$W^{\pm}$	± 1	80.398 ± 0.025
Z	Z	0	91.1876 ± 0.0021

This generates three massive bosons (the $W^{\pm}$ and Z bosons), one massless boson (the photon), and at least one massive Higgs particle. The Higgs particle is a prediction of the Standard Model, but it has not yet been observed. The boson properties are summarized in Table 2.2 [3].

2.1.1 Quantum Chromodynamics

Quantum Chromodynamics, or QCD, is the mathematical formulation of the strong force - the force mainly responsible for J/ψ production in hadron collisions. The strong charge is called color. Each quark has color: either red, green, or blue. The strong force carrier, the gluon, has a combination of a color and anticolor. The strength of the strong force does not decrease as the distance increases, and separating two colored particles would take an infinite amount of energy. If a colored final state existed, it would pull gluons out of the vacuum until it was color neutral. This property of the strong force is called color confinement. Therefore, observable states, such as composite particles, must be color neutral (a color "singlet").

Neutral color states, also known as color singlet states, can exist in two configurations. First, a color could be "canceled" with an antiparticle of the same color, e.g. a red charm quark with an antired charm antiquark. Such a state is called a meson; the lightest meson is the pion and other examples include the J/ψ meson ($c\bar{c}$), the Υ meson ($b\bar{b}$), the K^+ ($u\bar{s}$), and the K^- ($\bar{u}s$). Second, three different colored quarks could be combined in a single state (analogous to optical theory, where red+green+blue=white). States of three quarks are called baryons. Examples are the proton and neutron, which make up the nuclei of ordinary matter. Other exotic hadrons are predicted by QCD such as the pentaquark, made of a color-anticolor quark pair and three quarks of color red, green, and blue; glueballs, made of only gluons; and the tetraquark, made of two quark-antiquark pairs. However, only baryons and mesons have been observed.

An important feature of the strong force (called asymptotic freedom), is that the force gets weaker at higher energies. On the other hand, the strong force becomes very strong at low energy. Mathematically, the strong coupling constant scales according to equation 2.1, where Q^2 is the momentum transfer squared between the interacting particles:

$$\alpha_s(Q^2) = \frac{2\pi}{\beta \ln(\frac{Q^2}{\Lambda^2_{\rm QCD}})}. \tag{2.1}$$

$\Lambda_{\rm QCD}$ is the QCD energy scale, approximately 200 MeV, and β is $11 - \frac{2}{3}n_f$, where n_f is the number of quark flavors (currently six are known) [2, 3].

For example, at an interaction energy of 1 GeV, $\alpha_s \approx 0.4$. For comparison, the electromagnetic coupling constant is $\alpha \approx \frac{1}{137}$. As a consequence of asymptotic freedom QCD can be calculated perturbatively for sufficiently high energy, but at low energy no perturbative calculation can be made. Even at 1 GeV, where QCD can be calculated perturbatively (in principle), the QCD perturbative series will converge much more slowly than the comparable electromagnetic perturbative calculation.

2.2 Charmonium

The meson comprising a charm and anticharm quark is called charmonium. Depending on the angular momentum state of the quark pair, charmonium states have different mass, due to hyperfine splitting. Charmonium states can be described using spectroscopic notation $n^{2S+1}L_J$, where n is the principal quantum number, S the total spin, L the orbital angular momentum, and J the total angular momentum of the charmonium system. Different angular momentum states give the charmonium different parity. Charge parity (the parity under charge inversion) is given by $C = (-1)^{L+S}$, and parity under spatial coordinate inversion is given by $P = (-1)^{L+1}$. The lowest mass charmonium states each have $L = 0$, and are the η_c and J/ψ mesons; they form a hyperfine doublet. Their quantum states are 1^1S_0 and 1^3S_1, respectively.

The different charmonium properties are summarized in Table 2.3. The heavier charmonium states can decay into the J/ψ meson by emitting photons or pions, and contribute to the inclusive J/ψ production, as seen in Figure 2.1. This process is called feed-down. In particular, the $\psi(2S)$ state has the same angular momentum quantum numbers as the J/ψ, but at a higher

Table 2.3 Properties of charmonium states [4].

Particle	$n^{2S+1}L_J$	Mass (GeV)	Width (MeV)
η_c	1^1S_0	2.980 ± 0.001	26.7 ± 3.0
J/ψ	1^3S_1	3.09692 ± 0.00001	0.0932 ± 0.0021
χ_{c0}	1^3P_0	3.4148 ± 0.0003	10.2 ± 0.7
χ_{c1}	1^3P_1	3.51066 ± 0.00007	0.89 ± 0.05
χ_{c2}	1^3P_2	3.55620 ± 0.00009	2.03 ± 0.12
h_c	1^1P_1	3.5259 ± 0.0003	< 1
$\psi(2S)$	2^3S_1	3.68609 ± 0.00004	0.317 ± 0.009

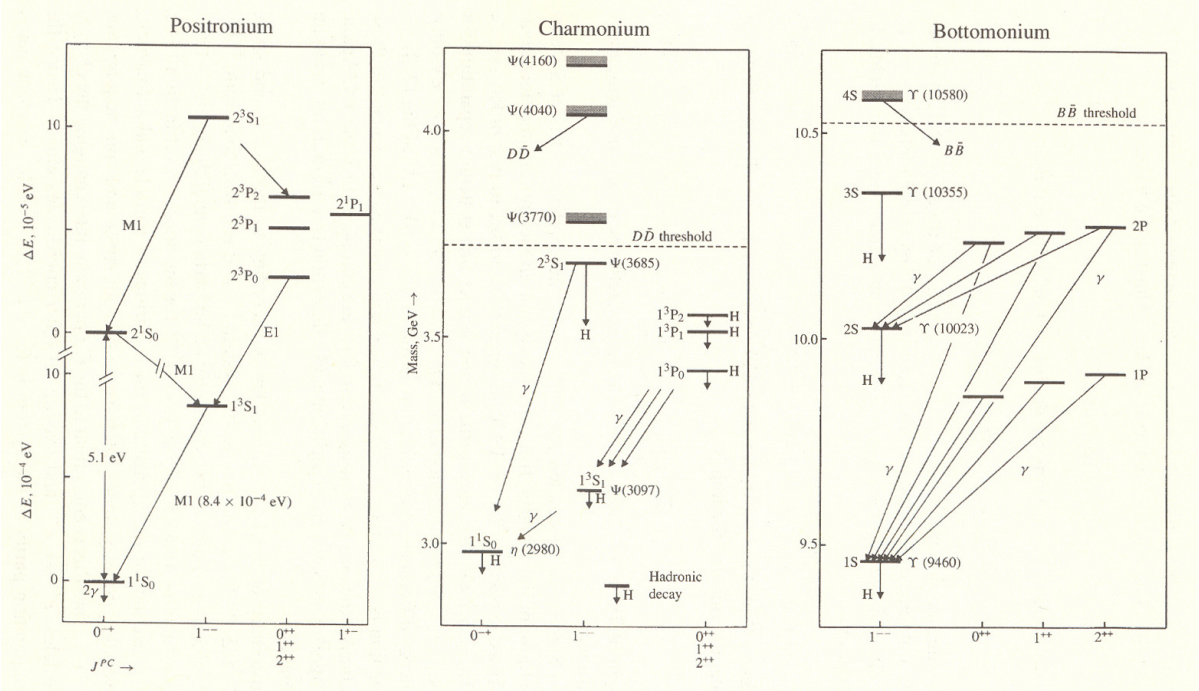

Figure 2.1 Charmonium states and their decay channels, compared to Positronium (electron bound state) and Bottomonium (bottom quark bound state) [5].

principal quantum number (2^3S_1). The $\psi(2S)$ decays into a J/ψ meson $57.4 \pm 0.9\%$ of the time, but it also decays into two muons $0.75 \pm 0.08\%$ of the time [4].

2.3 J/ψ Production and Decay

The J/ψ meson can be produced promptly either directly in the proton-proton collisions, or indirectly through the decay of higher mass charmonium states, and non-promptly through the weak decay of b hadrons. The proton has three valence quarks (two up and one down), but

along with these, there are many particle and antiparticle pairs being created and annihilated, as allowed by the Heisenberg uncertainty relations. The probability for a given quark to exist in the proton at a certain momentum is called the "parton distribution function." At low proton-proton collision energy, quark-antiquark annihilation dominantly contributes to J/ψ production, but at higher energies the number of gluons in the proton increases, and at the energies of the LHC gluon-gluon fusion is the dominant mechanism.

The measurement of the J/ψ cross-section by CDF at $\sqrt{s} = 1.8$ TeV found a much higher value than expected by the leading order terms of the Color Singlet Model (CSM) [6], shown in Figure 2.2. Afterwards, other models were created or revived to explain the cross-section, but so far none have been able to reproduce the experimental measurements of both J/ψ cross-section and polarization. However, the Color Octet Model (COM) predicts the magnitude of the cross-section quite well, as measured by the PHENIX Collaboration [7], for example. In this section we will briefly cover J/ψ decay, the three main models for J/ψ prompt production, and the model for J/ψ non-prompt production [8].

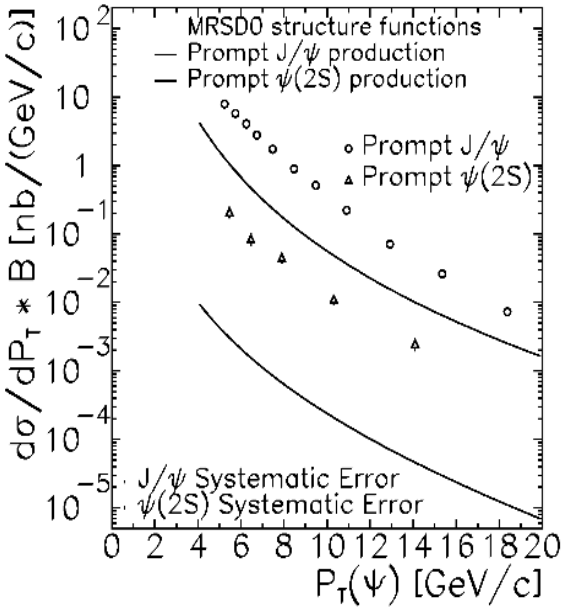

Figure 2.2 Differential cross-section times branching ratio for prompt J/ψ and $\psi(2S)$ mesons from the CDF experiment. Error bars are statistical and systematic uncertainties added in quadrature. Circles are J/ψ, triangles are $\psi(2S)$, and lines are theoretical predictions from the CSM [6].

2.3.1 Color Evaporation Model

The Color Evaporation Model (CEM) was the earliest model for charmonium production. It assumes that the color state of the $c\bar{c}$ pair is randomized by soft interactions after its initial production, so that the probability of the pair eventually reaching a color singlet state is $\frac{1}{9}$. The model allows the charm quark pair to be produced in any color state by the hard, perturbative process. The total charmonium cross-section is given by [9, 10]

$$\sigma_{c\bar{c}} = \frac{1}{9}\int_{2m_c}^{2m_D} dm \frac{d\sigma_{c\bar{c}}}{dm}, \tag{2.2}$$

where m_c and m_D are the charm quark mass and D meson mass, respectively. The cross-section for any given charmonium state, for example the J/ψ, is determined by a factor $\rho_{J/\psi}$:

$$\sigma_{J/\psi} = \rho_{J/\psi}\sigma_{c\bar{c}}. \tag{2.3}$$

The natural value of the ρ factor is the inverse of the number of charmonium states between $2m_c$ and $2m_D$, which can be further refined by considering other factors, such as spin multiplicity [9, 10, 11]. For example $\rho_{J/\psi}$ can be replaced by $\frac{\Gamma_{J/\psi}}{\sum_i \Gamma_i}$, where the sum is over the charmonium states between $2m_c$ and $2m_D$. $\Gamma_i = \frac{2J_i+1}{n_i}$ is a proportionality factor, where J_i is the total angular momentum, and n_i is the principal quantum number of the charmonium state [10]. The Next-to-Leading-Order (NLO) QCD perturbative prediction and the prediction using PYTHIA Monte Carlo are used for the CEM calculation, and the CEM prediction is compared with the prompt cross-sections from CDF and D0, as shown in Figure 2.3, where p_T is the transverse momentum of the J/ψ.

2.3.2 Color Singlet Model

The Color Singlet Model (CSM) takes into account the final state of the $c\bar{c}$ pair. In this model the two charm quark system is required to be produced with the same quantum numbers as the J/ψ: $^3S_1$ spin state and the color singlet state. Consequently, diagrams where a J/ψ meson is produced by a single gluon are no longer possible due to color conservation. The model factorizes the production into a hard relativistic part, described perturbatively, and a soft part, described by a universal wave function, which represents the probability for the

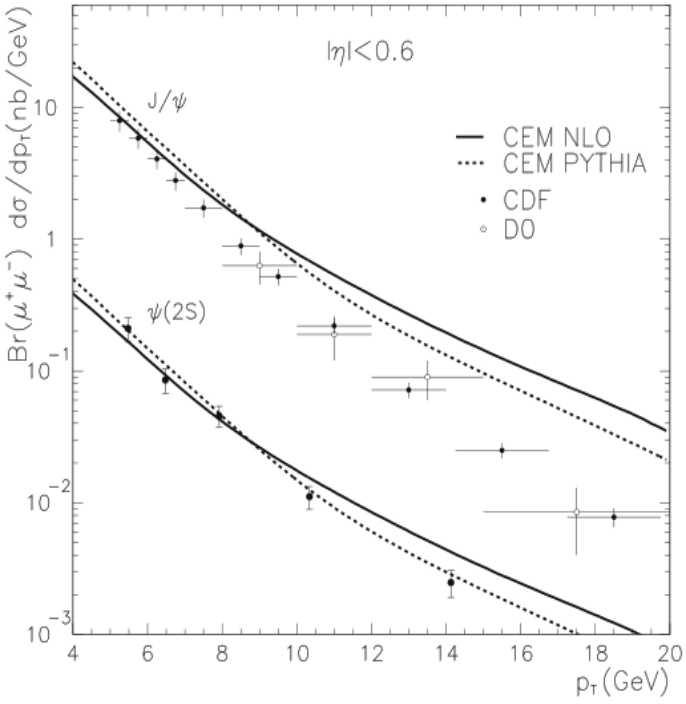

Figure 2.3 Comparison of prompt J/ψ and $\psi(2S)$ p_T differential cross-sections from CDF [12, 13, 14] and D0 [15] with results from the CEM added to NLO matrix elements and PYTHIA Monte Carlo [9].

two charm quarks to form the J/ψ bound state. The model assumes the two charm quarks are produced on-shell by the perturbative hard process, and at rest in the meson reference frame (this assumption is called the static approximation). The justification for the static approximation is that the universal wave function, which represents the probability for the two charm quarks to form a bound state, should be strongly peaked at the origin. The only input to this model, apart from the parton distribution functions, is the universal wave function, which can be determined from data or calculated using potential models [10].

Given the static approximation, the amplitude to produce a J/ψ is [10]

$$\mathcal{A} = \int \Phi(\vec{p})\mathcal{M}(p)\delta(2p^0)dp \approx \mathcal{M}(0)\Psi(0). \tag{2.4}$$

Here p is the relative momentum between the two charm quarks, $\mathcal{M}$ is the perturbative matrix element, and Ψ and Φ are the Schrödinger wave function for the $^3S_1$ state in coordinate and momentum space, respectively. The static approximation allows us to take the first non-vanishing term of the amplitude, in order to derive the final form. For S-wave states, this

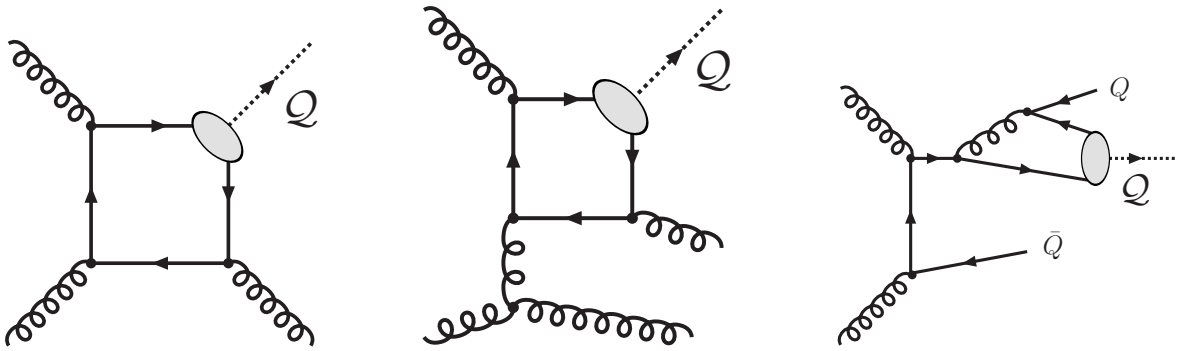

(a) Leading Order CSM Feynman diagram, scales like p_T^{-8}.

(b) NLO CSM Feynman diagram, scales like p_T^{-6}.

(c) NLO CSM Feynman diagram, scales like p_T^{-4}.

Figure 2.4 Representative Feynman diagrams for the CSM up to NLO. $\mathcal{Q}$ represents the $c\bar{c}$ state, and Q represents the charm quark [8].

means the value of the wave function at the origin, while for P-wave states, the first non-vanishing term is $\Psi'(0)$. The $\Psi(0)$ term is non-perturbative, but it is determined from the leptonic decay width, where it is also present.

The full Next-to-Leading-Order (NLO) calculation of the CSM is available, as well as a partially completed Next-to-Next-to-Leading-Order (NNLO*) calculation [69, 70]. In the proton-proton collisions at the LHC, where the leading contribution to the CSM comes from gluon-gluon fusion, the leading order Feynman diagrams are of the type shown in Figure 2.4(a). At leading order, the differential cross-section as a function of p_T scales like p_T^{-8} [16]. However, the NLO contributions add diagrams like those shown in Figures 2.4(b) and 2.4(c) that scale like p_T^{-6} and p_T^{-4} [8], respectively. Therefore, for sufficiently large values of p_T, the NLO terms will dominate over the LO terms.

2.3.3 Color Octet Model

The Color Octet Model (COM) also factorizes the J/ψ production into hard and soft parts, but it does not assume that the charm quarks are produced in their final spin and color state. Since the charm quark mass is about 1 GeV, and the QCD energy scale, Λ_{QCD}, is about 200 MeV, the COM models J/ψ production non-relativistically. The COM systematically expands the cross-section into terms of the charmed quark velocity (in the meson rest frame, $v_c^2 \approx 0.23c^2$) within the framework of Non-Relativistic Quantum Chromodynamics (NRQCD) [17].

Combining both of these ideas and expanding the cross-section into a sum over powers of α_s and velocity, the cross-section can be written as follows

$$d\sigma(J/\psi + X) = \sum_{S,L,J,\text{color}} d\hat{\sigma}(c\bar{c}[^{2S+1}L_J^{(1,8)}] + X)\langle \mathcal{O}^{J/\psi}[^{2S+1}L_J^{(1,8)}]\rangle. \tag{2.5}$$

S, L, and J are the spin, orbital angular momentum, and total angular momentum of the charmonium state, and the superscripts (1) and (8) indicate the color state of the quark pair. The sum is over S, L, J, and color. The Long Distance Matrix Elements (LDME) $\langle \mathcal{O}^{J/\psi}[^{2S+1}L_J^{(1,8)}]\rangle$ represent the probability for the quark pair in a particular spin and color state to transition into a J/ψ [10].

The LDME are proportional to the charmed quark velocity; the dependence can be determined from power counting rules applied to the operator $\mathcal{O}^{J/\psi}$ [18]:

$$\langle \mathcal{O}^{J/\psi}[^{2S+1}L_J^{(1,8)}]\rangle \propto v^{3+2L+2E+4M}, \tag{2.6}$$

where E and M are the minimum number of successive chromoelectric and chromomagnetic transitions for the $c\bar{c}$ to go from the $[^{2S+1}L_J^{(1,8)}]$ state to the J/ψ state.

As shown above, more transitions to reach the J/ψ state suppress the contribution by factors of v_c^2. This allows us to truncate the summation of quantum states. The four leading terms in v_c are kept: the color singlet state with the same quantum numbers as the J/ψ, $^3S_1^{(1)}$, and the three color octet states, $^1S_0^{(8)}$, $^3P_0^{(8)}$, and $^3S_1^{(8)}$. The color singlet LDME is determined from the leptonic decay width, in a manner similar to the determination of the universal wave function of the CSM, while the three color octet state LDME must be determined from a fit to the cross-section data [10].

Representative diagrams for the COM are shown in Figures 2.5(a) and 2.5(b). The COM includes diagrams with a similar topology to CSM, but at a lower order of α_s (compare the NNLO CSM diagram in Figure 2.5(c) with the LO COM diagram in Figure 2.5(a)). Therefore, at leading order, the COM already includes diagrams which scale as p_T^{-6} and p_T^{-4}, which don't appear in the CSM until NLO [8]. Since these diagrams will dominate for sufficiently high p_T, the COM can describe the cross-section better at high p_T at any given order.

The COM is able to reproduce the production cross-section quite well, as shown in Figure 2.6. However, it strongly disagrees with the measured polarization, as shown in Figure 2.7.

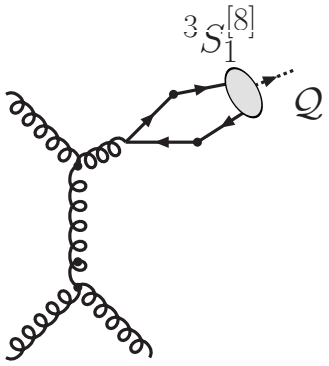

(a) Leading order COM Feynman diagram, scales like p_T^{-4}.

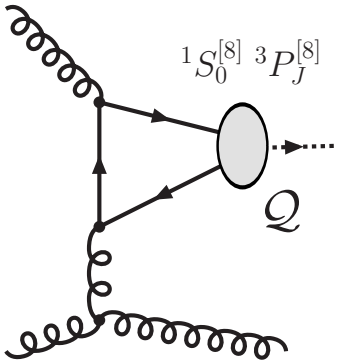

(b) Leading order COM Feynman diagram, scales like p_T^{-6}.

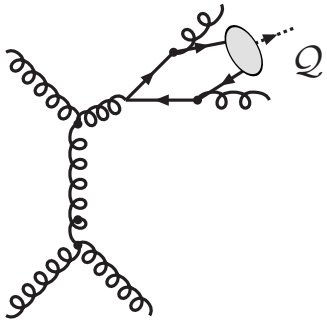

(c) NNLO CSM Feynman diagram, scales like p_T^{-4}.

Figure 2.5 Representative Feynman diagrams for the COM up to LO, and a representative CSM NNLO diagram. $\mathcal{Q}$ represents the $c\bar{c}$ state [8].

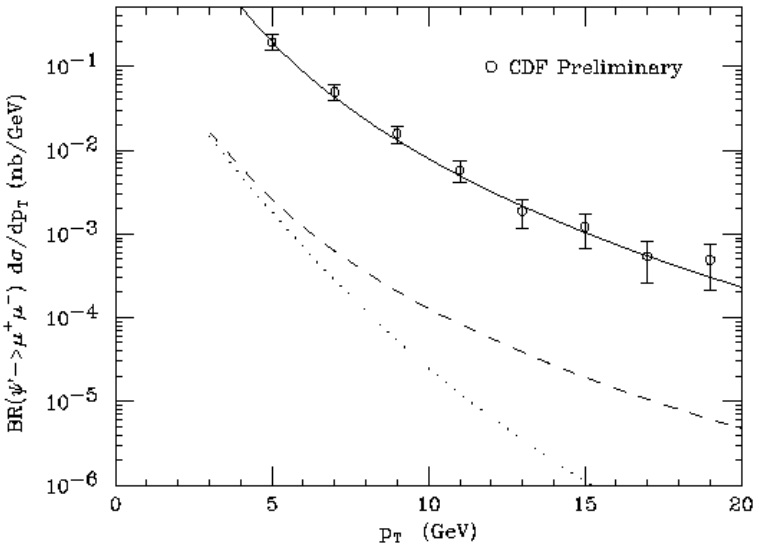

Figure 2.6 CDF data [19] for prompt $\psi(2S)$ differential cross-section versus p_T compared to theoretical calculations for the LO CSM (dotted), LO plus fragmentation (dashed), and COM fragmentation (solid line) [20].

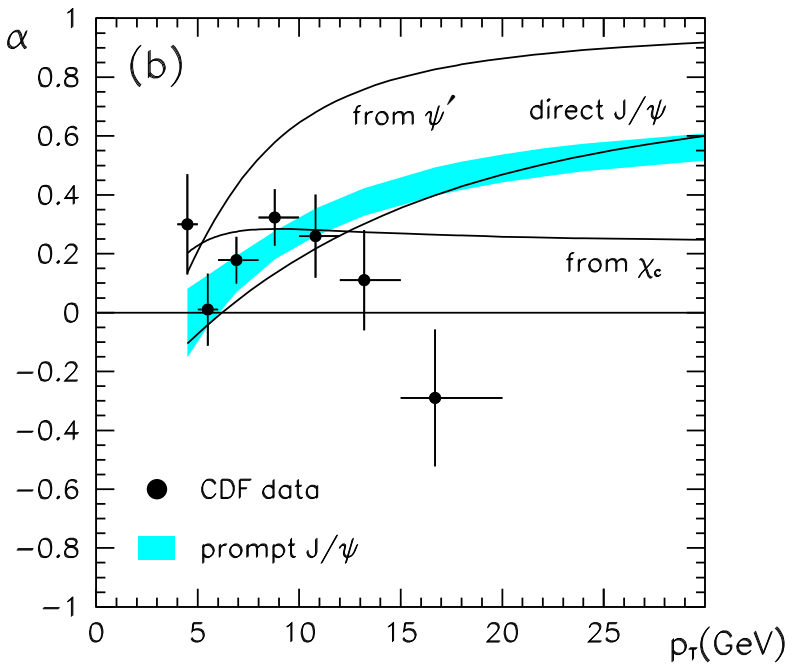

Figure 2.7 NRQCD polarization calculation of $\alpha(p_T)$ for J/ψ compared to CDF data [21]. An α value of 1 is 100% transversely polarized, while an α value of -1 is 100% longitudinally polarized.

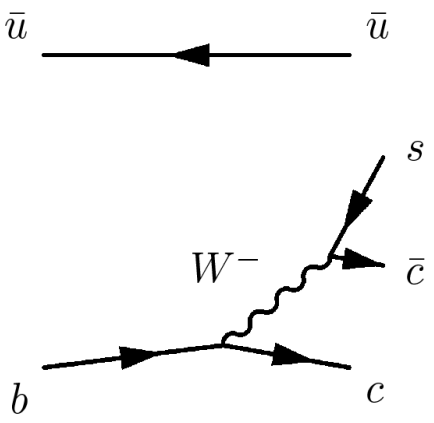

Figure 2.8 Feynman diagram for the process $B^-(\bar{u}b) \to J/\psi(c\bar{c})K^-(\bar{u}s)$.

2.3.4 Non-prompt J/ψ

J/ψ mesons are produced non-promptly only when a b hadron weakly decays, an example of which is shown in Figure 2.8. Therefore, the measurement of the non-prompt J/ψ cross-section is equivalent to a measurement of the b-hadron cross-section, since the b-hadron branching fractions are well known [4]. The theoretical prediction of the b-hadron cross-section consists of three parts: a perturbative QCD prediction of the b (or $\bar{b}$) quark production, b-quark fragmentation into b hadrons, and the b-hadron decay into a J/ψ meson plus some other particle(s) [22].

The perturbative calculation of the b-quark production is evaluated using Fixed Order Next-to-Leading-Logarithm (FONLL) calculations. FONLL combines a full Next-to-Leading-Order QCD prediction with a partial Next-to-Next-to-Leading-Order calculatio, called the Next-to-Leading-Logarithm (NLL) calculation. The NLL calculation adds terms that scale like $\alpha_s \ln(\frac{p_T^B}{m^B})$, where p_T^B and m^B are the transverse momentum and the mass of the b quark. These logarithmic terms are expected to be the dominant contribution from higher perturbative orders [23, 24].

The second part of the theoretical prediction of the non-prompt J/ψ cross-section is the fragmentation of the b quarks into b hadrons. In general, the probability for a quark to fragment into a hadron carrying a certain fraction of the quark's energy is called the fragmentation function. The fragmentation function incorporates low energy QCD physics which cannot be

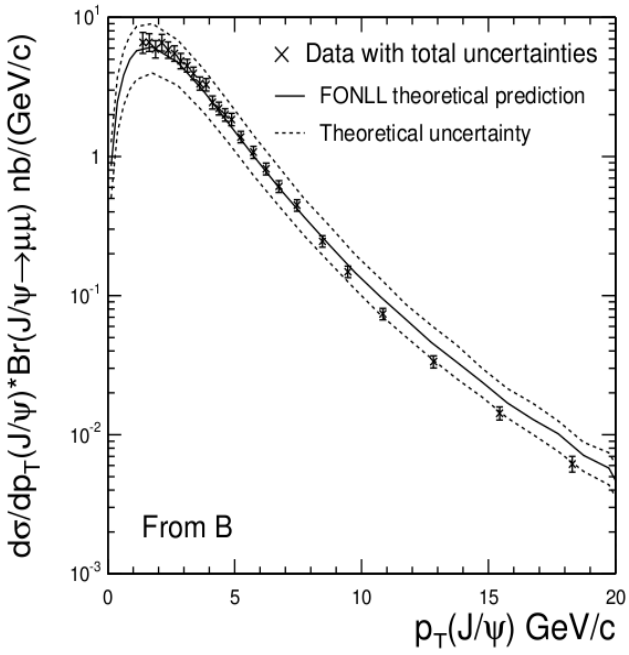

Figure 2.9 Differential cross-section of non-prompt J/ψ as a function of J/ψ transverse momentum, as measured by the CDF Collaboration. The X's indicate the cross–section, and the data uncertainty bars indicate both statistical and systematic uncertainties. The solid line is the nominal theoretical prediction using FONLL calculations and the dashed line is the theoretical uncertainty [28]

calculated perturbatively and it is measured from experimental data. The functional form of the b-quark fragmentation function was first described by Kartvelishvili et al. [27]. The extraction of the b-quark fragmentation functions is performed with e^+e^- experimental data [24, 25, 26].

Finally, the decay of b hadrons into J/ψ mesons is determined by the experimentally measured branching fractions [4]. The resulting prediction of the non-prompt J/ψ cross-section has been compared to the cross-section measured by the CDF Collaboration in Figure 2.9. The predicted cross-section is in good agreement with the experimental measurement.

2.3.5 Decay

Charmonium decay into D^0 and $\bar{D}^0$, as shown in Figure 2.10(a), is the dominant decay mode for sufficiently high mass charmonium states, however, it is kinematically forbidden for the J/ψ since the mass of two D^0 mesons ($m_{D^0} = 1.865$ GeV) is higher than the J/ψ mass. Therefore, the J/ψ has to decay through channels like the one shown in Figure 2.10(b), which

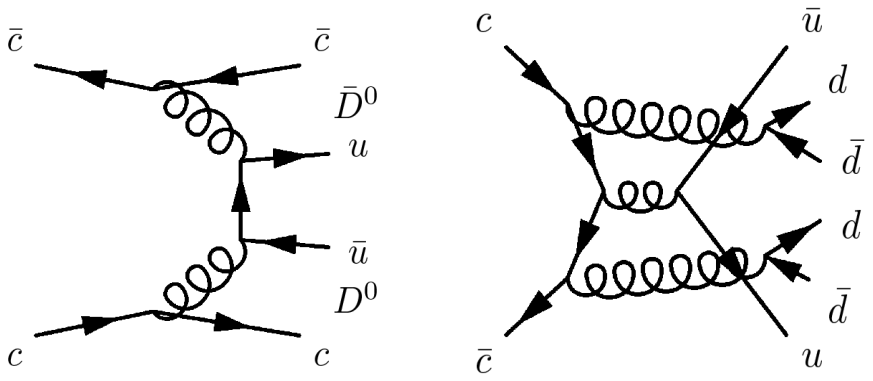

(a) Feynman diagram representing the decay of charmonium into two D^0 mesons, $\mathcal{Q} \to D^0\bar{D}^0$.

(b) Feynman diagram representing the decay of charmonium into three pions, $\mathcal{Q} \to \pi^0\pi^+\pi^-$.

Figure 2.10 Feynman diagrams for charmonium decay. The process in 2.10(a) is kinematically forbidden for the J/ψ. The J/ψ decays through the OZI suppressed diagram in 2.10(b).

are suppressed according to the "OZI rule", named after its discoverers, Okubo, Zweig, and Iizuka.

The OZI rule was formulated in the 1960's to explain why the ϕ meson preferentially decays into two kaons rather than three pions.[2] The two kaon decay is not kinematically forbidden for the ϕ. The OZI rule states that any Feynman diagram that can be split in two by cutting internal gluon lines is suppressed. A rough explanation of the OZI rule is as follows: since mesons are color neutral, color conservation forbids the Feynman diagram for the decay to be split in two by cutting a single gluon line; and charge parity forbids the decay diagram of the J/ψ to be split in two by cutting two gluon lines (both gluons and the J/ψ have $C = -1$); therefore the decay diagram must have three internal gluon lines, thereby suppressing it.

Because the J/ψ's strong force decay channels are suppressed, a sizable percentage of the J/ψ's actually decay electromagnetically into two leptons. The branching fraction for $J/\psi \to \mu^+\mu^-$ is $5.93 \pm 0.06\%$, and for $J/\psi \to e^+e^-$, $5.94 \pm 0.06\%$ [1].

[2] $m_\phi = 1.020$ GeV, and $m_{K^\pm} = 0.494$ GeV.

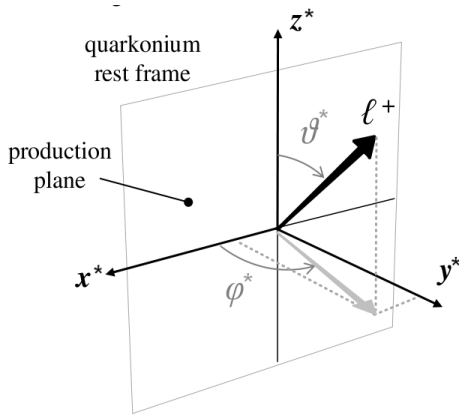

Figure 2.11 Definition of the J/ψ spin alignment angles, in the decay reference frame [29]. l represents the positively charged lepton, and the * indicates that the illustration is in the J/ψ rest frame.

2.4 Spin Alignment

The J/ψ is a spin 1 particle, and the Color Octet Model predicts strong transverse polarization at high p_T, i.e. $J_z = \pm 1$ with respect to the J/ψ momentum direction [29] (at high p_T, most of the J/ψ's spin will come from a single transversely polarized gluon). The NLO Color Singlet Model predicts strong longitudinal polarization ($J_z = 0$) [29, 8]. How the J/ψ's spin is aligned with the beam direction in the J/ψ's rest frame is called its "spin alignment", and measurements of the J/ψ spin alignment can put strong constraints on the production model. In general, the J/ψ is produced in a superposition of three spin eigenstates, $J_z = +1$, -1, and 0:

$$|J/\psi\rangle = b_{+1}|+1\rangle + b_{-1}|-1\rangle + b_0|0\rangle. \tag{2.7}$$

For example, a longitudinally polarized state corresponds to $b_0 = 1$ and $b_\pm = 0$.

This leads to a general angular distribution for the $J/\psi \to \mu\mu$ decay in the lab frame [29]:

$$\frac{d^2N}{d\cos\theta^\star d\phi^\star} \propto 1 + \lambda_\theta \cos^2\theta^\star + \lambda_\phi \sin^2\theta^\star \cos 2\phi^\star + \lambda_{\theta\phi} \sin 2\theta^\star \cos\phi^\star. \tag{2.8}$$

$\theta^\star$ is the angle between the direction of the positive muon momentum in the J/ψ decay frame and the J/ψ line of flight, and $\phi^\star$ is the angle between the J/ψ production and decay planes in the lab frame, as shown in Figure 2.11. A longitudinally polarized state corresponds to $\lambda_\theta = -1$ and λ_ϕ,$\lambda_{\theta\phi} = 0$.

CHAPTER 3. The LHC and ATLAS Experiment

The Large Hadron Collider (LHC) accelerator complex collides proton-proton (pp) beams at $\sqrt{s} = 7$ TeV. The LHC is located in Geneva, Switzerland at a laboratory called the *Conseil Européen pour la Recherche Nucléaire* (European Council for Nuclear Research, CERN). One of the experiments at the LHC is ATLAS (A Toroidal LHC ApparatuS). It detects and measures the particles produced in the pp collisions.

3.1 LHC

The LHC is the newest hadron particle accelerator. It was built in a tunnel which is 100 meters underground and 26.7 kilometers in circumference: the same tunnel that was used by the Large Electron Positron (LEP) collider from $1989 - 2000$. By design, the LHC will collide two proton beams with a center-of-mass energy ($\sqrt{s}$) of 14 TeV, or two beams of heavy-ions with a center-of-mass energy of 5.5 TeV per nucleon pair. Due to technical problems [30], the LHC superconducting magnets, which are responsible for bending the proton beams, are currently only able to operate at a fraction of their nominal power. The dataset we analyze corresponds to pp collisions at $\sqrt{s} = 7$ TeV [31].

The LHC controls groups of protons (called bunches) by moving them along in radio frequency "buckets." The LHC beam is subdivided into 35,640 radio frequency "buckets," but only every tenth can contain a bunch, so that there are 3,564 "slots," which are about 75 cm long. Subtracting gaps in the beam for technical purposes (abort and injection), up to 2,808 of the slots will be filled with bunches of protons [32]. Each bunch nominally contains 10^{11} protons, achieving a instantaneous luminosity of 10^{34} cm^{-2}s^{-1}, and the bunches traveling in opposite directions collide at a rate of 40 MHz at the center of the ATLAS detector. The lu-

minosity measures the intensity of the proton beams, measured in units of particles per unit of area per unit of time. At the design luminosity there will be about 23 proton-proton collisions per bunch crossing. In the early stages of data taking, the luminosity was much lower. The average number of collisions per bunch crossing was between one and two.

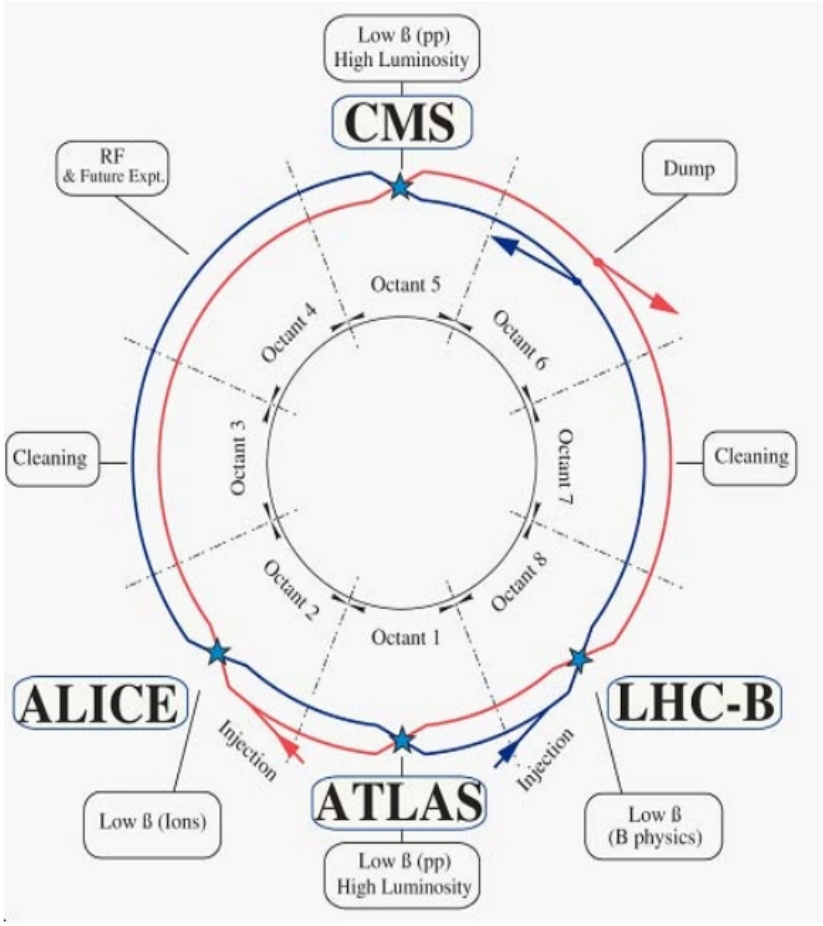

Figure 3.1 LHC schematic layout.

There are four main experiments at the LHC, shown schematically in Figure 3.1.

A Large Ion Collider Experiment (ALICE) [35], is shown in Figure 3.2(a). It is a detector designed to study the physics of the strong force and the quark-gluon plasma at extreme values of energy density and temperature in heavy-ion collisions.

A Toroidal LHC ApparatuS (ATLAS) [36], shown in Figure 3.2(b), is one of the two general-purpose experiments at the LHC. It is described in more detail in section 3.2.

Compact Muon Solenoid (CMS) [37], shown in Figure 3.2(c), is the other general-

purpose experiment at the LHC. The inner detector and most of the calorimeter is immersed in a strong magnetic field of 4 Tesla optimized for tracking muons.

Large Hadron Collider beauty (LHCb) experiment [38], shown in Figure 3.2(d), is dedicated to the precision measurements of CP violation and rare decays of b hadrons. It runs at a lower instantaneous luminosity, corresponding to one collision per bunch crossing.

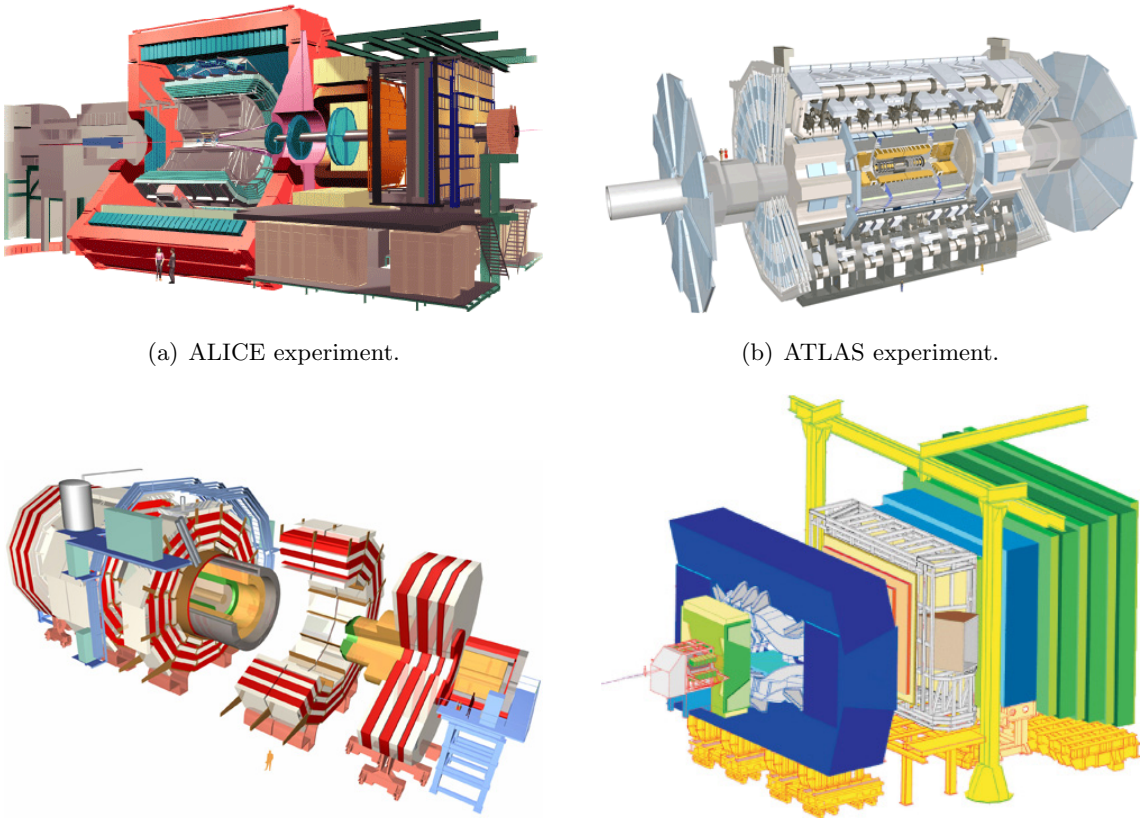

(a) ALICE experiment.

(b) ATLAS experiment.

(c) CMS experiment.

(d) LHCb experiment.

Figure 3.2 The four main LHC experiments.

3.2 ATLAS

The ATLAS detector is shown in more detail in Figure 3.3. It is a general-purpose particle detector that was designed to exploit the full discovery potential at the LHC. The detector was optimized to withstand the high interaction rates and radiation doses, while maximizing the range of sensitivity to new physics (such as the Higgs boson and supersymmetric particles) and top quark studies. It will probe both pp collisions and heavy-ion collisions.

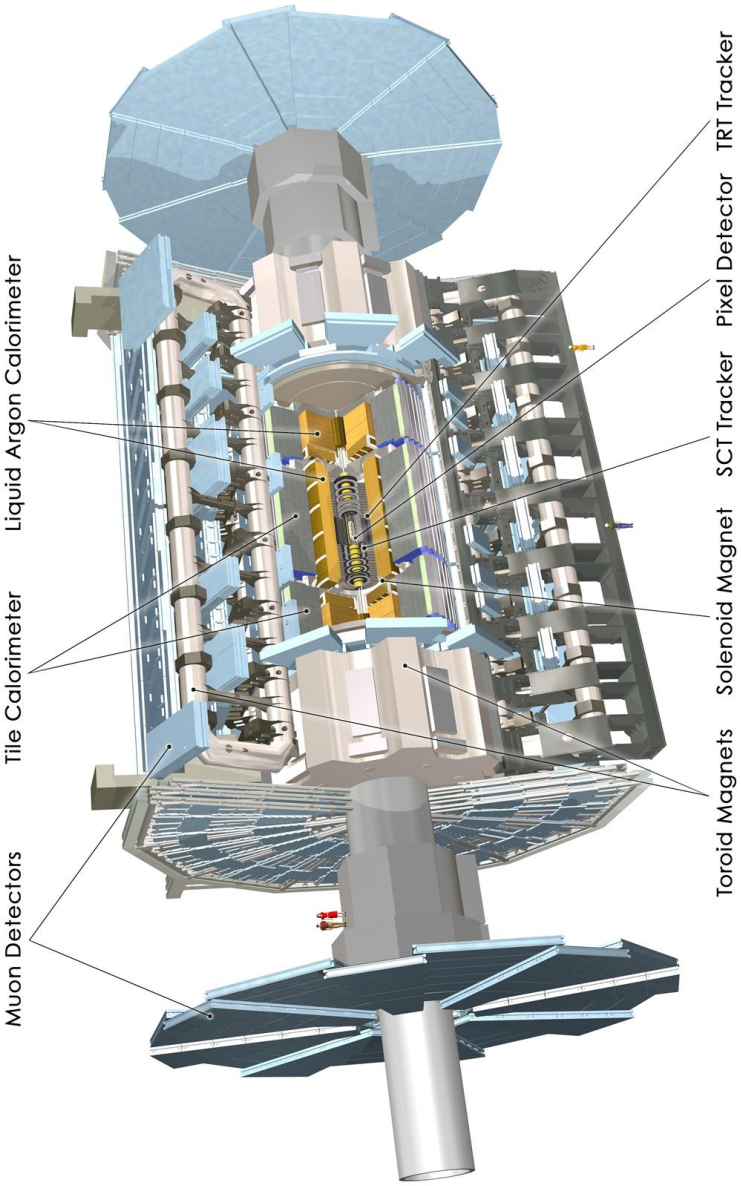

Figure 3.3 A computer generated image of the ATLAS detector [36].

The coordinate system for the ATLAS detector is summarized as follows. The nominal interaction point is the origin of the coordinate system. The axis form a right-handed coordinate system; the beam direction is the z-axis, the x-axis points from the interaction point to the center of the LHC ring, and the y-axis points upwards. The angles are defined as in a spherical coordinate system: the azimuthal angle, ϕ, is measured from the positive x-axis, and the polar angle, θ, is the angle from the positive z-axis. Pseudorapidity is defined as $\eta = -\ln\tan\left(\frac{\theta}{2}\right)$, rapidity is defined as $y = \frac{1}{2}\ln\left(\frac{E+p_z}{E-p_z}\right)$, and transverse momentum, p_T, is the momentum in the $x-y$ plane [36].

The ATLAS detector has five main components: the Inner Detector (ID), composed of three subdetectors, which measures the momentum of charged particles produced; the Calorimeter, composed of two subdetectors (Electromagnetic (EM) and Hadronic), which measure the energy carried by certain particles; the Muon Spectrometer, which measures the momentum of any charged particles which passes through the calorimeters - i.e. muons; the Magnet System, which bends particles in the Inner Detector and Muon Spectrometer; and the Trigger System, which selects interesting events to be processed and recorded for later analysis. The general performance goals of the ATLAS detector are given in Table 3.1. The symbol "$\oplus$" indicates that the uncertainties are summed in quadrature.

Table 3.1 The general performance goals of the ATLAS detector [36].

Detector component	Required resolution	η coverage	
		Measurement	Trigger
ID Tracking	$\sigma_{p_T}/p_T = 0.05\%\ p_T \oplus 1\%$	± 2.5	
EM calorimeter	$\sigma_E/E = 10\%/\sqrt{E} \oplus 0.7\%$	± 3.2	± 2.5
Hadronic calorimeter			
barrel and end-cap	$\sigma_E/E = 50\%/\sqrt{E} \oplus 3\%$	± 3.2	± 3.2
forward	$\sigma_E/E = 100\%/\sqrt{E} \oplus 10\%$	$3.1 < \lvert\eta\rvert < 4.9$	$3.1 < \lvert\eta\rvert < 4.9$
Muon Spectrometer	$\sigma_{p_T}/p_T = 10\%$ at $p_T = 1$ TeV	± 2.7	± 2.4

The particle identification system in ATLAS is shown in the cartoon in Figure 3.4. In the Inner Detector, charged particles leave "tracks," and are bent in a solenoidal magnetic field. Uncharged particles, such as photons and neutrinos, don't leave any tracks in the Inner Detector. In the Calorimeter, the innermost component is the Electromagnetic Calorimeter,

and farther out is the Hadronic Calorimeter. Electrons and photons will deposit most of their energy in the Electromagnetic Calorimeter, while hadrons will deposit most in the Hadronic Calorimeter. The Muon Spectrometer is farthest from the interaction point, and muons will be bent in the toroidal magnetic field which surrounds it. Neutrinos are only detected indirectly, by the observation of a momentum imbalance in the transverse plane.

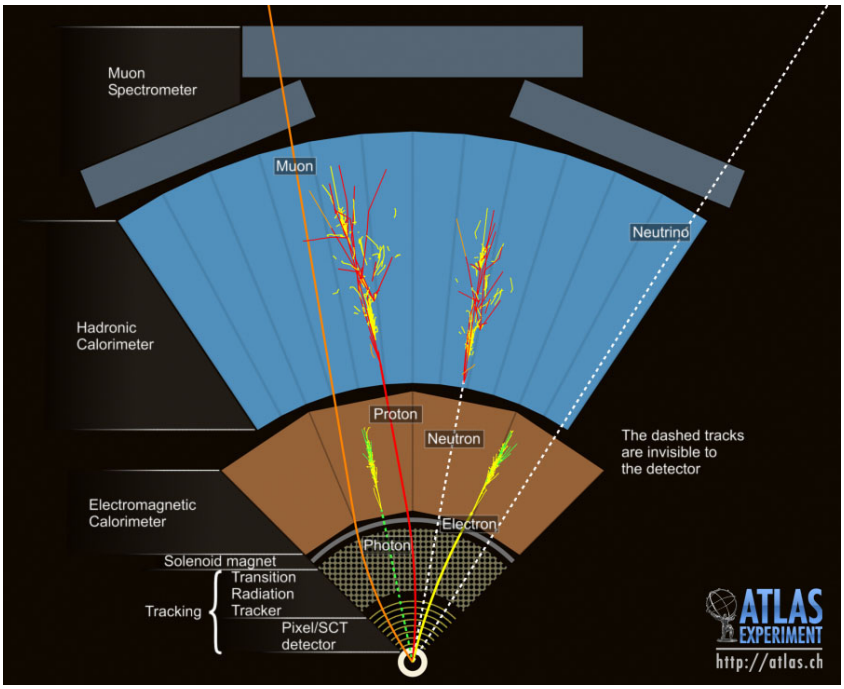

Figure 3.4 A view of the transverse plane of the ATLAS detector.

3.2.1 Inner Detector

At design luminosity, about 1,000 particles within $|\eta| < 2.5$ will emerge from the interaction point every bunch crossing [36]. The Inner Detector (ID) must make high precision momentum and position measurements. A related important task of the Inner Detector is to measure "vertices," which are points where particles collide or decay. In order to meet these needs, the ID is made up of three subdetectors, shown in Figure 3.5: the Pixel detector, SemiConducter Tracker (SCT), and the straw tube Transition Radiation Tracker (TRT). The ID is immersed in a 2 Tesla solenoidal magnetic field which bends charged particles. Charged particles leave "hits" in the different subdetectors. The charged particle trajectory in the ID is approximately

a helix, and pattern recognition algorithms reconstruct particle tracks from these hits.

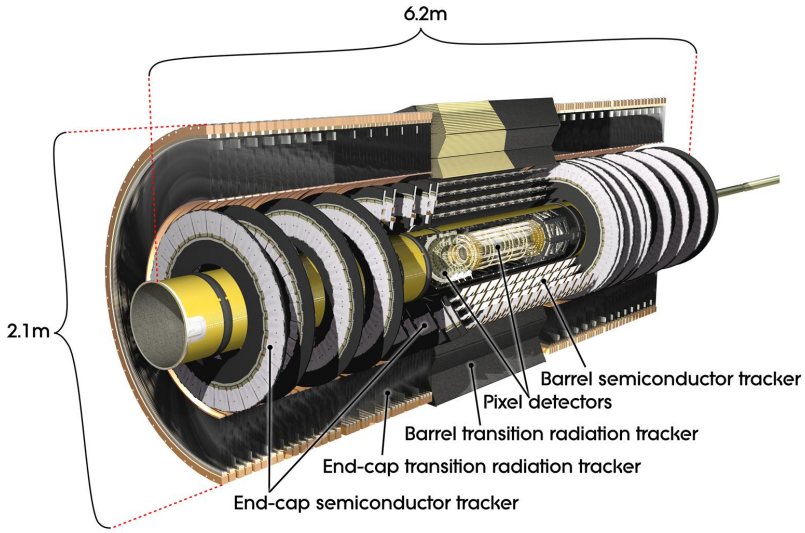

Figure 3.5 A three dimensional view of the Inner Detector [36].

The silicon trackers, Pixel and SCT, are arranged in concentric cylinders around the beam axis (in the central region, the "barrel") and in disks perpendicular to the beam axis (in the high-eta regions, the "end-caps"). They cover the range $|\eta| < 2.5$. The Pixel tracker is the closest to the collision point, made up of three layers with about 80 million readout channels, and has the highest resolution for vertexing. The SCT is farther out, and has eight layers arranged in stereo strips in order to measure both angular coordinates, giving four space points and 6.3 million readout channels [36].

The silicon detectors measure the presence of charged particles. A voltage is applied across doped silicon pixels or strips for the Pixel or SCT detectors, respectively. When a relativistic particle passes through the silicon it will produce electron-hole pairs. The electron-hole pairs are collected and produce a current which allows the position of the particle to be measured [39]. The measured quantity is the "Time-Over-Threshold," which is the amount of time that the current produced by the charged particle is above a certain electronic threshold. This information is recorded for each event that is accepted. This quantity is roughly proportional to the amount of charge produced by the relativistic particle. A sketch of the Time-Over-Threshold for different charges and the discriminator output is shown in Figure 3.6.

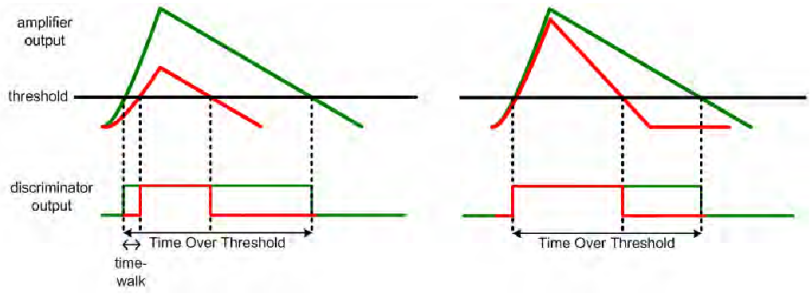

Figure 3.6 Time-Over-Threshold for two different charges; green is a high charge and red is a low charge. The discriminator output is also shown. Lower charges take longer to go above threshold, this effect is referred to as time-walk [44]. The left plot and the right plot have different feedback current settings, which changes the time dependence of the charge response curve.

The TRT covers the range $|\eta| < 2.0$ with 351,000 readout channels. The TRT straw tubes do not provide any η resolution; it only provides information on the radial distance from the beam pipe and ϕ ($R - \phi$ information). On average, each track will leave 36 hits in the TRT. The Transition Radiation Tracker uses transition radiation, which is emitted when a charged particle crosses the interface between two materials with different permittivity. Lower mass charged particles, like electrons, will give off more transition radiation for a given energy, than higher mass particles, so the TRT allows discrimination between electrons and hadrons [36]. A summary of the size and resolution of the three subdetectors is given in Table 3.2.

Table 3.2 Parameters of the Inner Detector [36].

System	Position	Radius (mm)	Length (mm)	Resolution (μm)
Pixel	3 cylindrical layers (barrel)	$50.5 < R < 122.5$	$0 < \|z\| < 400.5$	10 ($R-\phi$), 115 (z)
	2×3 disks (end-cap)	$88.8 < R < 149.6$	$495 < \|z\| < 650$	10 ($R-\phi$, 115 (R)
SCT	4 cylindrical layers (barrel)	$299 < R < 514$	$0 < \|z\| < 749$	17 ($R-\phi$), 580 (z)
	2×9 disks (end-cap)	$275 < R < 560$	$839 < \|z\| < 2735$	17 ($R-\phi$), 580 (R)
TRT	73 straw planes (barrel)	$563 < R < 1066$	$0 < \|z\| < 712$	130 ($R-\phi$)
	160 straw planes (end-cap)	$644 < R < 1004$	$848 < \|z\| < 2710$	130 ($R-\phi$)

3.2.1.1 Pixel Detector

The Pixel detector is very important to measuring long-lived b-hadron decays, needed for the $\mathcal{R}$ measurement. The Pixel detector [40] is composed of 1,456 Pixel modules in three barrel layers, and 144 modules in each of the end-caps. Figure 3.7 shows an example of a Pixel module.

Each Pixel module has 16 front-end integrated circuits (FE) with 2,880 channels per FE for a total of 46,080 channels per Pixel module, and more than 80 million for the whole Pixel detector. Each channel corresponds to a pixel, and they are organized into 18 columns and 160 rows on the FE chip. There is one Module Controller Chip (MCC) per Pixel module which collects and multiplexes the data from the 16 FE chips. Groups of six or seven modules are connected to an optoBoard [40], which transmits or receives optical signals from the standard ATLAS "9U Versa-Module Euro" (VME) crate. The VME crate has slots for up to 16 Read-Out-Drivers (ROD's), and each ROD is responsible for up to 26 Pixel modules [41]. A block diagram of the Pixel detector system architecture is shown in Figure 3.8. Section 4 has more details on the Pixel detector data path.

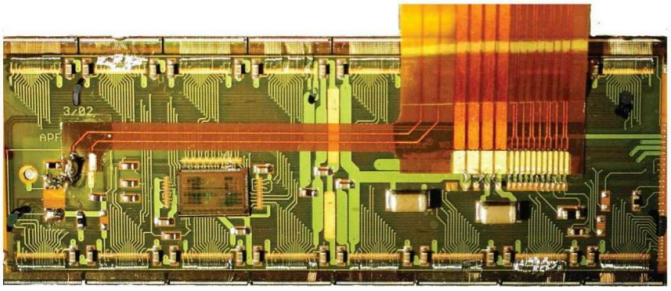

Figure 3.7 Photograph of a Pixel module from the barrel section [36].

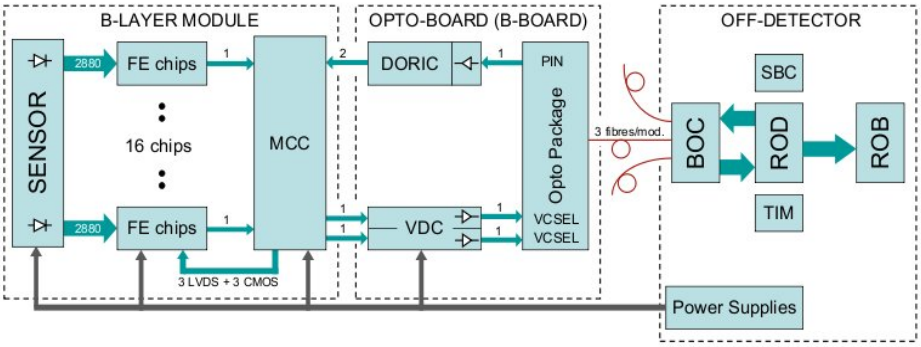

Figure 3.8 Block diagram of the Pixel detector system architecture [40].

The pixel sensors (also called "pixels") have a nominal size of $50 \times 400 \mu\text{m}^2$ in $R - \phi \times z$. In addition to the normal pixel, there are three more types of pixel sensor. All of the pixels on the first and last column of each FE chip are larger: $50 \times 600 \mu\text{m}^2$; these pixels are called

"long pixels." While there are 47,232 pixels on each Pixel module, there are four "ganged pixels" in each column of the FE chip which are connected, leading to a total of 46,080 readout channels for each Pixel module. Because of the metal interconnections between each pixel, the "inter-ganged pixels" between the ganged pixels also have different performance [40].

The Pixel detector will be exposed to significant radiation through the course of its lifetime. State of the art technology was used to meet the high requirements of radiation hardness, resolution, and occupancy. Pixel modules were exposed to radiation at the CERN Proton Synchrotron using 20-24 GeV protons, and the Front-End electronics were designed to be tolerant to Single-Event-Upsets (SEU) or bit-flips in the electronics, through redundancy and correction algorithms. Figure 3.9 shows the resolution in the $R-\phi$ direction of a Pixel module before and after irradiation with a total equivalent fluence of about 10^{15} neutrons/cm^2, the radiation dose projected for 10 years of LHC operation at design luminosity [59]. The design requirements on the Pixel detector resolution are 10μm in the $R-\phi$ direction and 115μm in the z direction. The noise occupancy of the Pixel detector is less than 10^{-6} hits/pixel/bunch crossing, which corresponds to 0.05 hits/module/bunch crossing. If the noise occupancy were higher, the performance of the track reconstruction algorithms would be negatively affected [43, 36].

3.2.2 Calorimeters

The calorimeters in ATLAS have four main tasks: to accurately measure the energy and direction of electrons, photons, and jets; to measure imbalance of energy in the transverse plane, E_T^{miss}; to perform particle identification (separating electrons, photons, and jets); and to trigger on interesting events. The calorimeters cover the range $|\eta| < 4.9$, and in the η region covered by the Inner Detector, the Electromagnetic (EM) Calorimeter provides a fine-grained measurement of electrons and photons [36, 34]. The Electromagnetic and Hadronic Calorimeters are shown in Figure 3.10, and its main parameters are summarized in Table 3.3.

Liquid Argon Calorimeters

For sufficiently high energy, electron and photon interactions in matter primarily occur through two types of interactions: the creation of electron and positron pairs (pair production) and an electron or positron radiating a photon when interacting with a nucleus

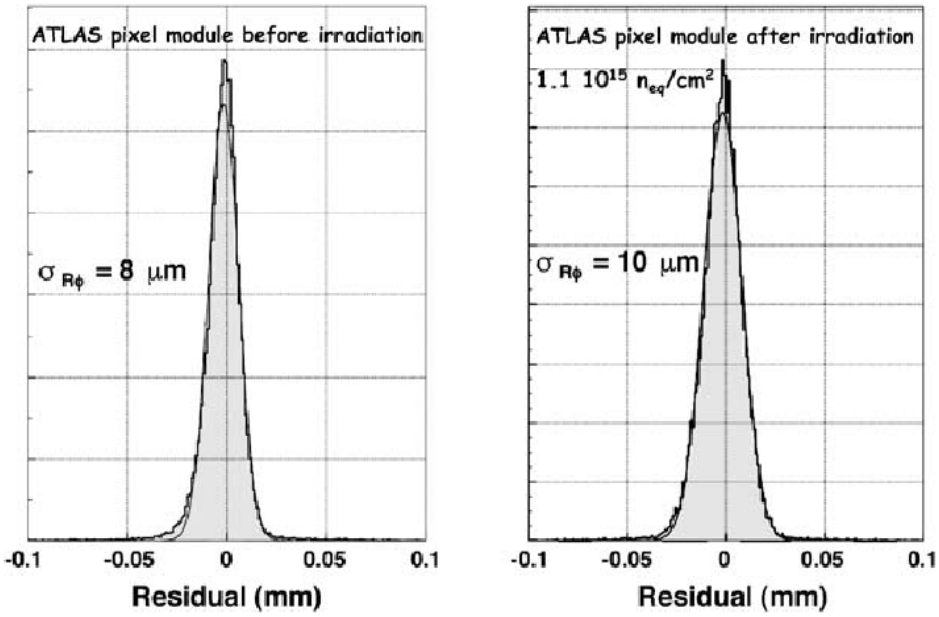

Figure 3.9 Resolution from $R-\phi$ measurements of a production-grade ATLAS Pixel module before (left) and after irradiation (right) with a total equivalent fluence of 10^{15} neutrons/cm^2, as obtained from test beam data taken in 2004 [59].

(Bremsstrahlung). These two types of interactions alternate to create a particle shower; photons decay into an electron and a positron, which radiate further photons through Bremsstrahlung. The particle shower continues until the electron/positron energy loss from ionization equals the energy loss by Bremsstrahlung [39]. The Liquid Argon (LAr) calorimeters use a material with a high number of nucleons (like lead) to induce a particle shower, and use LAr as their active medium. The electromagnetic shower particles ionize the LAr, and the charges are collected at high voltage electrodes attached to the lead plates [36].

Three subdetectors use LAr: the EM Calorimeter, the Hadronic End-cap Calorimeter, and the Forward Calorimeter; these are all shown in Figure 3.11. The EM Calorimeter covers the region $|\eta| < 3.2$, and is divided into a barrel component, $|\eta| < 1.475$, and two end-cap components, $1.375 < |\eta| < 3.2$; it also has several samplings which segment the calorimeter in depth. The region near the transition from barrel to end-cap has poorer performance and is called the "crack" region. The Hadronic End-cap Calorimeter (HEC) is made up of two wheels per end-cap and is directly behind the EM Calorimeter, and it covers the region $1.5 < |\eta| < 3.2$. The Forward Calorimeter (FCal) has a coarser granularity than the other calorimeters and

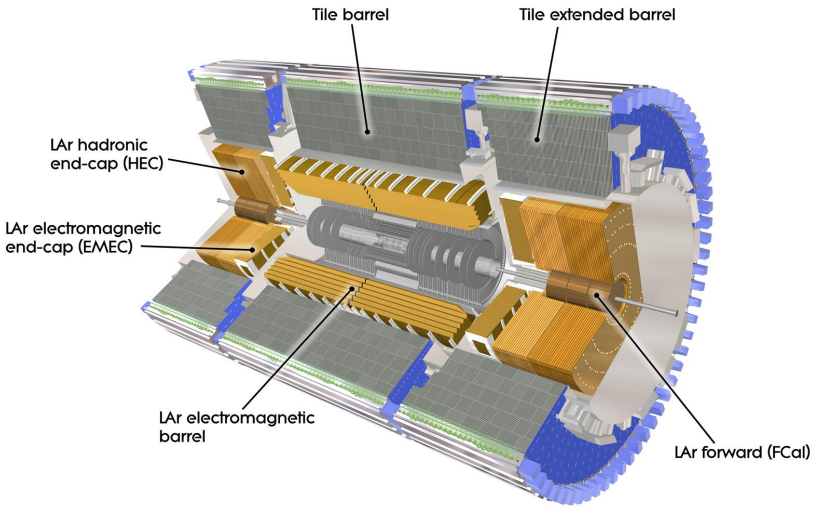

Figure 3.10 A three dimensional view of the calorimeters [36].

covers the highest η range: $3.1 < |\eta| < 4.9$ [36].

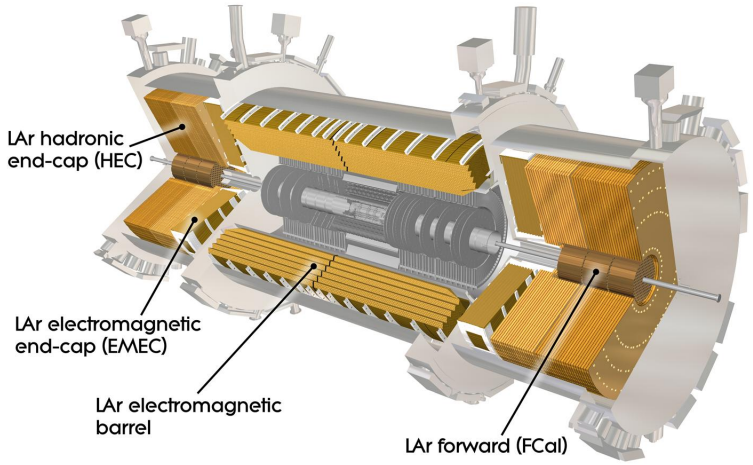

Figure 3.11 A three dimensional view of the LAr calorimeters [36].

Tile Calorimeter

The Tile Calorimeter is located directly behind the EM Calorimeter. It is divided into two components: the barrel, which covers $|\eta| < 1.0$, and two extended barrels, which cover $0.8 < |\eta| < 1.7$. The Tile Calorimeter is a sampling calorimeter which uses steel for its

Table 3.3 Summary of the coverage and granularity of the ATLAS calorimeters [36].

	Barrel		**End-cap**	
Electromagnetic Calorimeter				
Granularity $\Delta\eta \times \Delta\phi$ versus $\lvert\eta\rvert$				
Presampler	0.025×0.1	$\lvert\eta\rvert < 1.52$	0.025×0.1	$1.5 < \lvert\eta\rvert < 1.8$
1st Sampling	$0.025/8 \times 0.1$	$\lvert\eta\rvert < 1.40$	0.050×0.1	$1.375 < \lvert\eta\rvert < 1.425$
	0.025×0.025	$1.40 < \lvert\eta\rvert < 1.475$	0.025×0.1	$1.425 < \lvert\eta\rvert < 1.5$
			$0.025/8 \times 0.1$	$1.5 < \lvert\eta\rvert < 1.8$
			$0.025/6 \times 0.1$	$1.8 < \lvert\eta\rvert < 2.0$
			$0.025/4 \times 0.1$	$2.0 < \lvert\eta\rvert < 2.4$
			0.025×0.1	$2.4 < \lvert\eta\rvert < 2.5$
			0.1×0.1	$2.5 < \lvert\eta\rvert < 3.2$
2nd Sampling	0.025×0.025	$\lvert\eta\rvert < 1.40$	0.050×0.025	$1.375 < \lvert\eta\rvert < 1.425$
	0.075×0.025	$1.40 < \lvert\eta\rvert < 1.475$	0.025×0.025	$1.425 < \lvert\eta\rvert < 2.5$
			0.1×0.1	$2.5 < \lvert\eta\rvert < 3.2$
3rd Sampling	0.050×0.025	$\lvert\eta\rvert < 1.35$	0.050×0.025	$1.5 < \lvert\eta\rvert < 2.5$
Hadronic Tile				
1st and 2nd Sampling	0.1×0.1	$\lvert\eta\rvert < 1.0$	0.1×0.1	$0.8 < \lvert\eta\rvert < 1.7$
3rd Sampling	0.2×0.1	$\lvert\eta\rvert < 1.0$	0.2×0.1	$0.8 < \lvert\eta\rvert < 1.7$
LAr Hadronic End-cap				
			0.1×0.1	$1.5 < \lvert\eta\rvert < 2.5$
			0.2×0.2	$2.5 < \lvert\eta\rvert < 3.2$
LAr Forward Calorimeter				
			$\approx 0.2 \times 0.2$	$3.1 < \lvert\eta\rvert < 4.9$

absorbing material and scintillating plates for the active medium.

3.2.3 Muon Spectrometer

The Muon Spectrometer is made up of four subdetectors: two trigger and two high-precision trackers, and is shown in Figure 3.12. It covers the range $|\eta| < 2.7$, and is immersed in a toroidal magnetic field. In the region $|\eta| < 1.4$, the magnetic field is provided by the barrel toroid, and in the region $1.6 < |\eta| < 2.7$, the magnetic field is provided by the end-cap magnets. In the region from $1.4 < |\eta| < 1.6$ (called the transition region), the magnetic field is provided by a combination of barrel and end-cap magnets [36].

One of the performance goals of the Muon Spectrometer is to provide a stand-alone measurement of the p_T with a resolution of 10% for 1 TeV tracks. To meet this goal, the Monitored Drift Tubes (MDT's) and the Cathode Strip Chambers (CSC's) provide a precision tracking measurement in the bending plane. The MDT's cover the range $|\eta| < 2.7$, except in the innermost layer, where they cover $|\eta| < 2.0$. The CSC's are used only at $2.0 < |\eta| < 2.7$, and

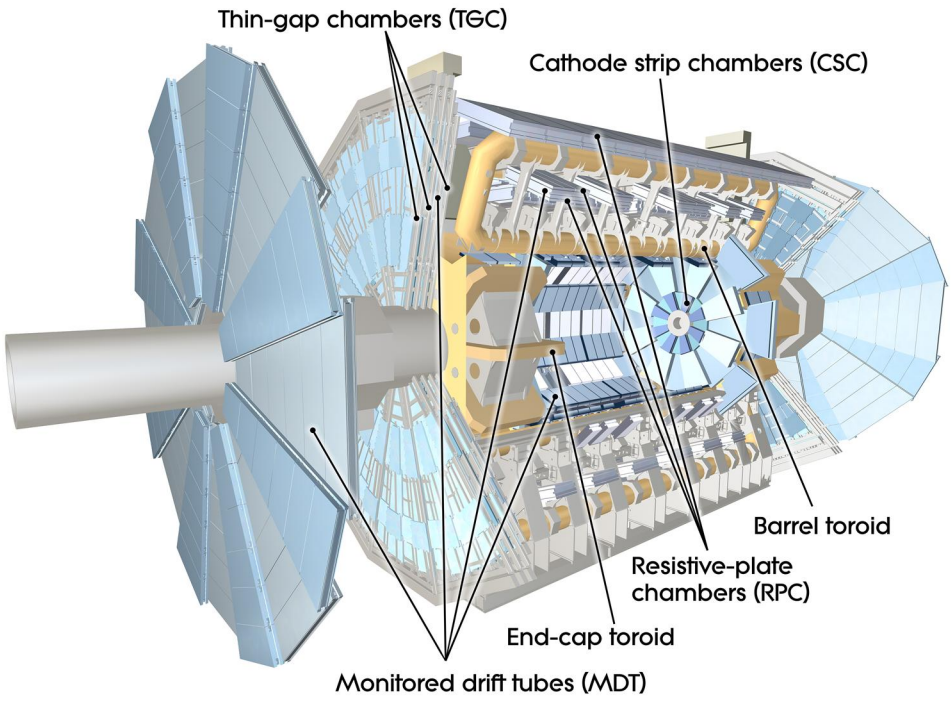

Figure 3.12 A three dimensional view of the Muon Spectrometer [36].

they are specially designed to withstand the high rates expected at large η. The MDT's are tubes filled with gas, with a sense anode wire in the center. A charged particle passing through will ionize the gas. The electric field is calibrated so that the drift velocity of the ions is approximately constant, which makes the drift time approximately proportional to the distance from the primary ionization. The CSC's are wires between two metal plates held at a potential difference, called a multiwire proportional chamber. When a charged particle passes through, it produces ions which are attracted to the closest wire [39].

Triggering is provided by the Resistive Plate Chambers (RPC's) in the range $|\eta| < 1.05$, and by the Thin Gap Chambers (TGC's) in the range $1.05 < |\eta| < 2.4$; both of these subdetectors measure the track coordinate in the nonbending plane. While the trigger system only covers the range $|\eta| < 2.4$, the TGC's can provide a second coordinate out to $|\eta| < 2.7$. The η coverage and resolution of each of the four detectors is detailed in Table 3.4. RPC's are two resistive plates separated by a gas mixture, and held at a potential difference. A charged particle passing through will ionize the gas, and the resulting shower is read out by metallic strips attached to the outer faces of the resistive plates. The TGC's are multiwire proportional chambers.

Table 3.4 Summary of the coverage and resolution of the Muon Spectrometer subdetectors [36].

Type	Function	η Coverage	Chamber resolution (RMS) in z/R	ϕ
MDT	Tracking	$\lvert\eta\rvert < 2.7$	35μm (z)	
CSC	Tracking	$2.0 < \lvert\eta\rvert < 2.7$	40μm (R)	5 mm
RPC	Triggering	$\lvert\eta\rvert < 1.05$	10 mm (z)	10 mm
TGC	Triggering	$1.05 < \lvert\eta\rvert < 2.7$	$2-6$ mm (R)	$3-7$ mm

3.2.4 Magnet System

The magnet system of ATLAS consists of the Central Solenoid, the Barrel Toroid, and two End-cap Toroid magnets. The Central Solenoid magnet provides a 2 Tesla axial magnetic field in the central tracking volume. It is a superconducting magnet with a single layer coil. The Barrel Toroid and End-cap Toroid magnets provide a 0.5 to 1 Tesla toroidal magnetic field for the Muon Spectrometer. The Barrel Toroid consists of eight coils, and is shown in the Figure 3.13. The two End-cap Toroids are located inside the Barrel Toroid, at each end [36].

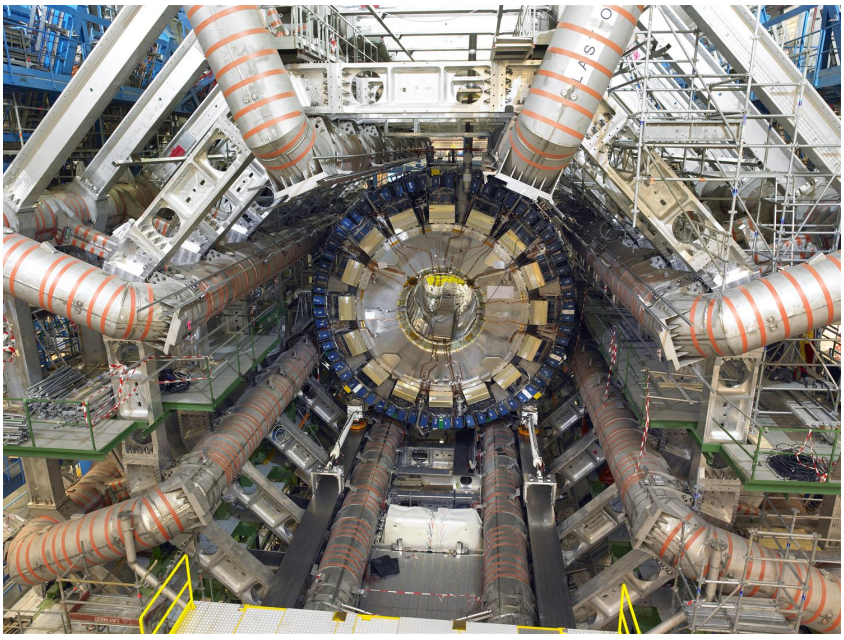

Figure 3.13 A view of the ATLAS calorimeter and Barrel Toroid magnets [36].

3.2.5 Trigger System

The ATLAS Trigger and Data Acquisition system (TDAQ) has three levels of online event selection. Each trigger level refines the selections made in the previous level, reducing the 40 MHz LHC bunch crossing rate to the ≈200 Hz final event rate written to tape. The first level trigger is hardware based, while the higher level triggers use commercial computing. An overview of the ATLAS trigger system detailing the trigger rates at each level is shown in Figure 3.14.

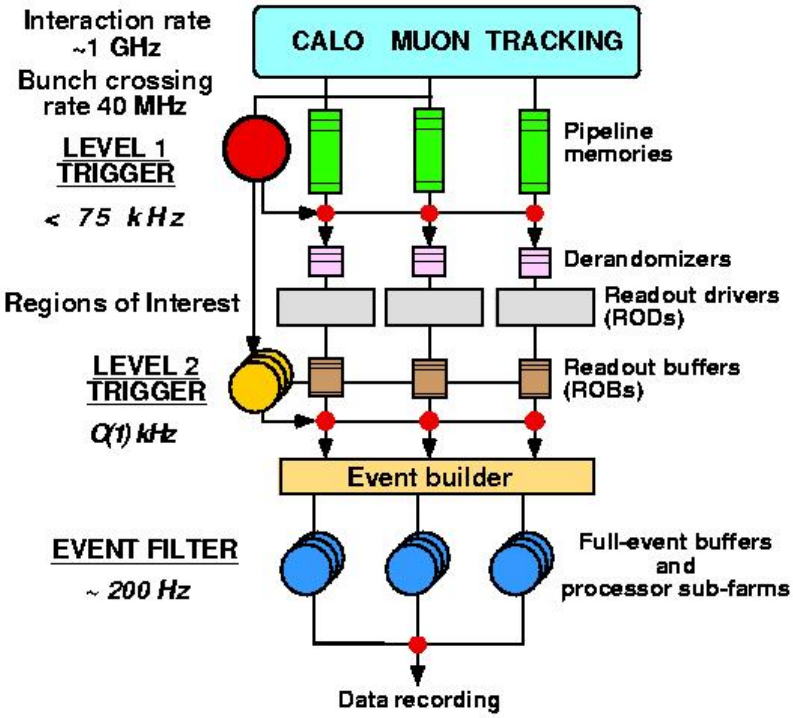

Figure 3.14 Overview of the ATLAS trigger system [34].

The Level 1 (L1) trigger makes an initial selection based on information with reduced granularity from the calorimeter and muon systems. It is a simple selection which accepts events with a high energy deposit in the calorimeters or a high p_T muon. Objects that are selected at L1 are electrons, photons, taus decaying hadronically, jets, and large missing E_T. Data are stored in a buffer until the L1 decision is made, but because of the finite length of the buffer, the decision must be made in 2.5μs, and the maximum L1 output rate is 75 kHz.

It passes on information about the Region-of-Interest (RoI) (geographical location in η and ϕ) to the Level 2 trigger.

The Level 2 (L2) trigger is seeded by the RoI information from the L1 trigger. L2 uses all of the detector information within the RoI with full granularity, although not the full detector calibration and alignment. The L2 trigger reduces the trigger rate to about 3.5 kHz, and has an average event processing time of about 40 ms. The final level of trigger is the Event Filter (EF). The EF uses the entire detector, including alignment and calibration information; its selections use offline analysis reconstruction algorithms. The EF reduces the event rate to about 200 Hz, and processes an event at a rate of 1 Hz [36].

CHAPTER 4. Pixel DAQ

The Pixel detector is crucial for identifying and measuring long-lived b hadron decays, needed for the $\mathcal{R}$ measurement. The Pixel detector Data-Acquisition (DAQ) system plays an essential role in the operation of the Pixel detector, as it ensures all of the hit information is retrieved from the detector with maximum efficiency. The basic unit of the Pixel DAQ system is the Read-Out-Driver (ROD). 132 ROD's service the Pixel detector, performing module configuration, readout, trigger distribution, event-fragment assembly, and monitoring [43, 45].

4.1 Pixel/SCT ROD

The ROD is a 9U VME board, with a design common to both the Pixel detector and the SCT [40, 41, 42]. 9 VME crates service the Pixel detector: three for the B-layer (the innermost barrel layer of the Pixel detector), four for Layers 1 and 2, and two for the end-cap disks. Each VME crate contains up to 16 ROD's; a Single-Board Computer (SBC), which is an interface between the ROD's and the DAQ host computer; and a Timing-Trigger-and-Control Interface Module (TIM), which receives timing, trigger, and control information from ATLAS and propagates it to the ROD's. There is a Back-Of-Crate (BOC) card for each ROD that converts the ROD's electrical signals into optical ones and sends them to the detector modules' MCC, and vice versa. The BOC hosts the S-Link, which sends formatted data from the ROD to the ATLAS Read-Out-System (ROS) [45]. A picture of the ATLAS Pixel/SCT ROD is shown in Figure 4.1(a), and a block diagram of it is shown in Figure 4.1(b).

The primary purposes of the ROD are trigger signal propagation, data formatting, and module configuration. When an L1 trigger is received by the ROD's, they propagate an L1 trigger to the Pixel FE chips. Once the data requested by the L1 trigger has been sent from

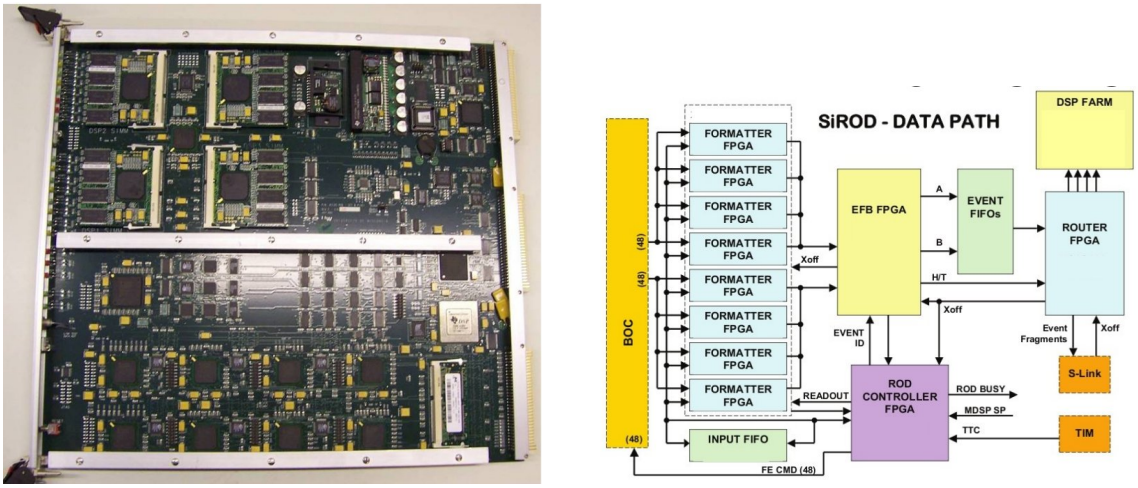

(a) Picture of the ATLAS Pixel ROD [42]. (b) Block diagram of the ATLAS Pixel ROD [40].

Figure 4.1 The ATLAS Pixel ROD.

the MCC to the ROD, the ROD serializes the multiplexed data from the MCC's and formats the data stream into "event-fragments" that are then sent to the ROS for the Level 2 trigger. The electronic threshold and response curve for each pixel can be configured with several parameters at the MCC, FE, and individual pixel level; the ROD is responsible for sending these configuration bits, which are saved in an offline database, to the Pixel detector.

The secondary purposes of the ROD are detector calibration and monitoring. The Pixel detector is calibrated by injecting known amounts of charge into the sensors, and measuring the response. By varying the parameters which control the electronic threshold and response curve, the calibration parameters can be chosen to minimize noise[1] while still measuring signal charges, and to ensure a uniform response throughout the detector, which is important for detector simulation. The ROD can also sample the L1 data stream when it is processed, and provide an important monitoring tool for low level occupancy, timing, and error information [45].

The ROD consists of a combination of Field-Programmable Gate Arrays (FPGA's) and Digital Signal Processors (DSP's), chosen to provide maximum versatility during data taking and calibration. The FPGA's perform the time critical operations, such as formatting, building, and routing of data. One "Master" DSP and four "Slave" DSP's are used for the control and coordination of ROD operations, and for high level tasks like monitoring and calibration [45,

[1]The noise occupancy of the Pixel detector should be no greater than 0.05 hits/module/bunch crossing.

46, 47].

Resetting the ROD and the VME interface is handled by the Program Reset Manager FPGA (PRM). When the ROD is booted it resets the Master DSP and initializes the other FPGA's: the ROD Controller FPGA (RCF), the Formatter FPGA (FMT), the Event Fragment Builder FPGA (EFB), and the Router FPGA (RTR). The RCF and the Master DSP setup the "data-path" FPGA's (FMT, EFB, and RTR) [45].

The Formatter FPGA serializes the multiplexed data from the MCC's. There are eight FMT's per ROD, each of which can handle four links over which data can be sent. Each link sends data at a rate of 40 MHz, and the number of links per module depends on the readout speed used: the B-layer uses 160 Mbits/sec readout, which has four links per module; the end-caps and Layer 1 use 80 Mbits/sec readout, which has two links per module; and Layer 2 uses 40 Mbits/sec readout, which has one link per module. The Event Fragment Builder FPGA collects the FMT output, checks the L1 and bunch-crossing ID, and counts errors. The Router FPGA routes the formatted data to the S-Link, and can also simultaneously transfer data to the Slave DSP's.

The Master DSP is responsible for generating triggers for detector calibration, and for the configuration of the BOC and the Pixel modules. The Slave DSP analyzes data for detector calibration and monitoring, which are described in greater detail in the following sections [45].

4.2 Pixel Calibration Procedure

Calibration scans are performed regularly on the Pixel detector in order to find the optimal values of the tuning parameters, and in order to check that the current values of tuning parameters are still optimal. Since the Pixel detector is exposed to the highest level of radiation, being the innermost subdetector, the tuning will change as the detector is irradiated.

During a calibration scan, the Master DSP generates triggers, updates configuration parameters and sends new configurations to the Pixel modules, and coordinates the scan in general. The Slave DSP interprets the data processed by the data-path FPGA's, generates and stores histograms for the scan, and does some simple calculations for the scan (such as averages and standard deviations of Time-Over-Threshold values).

There are five scan loops steered by the Master DSP, shown in Figure 4.2. During the innermost loop, the Master DSP generates triggers, and the MCC injects charges into the pixels (this is called the "calibration strobe.") The relative position of the other loops can be varied according to their speed; the loop which takes the least amount of time per step should always be the innermost loop, in order to optimize the calibration scan time. The mask-stage loop is a special loop over groups of pixels, since the size of the buffers on the FE chip were designed with data taking in mind, the buffers are not large enough to hold data from every pixel. Because of this, the pixels on the FE chip are divided into 32 groups, and calibration scans are only run over one group at a time. The loop over these groups is the mask-stage loop. The other loops are over parameters on the MCC, FE chip, and individual pixels [45].

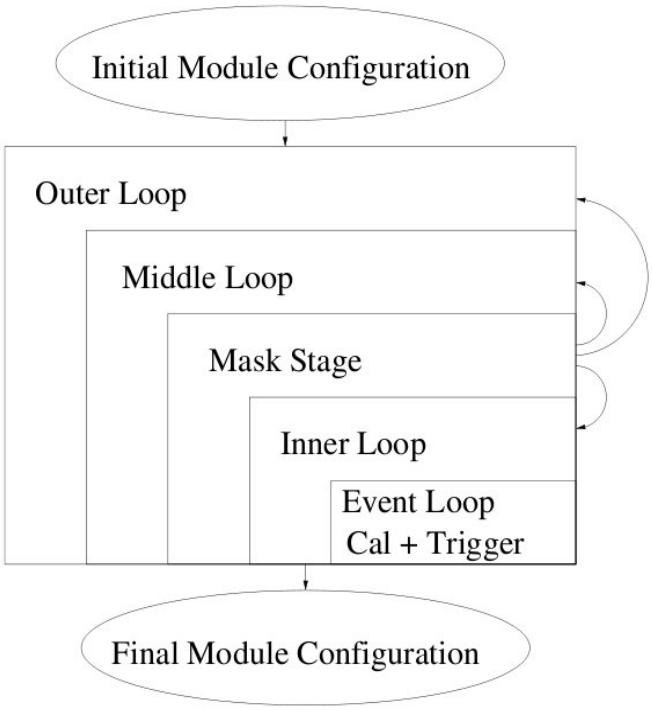

Figure 4.2 The five calibration scan loops of the Pixel ROD [45].

The timing relationship between a calibration strobe and sending the Level 1 trigger signal is shown in Figure 4.3. The MCC operates on a 40 MHz clock, so that one cycle represents one ATLAS bunch crossing (BC). The MCC sends the calibration command to the strobe circuitry, and the delay between the calibration command and the injection of charge is called the "strobe

delay." Once a charge is injected, the FE chip records hits and labels them with a time stamp, which corresponds to the leading edge of the signal. The hits will only be read out if a Level 1 (L1) trigger command arrives within the latency of the hit time stamp (called the FE L1 latency), otherwise the hit is discarded. The delay between the MCC calibration command, and when the MCC sends the L1 trigger is called the "L1 delay." The L1 delay is set to mimic the ATLAS L1 delay during data taking. When the L1 trigger is received by the FE chip, the chip is read out for a configurable number of consecutive bunch crossings. Typically the L1 delay is set to 240 BC's, the L1 latency is set to 248 BC's, and the read out is set to 16 BC's. During data taking, the read out window will be nominally set to 1 BC, but normally in calibration scans we set it to a larger window so that the pixel timing is more robust [45].

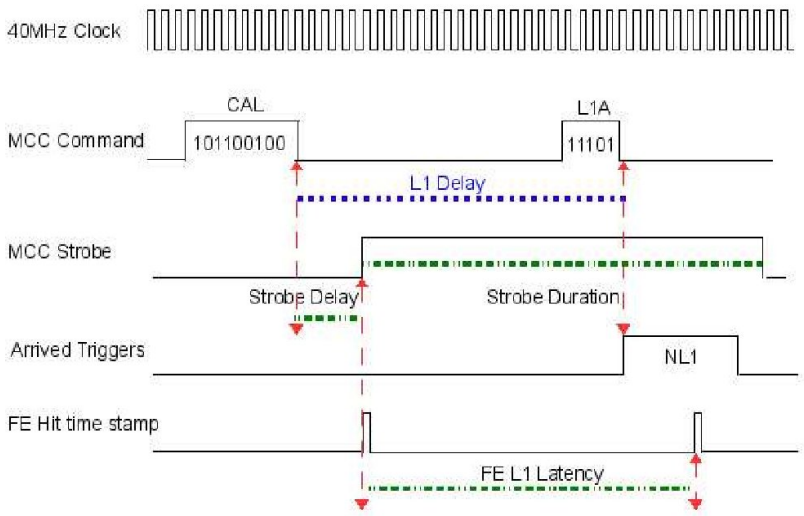

Figure 4.3 Illustration of timing for a calibration scan [45].

As an example, a typical scan which is run to check that the Pixel detector calibration is still acceptable is the "Threshold Scan." In this scan there is only one parameter loop: injected charge. The injected charge is the innermost parameter loop, and the outermost loop is the mask-stage. The Slave DSP's analyzes the data stream, and stores which pixels had hits for an injected charge. About 100 triggers are sent for each value of injected charge, and a simple fit is performed on the number of hits per pixel as a function of injected charge. From this the threshold mean and standard deviation are calculated, and compared with the value expected (which depends on what threshold the detector was tuned for). As the detector is irradiated it

will become necessary to tune it more often as the response of the pixels will change.

4.3 Pixel ROD Online Monitoring

The Slave DSP's can sample the Level 1 data stream as it goes through the Router to the S-Link, and perform simple analysis of the data, such as calculating pixel and average module occupancy, error counting, and timing information. Monitoring the Level 1 stream in this way is called "ROD Monitoring." The ROD Monitoring is an important monitoring tool, and it complements the other ATLAS monitoring tools, which analyze the Level 2 and Event Filter data streams [45, 48].

The average module occupancy from a data taking run in 2010 is shown in Figure 4.4. In this figure the half-circles in the center represent the B-Layer of the Pixel detector, and the concentric half-circles further out are Layers 1 and 2; it can clearly be seen that the average occupancy decreases as the distance from the beam pipe increases.

Examples of the pixel occupancy and timing histograms stored by the ROD Monitoring are shown in Figures 4.5(a) and 4.5(b), respectively. The straight line patterns in the occupancy histograms likely come from electrons knocked off of atoms (also called delta rays) by a low p_T track passing through the silicon wafer. Low p_T tracks have a greater probability to create delta rays. Higher p_T tracks can cause several adjacent pixels to go above threshold, creating a cluster. The timing histogram was made while the Pixel detector was reading out 5 bunch crossings for every Level 1 trigger. In the first two columns there shouldn't be any hits, except for random noise, and the middle column is the one which was triggered on. There are hits in the last two bunch crossing columns because of the (already defined earlier) phenomenon called "time-walk"; hits depositing lower charge will cause the pixel to rise above threshold slower, and for a sufficiently low charge, the pixel will rise above threshold the bunch crossing after the charged particle passed through the pixel. Therefore, the average Time-Over-Threshold (ToT) for column 2 is higher than the average ToT for column 3.

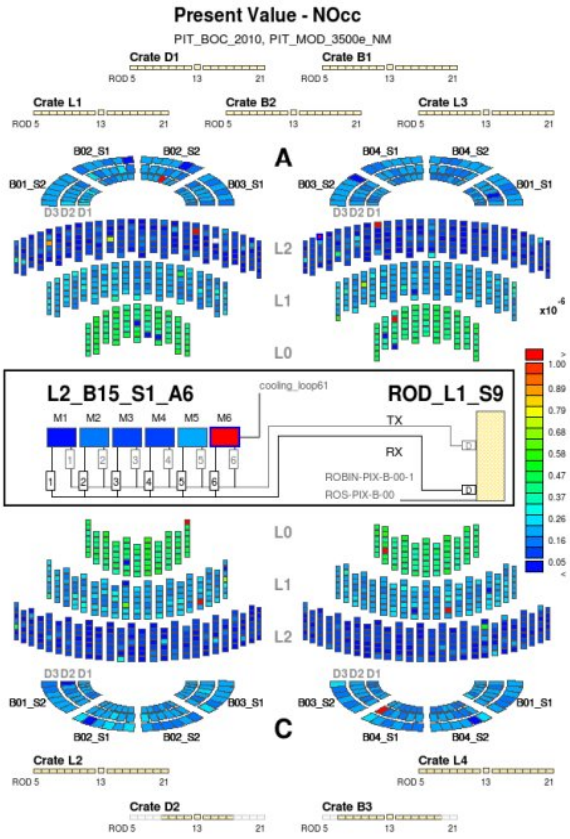

Figure 4.4 Average module occupancy during an early data taking run in April 2010. The B-Layer is labeled L0, Layers 1 and 2 are labeled L1 and L2, and the end-cap disks are labeled D1, D2, and D3. Units here are hits/module.

4.4 Outlook

The Pixel DAQ system performed well in the first data taking runs. As the LHC operators gain more experience, the instantaneous luminosity will rise, increasing the amount of data flow through the DAQ system, and therefore putting greater demands on it. Consequently, the sampling rate of the ROD Monitoring will need to be reduced. As the Pixel detector is irradiated, calibration scans need to be run more frequently to get the most performance out of the detector. The configurability of the scan structure, as well as the wide range of calibration scans currently available will help greatly to keep the detector performance within expectations.

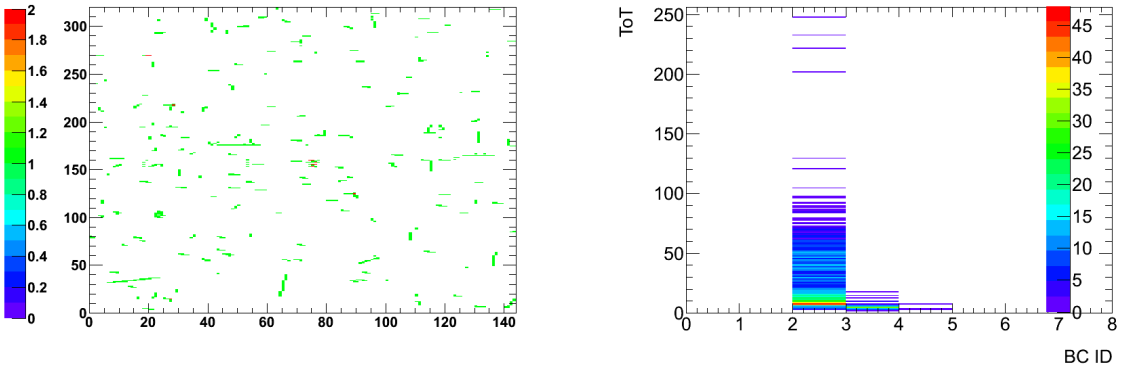

(a) Pixel occupancy of a Layer 1 module during a data taking run in early 2010.

(b) ToT versus bunch crossing offset for all the hits on a Layer 1 module during a data taking run in early 2010.

Figure 4.5 Examples of ROD Monitoring histograms.

CHAPTER 5. J/ψ Cross-Section Measurement

The double differential cross-section of the J/ψ, $\frac{d^2\sigma}{dp_T dy}$, is measured in bins of rapidity, y, and transverse momentum, p_T. The J/ψ yield is determined from a weighted fit, where the weight takes into account the probability to reconstruct a J/ψ candidate. The cross-section in each p_T and y bin is:

$$\frac{d^2\sigma}{dp_T dy} = \frac{N_{\text{wgt}}}{\mathcal{L}\Delta p_T \Delta y}. \tag{5.1}$$

N_{wgt} is the weighted number of J/ψ determined by the fit, and Δp_T and Δy are the widths of the bin in p_T and y, respectively [49].

5.1 Luminosity and Differential Cross-Section

In particle physics, luminosity is a measure of beam intensity with the units of the number of particles per area per time, and similarly the integrated luminosity is the luminosity integrated over time. The cross-section of an interaction is a proportional to the the probability of an interaction, expressed in units of area, typically barns. One barn is 10^{-28} m^2. The product of the integrated luminosity and the cross-section of particular process describes how often a certain process occurs, as shown in equation 5.2. The total integrated luminosity from the LHC is shown in Figure 5.1 as a function of time.

$$N_{J/\psi} = L\sigma_{J/\psi}, \tag{5.2}$$

where L is the integrated luminosity, σ is the cross-section, and N is the number of J/ψ. We used 2.2 pb^{-1} of integrated luminosity for the differential cross-section analysis, and 2.3 pb^{-1} for the $\mathcal{R}$ measurement.[1] We measure the "inclusive cross-section", which means we

[1]The $\mathcal{R}$ measurement has a higher integrated luminosity since multiple triggers were used.

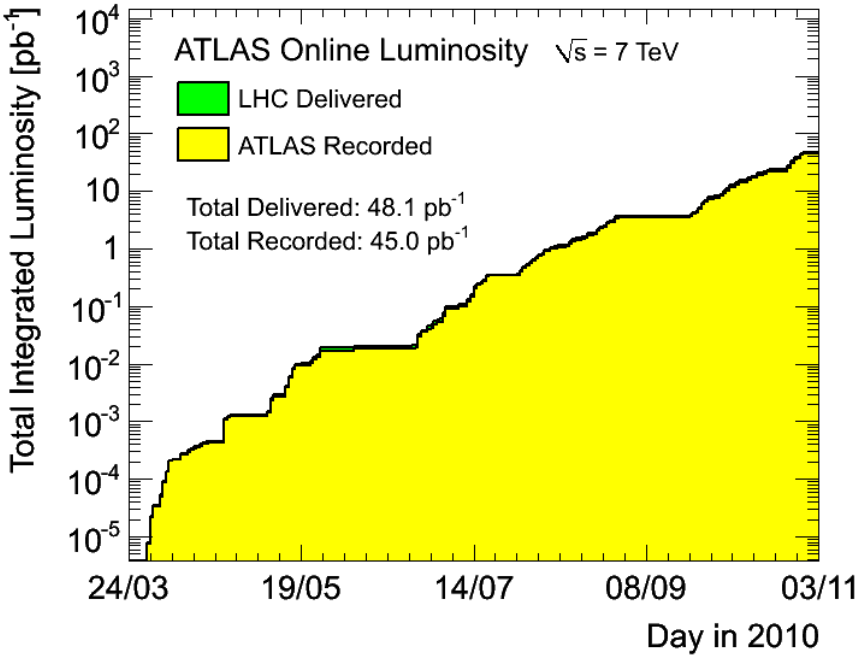

Figure 5.1 Integrated luminosity per day, delivered by the LHC (green), and recorded by ATLAS (yellow). The ATLAS data taking efficiency is about 94%, so the green part is not very visible.

do not distinguish by what process the J/ψ was produced. We cannot record all produced J/ψ's, but do so with some efficiency, $\epsilon = \frac{N_{\text{obs}}}{N}$. The cross-section can then be determined from equation 5.3. We can determine the value of the efficiency from either data or simulation but usually a combination of both is needed.

$$N_{\text{obs}} = L\sigma\epsilon. \tag{5.3}$$

The luminosity is determined in ATLAS through "event-counting" methods [32]. The luminosity can be written as

$$L = \frac{\mu n_b f_r}{\sigma_{\text{inel}}} = \frac{\mu_{\text{vis}} n_b f_r}{\sigma_{\text{vis}}}. \tag{5.4}$$

In the first equality, μ is the average number of inelastic interactions per bunch crossing, f_r is the frequency of beam revolution, n_b is the number of bunches which cross at the interaction point, and σ_{inel} is the pp inelastic cross-section [32, 51, 52]. The second equality is the same as the first, but the visible number of inelastic interactions $\mu_{\text{vis}} \equiv \epsilon\mu$ and the visible cross-section

$\sigma_{\text{vis}} \equiv \epsilon\sigma_{\text{inel}}$ are used. μ_{vis}, n_b, and f_r are directly measurable quantities, but σ_{vis} is determined indirectly, as explained below.

First, the absolute luminosity is determined from measured accelerator parameters [51, 52]. The absolute luminosity can be written:

$$L = \frac{n_b f_r n_1 n_2}{2\pi\Sigma_x\Sigma_y}, \tag{5.5}$$

where n_1 and n_2 are the numbers of particles in the two colliding bunches and Σ_x and Σ_y represent the widths of the horizontal and vertical beam profiles. Σ_x and Σ_y are determined through "van der Meer" scans in which the event rate is recorded while scanning the two beams across each other in the vertical and horizontal directions. This yields two Gaussian-like curves, from which Σ_x and Σ_y are extracted. After determining the luminosity at zero separation from Equation 5.5, σ_{vis} is extracted from Equation 5.4.

5.2 Monte Carlo Samples

The Monte Carlo approach to simulating detector response to a specified physical process relies on repeated random sampling of a probability distribution. Samples of Monte Carlo simulation (also called Monte Carlo samples) were used in different studies and systematic cross-checks related to the cross-section analysis. They are generated using PYTHIA 6 [53] and tuned using the ATLAS MC09 tune [54] which uses the MRST LO* parton distribution functions [55]. The passage of the generated particles through the detector is simulated with GEANT4 [56]. For signal J/ψ Monte Carlo, the PYTHIA implementation of prompt J/ψ production sub-processes in the NRQCD Color Octet Mechanism framework [57] is used [49].

5.3 Muon Reconstruction

Two muon offline reconstruction algorithms are used in this analysis: combined muons and segment-tagged muons, also referred to as "tagged", muons.[2] Combined muons are constructed from a global track fit to hits from the inner detector and the muon spectrometer. Tagged muons

[2]Offline refers to the fact that the reconstruction is performed after the data has been collected, an online muon reconstruction algorithm would refer to one performed under the time constraints of the trigger system.

are constructed from inner detector tracks, which are extrapolated to muon spectrometer hits. These two algorithms have different advantages and disadvantages, and both are useful over the p_T range studied in this analysis. Efficiency is one way of characterizing the two algorithms, which refers to the ratio of the number of reconstructed muons from a J/ψ meson to the actual number of such muons. The tagged-muon algorithm reconstructs many low p_T muons, but is also prone to reconstruct many "fake" muons i.e. it identifies tracks as muons which did not come from muons, such as pions decaying in flight into muons. The combined muon algorithm reconstructs much fewer fake muons, but is not very efficient at low p_T. The two algorithms' efficiencies are shown in Figures 5.2(a) and 5.2(b); the transition between the barrel and the end-cap can be seen at $\eta \approx 1$, and the gap between the two half-barrels at $\eta \approx 0$ can be seen. There are some "holes" in the tagged muon efficiency, since the efficiency is quite low at high p_T.

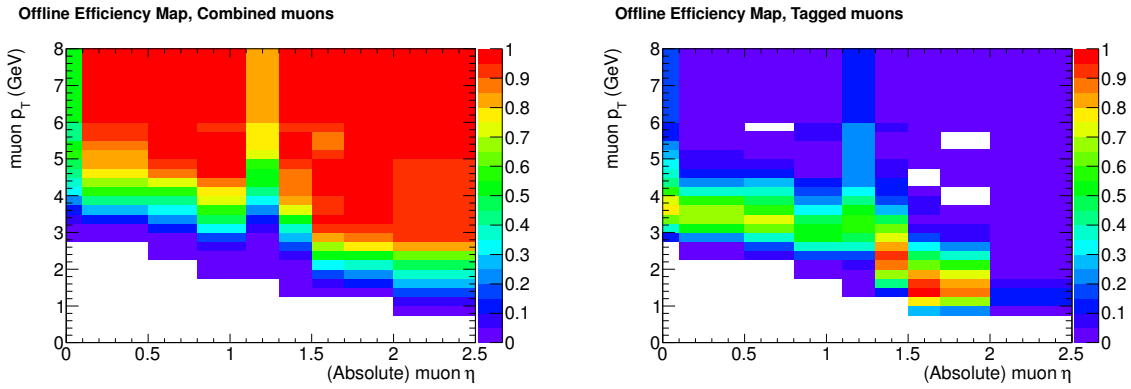

(a) Combined muon efficiency.

(b) Tagged muon efficiency.

Figure 5.2 Offline muon reconstruction efficiencies used in the cross-section analysis, as a function of muon η and p_T.

We use combined-combined and combined-tagged muon pairs, but do not use tagged-tagged muon pairs. In this way, we take advantage of the greater efficiency of the tagged muon algorithm at low p_T and keep the extra background contribution that it introduces acceptable. In all cases the inner detector tracks are used for measuring the J/ψ's kinematic properties since using the combined muon tracks does not significantly improve the p_T resolution for the p_T range used in this analysis.

5.4 J/ψ Selection

In the analysis, we use four different types of selection requirements, sometimes called "cuts": quality cuts, trigger requirements, acceptance cuts, and "carving" cuts. Quality cuts are used to increase the ratio of signal to background of the sample. In no particular order, they are hit requirements on the muon's inner detector track: ≥ 1 Pixel hit and ≥ 6 SCT hits and tagged-tagged muon pairs are excluded. We only use events that have at least two muon tracks of opposite charge. The muons' inner detector tracks are then fit to a common vertex using a minimum χ^2 fit [62]. The χ^2 from this fit is required to be less than 200.

As time progressed the instantaneous luminosity increased. The increasing instantaneous luminosity meant that an increasing amount of data passed through the DAQ system, and to alleviate this, muon triggers with lower thresholds were prescaled.[3] The applied prescaling was so severe, that it was more efficient to switch to a higher threshold rather than to keep using the same trigger. This analysis uses three distinct luminosity periods and in each period we use a different single-muon trigger. Single-muon triggers (one which only requires a single muon) are used because their efficiency was better understood than the double-muon triggers at the time of the analysis. In the first period we used the L1_MU0 trigger. It has the lowest threshold of any muon trigger, and looks for hit coincidences within different muon detector layers inside preprogrammed geometrical regions. In the next period we used the EF_mu4 trigger, which required a single muon with p_T greater than 4 GeV, and in the final period we used EF_mu6, requiring a single muon with p_T greater than 6 GeV.

The acceptance cuts are related to the physical acceptance of the detector, and the trigger requirements of each period. The physical acceptance requirements are the fiducial η acceptance of the detector and the requirement that the muon have enough momentum to break through the calorimeter. This results in a basic acceptance cut of $p_\mu > 3$ GeV and $|\eta_\mu| < 2.5$ on each muon. On top of the basic acceptance cut, there is an additional trigger acceptance cut which varies with the period; at least one muon must be above the trigger threshold, p_T^{thresh}. The trigger thresholds for the three periods are 0, 4, and 6 GeV, as explained above.

[3] Prescaled means that a specified fraction of events which passed the trigger were randomly dropped.

Finally, the "carving" cuts are used to eliminate low efficiency bins with zero population. Their definition is based on the shape of the efficiency curves. There are two components to the carving cuts, reflecting the two different types of efficiency maps used in the analysis: offline and trigger. The offline component to the carving cuts requires each muon to meet the requirements shown in Table A.1.

For the L1_MU0 trigger, the regions of low trigger efficiency are not removed by the period-dependent acceptance cuts, and so additional carving cuts are needed. The cuts are charge dependent, since the L1_MU0 trigger efficiency depends strongly on the muon charge and only one of the muons from the reconstructed J/ψ meson has to satisfy the cuts. Negatively charged muons will bend in the opposite longitudinal direction from positively charged muons, so the cuts are reversed in η for them. The trigger carving cuts are shown in Table A.2.

After these selections are applied, the $J/\psi \to \mu\mu$ candidates are binned according the J/ψ's p_T and y. The bin boundaries we used, and the bins that are populated enough to be fit, are shown in Table A.4 The J/ψ candidates are divided into four different regions, called "slices." One rapidity slice has the full p_T range available. Figure 5.3 shows the J/ψ mass peak in the four different rapidity slices, and Table 5.1 summarizes the number of J/ψ's and the mass position and resolution; note that the $\psi(2S)$ mass peak at about 3.7 GeV is included in the fit. The resolution gets worse as y increases because at higher y the muons decaying from the J/ψ meson are more likely to have an η in the end-cap region of the Inner Detector.

Table 5.1 Fitted yield, mass position, and mass resolution in the four J/ψ rapidity slices [49].

	J/ψ rapidity range			
	$\lvert y\rvert < 0.75$	$0.75 \leq \lvert y\rvert < 1.5$	$1.5 \leq \lvert y\rvert < 2.0$	$2.0 \leq \lvert y\rvert < 2.4$
Signal yield	6710 ± 90	10710 ± 120	9630 ± 130	4130 ± 90
Fitted mass (GeV)	3.096 ± 0.001	3.097 ± 0.001	3.097 ± 0.001	3.109 ± 0.002
Fitted resolution (MeV)	46 ± 1	64 ± 1	84 ± 1	111 ± 2

5.5 Event Weights

The various efficiencies are combined together to form a weight, defined as the inverse of the probability to reconstruct the J/ψ meson with a certain p_T and y value. The per event

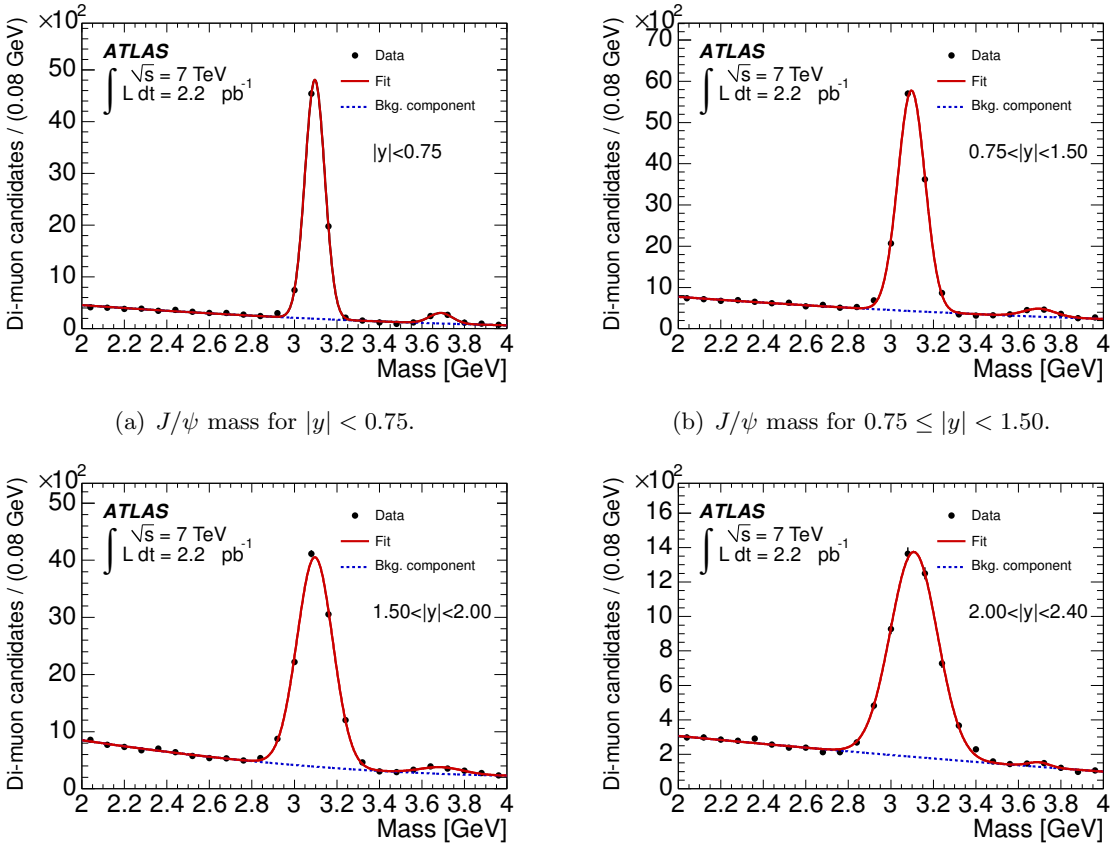

(a) J/ψ mass for $|y| < 0.75$.

(b) J/ψ mass for $0.75 \leq |y| < 1.50$.

(c) J/ψ mass for $1.50 \leq |y| < 2.00$.

(d) J/ψ mass for $2.00 \leq |y| < 2.40$.

Figure 5.3 J/ψ candidates' mass after all selection requirements in different rapidity ranges [49].

inverse weight is defined as shown in equation 5.6:

$$P = w^{-1} = \mathcal{A}_{\text{spin}}(p_T^{J/\psi}, y^{J/\psi}, t)\mathcal{M}(p_T^{J/\psi}, y^{J/\psi})\mathcal{E}_{\text{track}}\mathcal{E}_{\text{combined}}(p_T{}^+, \eta^+, p_T{}^-, \eta^-, t)\mathcal{P}(p_T^{J/\psi}, y^{J/\psi}), \tag{5.6}$$

where $\mathcal{A}_{\text{spin}}$ represents the acceptance correction, which varies with the spin alignment that the J/ψ meson is produced with. $\mathcal{M}$ corrects for bin migrations. $\mathcal{E}_{\text{track}}$ is the tracking efficiency. $\mathcal{P}$ represents the integrated luminosity in the p_T and y bin. $\mathcal{E}_{\text{combined}}$ represents the combination of offline and trigger efficiencies. The offline efficiency is different for tagged and combined muons, and the trigger efficiency is different for tagged and combined, and for positively and negatively charged muons. In addition, since a different trigger threshold is used in each of the three different luminosity periods, there is a different trigger efficiency for each data taking period, t.

The expression for $\mathcal{E}_{\text{combined}}$ can be broken into three components, for each pair of muon algorithms allowed: combined-combined, combined-tagged, tagged-combined. Tagged-tagged pairs are excluded, as noted above:

$$\mathcal{E}_{\text{combined}} = \mathcal{E}^{cc} + \mathcal{E}^{ct} + \mathcal{E}^{tc}, \tag{5.7}$$

where the letter t or c represents whether the tagged or the combined muon algorithm was used. Positive and negative muons have different efficiencies, so the order of the letters matters. The offline component to the combined efficiency in each of the three cases is the product, $\epsilon^{\alpha}_{\text{off}}(p_T^+, \eta^+)\epsilon^{\alpha}_{\text{off}}(p_T^-, \eta^-)$, since both muons must be reconstructed. The index α indicates the muon reconstruction algorithm (tagged or combined). The trigger component of the combined efficiency reflects the fact that we are using single-muon triggers; the requirement is that at least one of the muons is reconstructed, i.e. the complement of no muons being reconstructed, as in equation 5.8:

$$1 - (1 - \epsilon^{\alpha}_{\text{trig}}(p_T^+, \eta^+))(1 - \epsilon^{\alpha}_{\text{trig}}(p_T^-, \eta^-)). \tag{5.8}$$

The components of the combined efficiency in 5.7 are defined in equation 5.9.

$$\begin{aligned}
\mathcal{E}^{cc} &= \epsilon_{\text{off}}{}^{c}_{+}\epsilon_{\text{off}}{}^{c}_{-}(\epsilon_{\text{trig}}{}^{c}_{+} + \epsilon_{\text{trig}}{}^{c}_{-} - \epsilon_{\text{trig}}{}^{c}_{+}\epsilon_{\text{trig}}{}^{c}_{-}) \\
\mathcal{E}^{tc} &= \epsilon_{\text{off}}{}^{t}_{+}\epsilon_{\text{off}}{}^{c}_{-}(\epsilon_{\text{trig}}{}^{t}_{+} + \epsilon_{\text{trig}}{}^{c}_{-} - \epsilon_{\text{trig}}{}^{t}_{+}\epsilon_{\text{trig}}{}^{c}_{-}) \\
\mathcal{E}^{ct} &= \epsilon_{\text{off}}{}^{c}_{+}\epsilon_{\text{off}}{}^{t}_{-}(\epsilon_{\text{trig}}{}^{c}_{+} + \epsilon_{\text{trig}}{}^{t}_{-} - \epsilon_{\text{trig}}{}^{c}_{+}\epsilon_{\text{trig}}{}^{t}_{-})
\end{aligned} \tag{5.9}$$

The notation is shortened here, so that ϵ_+ means $\epsilon(p_T^+, \eta^+)$, and similarly for ϵ_-.

5.5.1 Acceptance

The acceptance represents the probability that the reconstructed J/ψ candidate falls within the fiducial volume of the detector, i.e. that the J/ψ candidate passes the acceptance cuts. The acceptance cuts are described in detail in the section 5.4. However, the acceptance also strongly depends on the spin alignment of the J/ψ, which is not known for the LHC conditions. The spin-alignment calculations are explained in more detail in section 2.4. This uncertainty contributes to the theoretical uncertainty of the measured differential cross-section. For the nominal cross-section we use a default assumption of a flat spin alignment. The corresponding

acceptance maps are shown in Figure 5.4. Two-dimensional acceptance maps were produced as a function of the J/ψ candidate transverse momentum and rapidity. The different luminosity periods each have a different trigger threshold, and we require at least one of the muons to have a momentum above the trigger threshold to remove regions of very low trigger efficiency. Since the acceptance cuts depend in part on the trigger threshold, there is a different map for each of the three trigger periods.

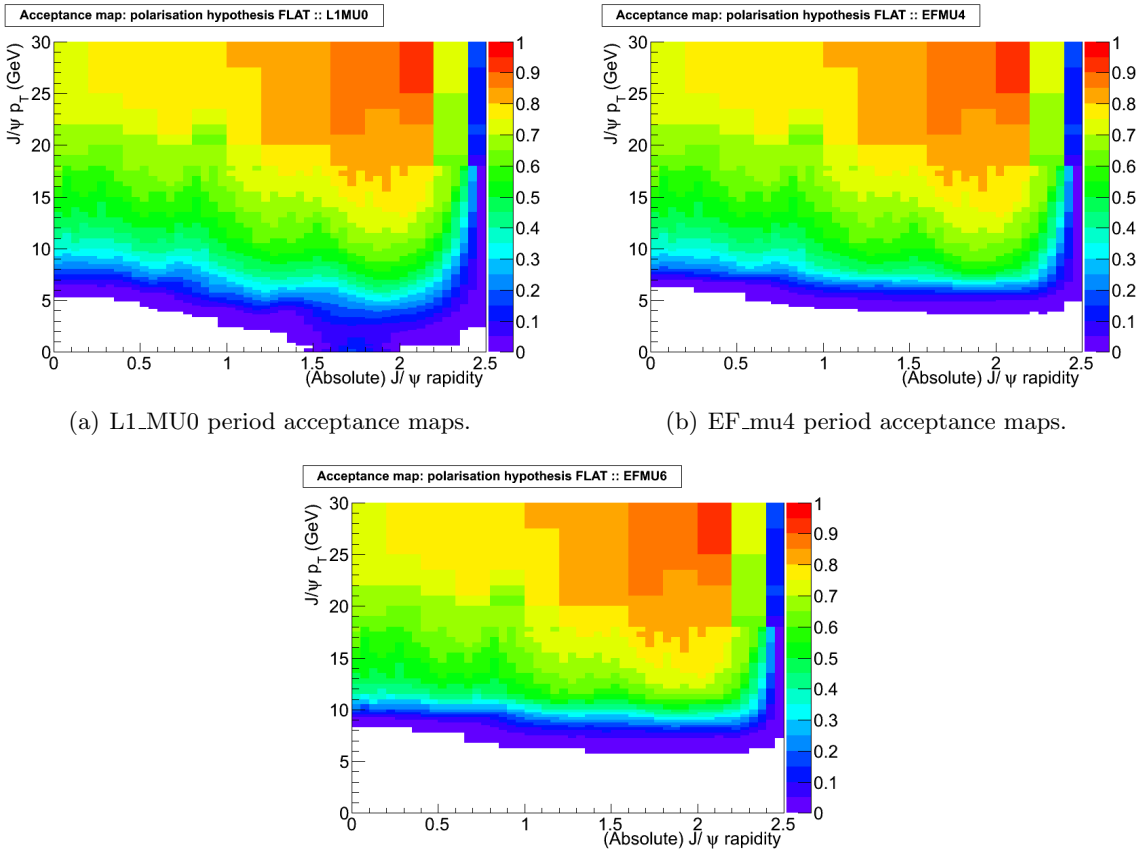

(a) L1_MU0 period acceptance maps.

(b) EF_mu4 period acceptance maps.

(c) EF_mu6 period acceptance maps.

Figure 5.4 Acceptance maps for the flat spin alignment.

5.5.2 Offline Muon Reconstruction Efficiency

The offline reconstruction efficiency is estimated using a tag-and-probe study on both data and Monte Carlo simulation [60]. A brief description of the tag-and-probe method is as follows. Well reconstructed muons (the tags) are paired with Inner Detector tracks (the probes), and the invariant mass of the tag and probe pair is calculated. The probes are split into two classes:

those which match to a reconstructed muon and those which do not. A χ^2 fit is performed on the J/ψ mass peak for each of the two classes of probes, and the ratio of the fitted number probes which are matched to a reconstructed muon to the total number of probes is the efficiency, $\epsilon = \frac{N_{\text{matched}}}{N_{\text{total}}}$.

A scale factor, defined as the ratio between the data and Monte Carlo efficiencies is derived, as a function of muon η and ϕ. The difference between data and Monte Carlo is about 2% in most bins, as shown in Figure 5.5. The hatching pattern in Figure 5.5 along the ϕ direction is due to the different sectors in the muon spectrometer, and in the η direction at $\eta \approx 1$ there is the transition between the barrel and end-cap that is not well described by the ATLAS Monte Carlo simulation.

For the cross-section analysis, we use the tag-and-probe study on data for the efficiency on muons with $p_T < 6$ GeV, but for $p_T \geq 6$ GeV we use the tag-and-probe study and Monte Carlo simulation corrected with a scale factor, since ≥ 6 GeV there were not enough J/ψ candidates to accurately calculate the efficiency only from data. The total efficiency map, combining Monte Carlo with scale factors above 6 GeV and data tag-and-probe below 6 GeV, is shown in Figure 5.2. The inner detector tracking efficiency is calculated from simulation, and found to be constant in the kinematic regions we are using, $99.0 \pm 0.5\%$.

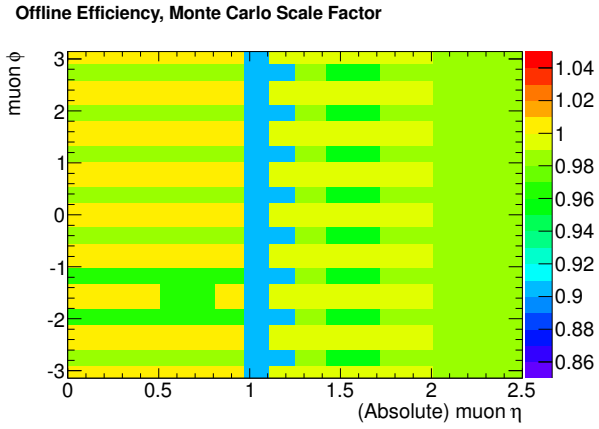

Figure 5.5 Monte Carlo to data scale factor as a function of muon η and ϕ.

5.5.3 Trigger Efficiency

The trigger efficiency is calculated from a combination of data and Monte Carlo. A scale factor which is a function of the muon η and p_T is derived from the ratio of data and Monte Carlo efficiencies using the tag-and-probe method. However, we found the trigger efficiency significantly depended on the muon charge in the low p_T region. We didn't have a large enough sample to calculate the trigger efficiency separately for both positively and negatively charged muons using tag-and-probe on data. For this study, we calculated the trigger efficiency directly from Monte Carlo, and then corrected it to data using the scale factor. The scaled trigger efficiencies for combined muons in each period are shown in Figure 5.6.

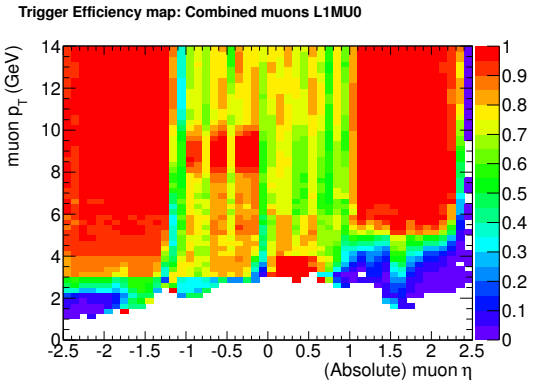

(a) Combined muon efficiency for L1_MU0.

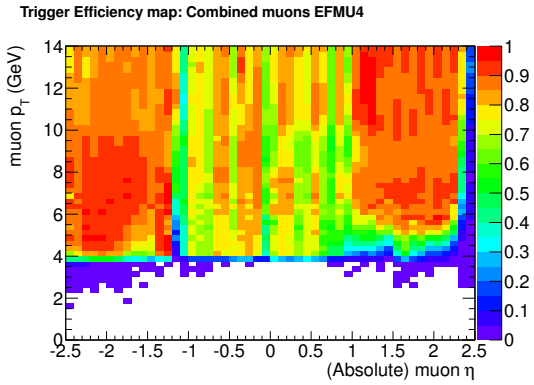

(b) Combined muon efficiency for EF_mu4.

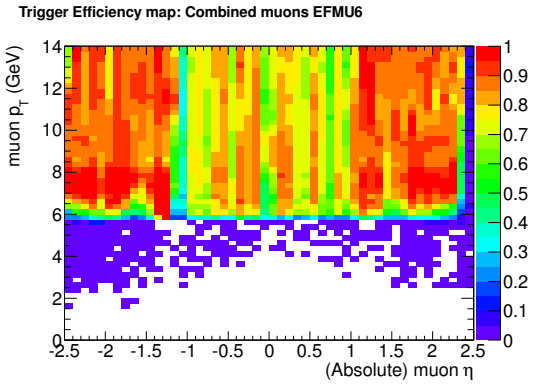

(c) Combined muon efficiency for EF_mu6.

Figure 5.6 Trigger efficiencies as a function of muon η and p_T.

5.5.4 Bin Migrations

The measured J/ψ p_T distribution corrected with the efficiency weight is parameterized in each rapidity slice by a smooth analytic function convoluted with a Gaussian distribution which represents the J/ψ p_T resolution. The p_T resolution was derived from data by using the equation [50]:

$$\sigma_{p_T}^{J/\psi} = p_T \frac{\sigma_m^{J/\psi}}{m^{J/\psi}}, \tag{5.10}$$

were $m^{J/\psi}$ is the mass resolution taken from the mass fit, and it is assumed that the p_T and mass resolutions are dominated by the muon p_T measurements. The integral of this function over p_T in each of the analysis p_T bins is calculated with and without the Gaussian smearing and the ratio of the two is the bin migration correction factor. At low p_T and rapidity the correction is around 0.1% and it increases at higher p_T and rapidity to around 3%. This is expected, because the muon momentum resolution gets worse as transverse momentum and rapidity increase as seen in Figure 5.7.

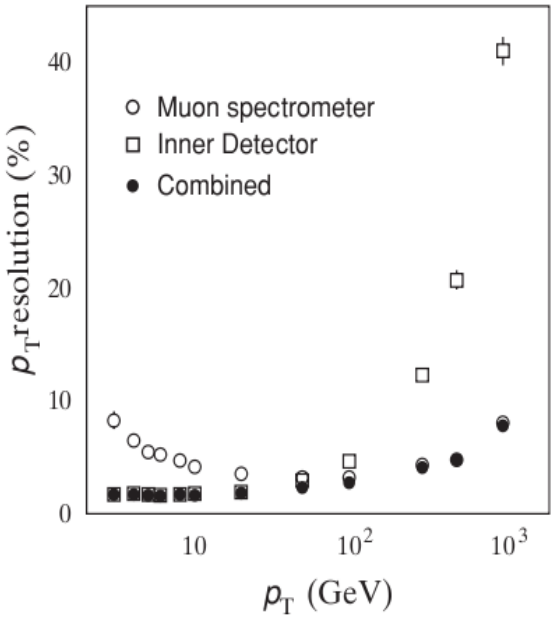

Figure 5.7 Expected performance of the ATLAS muon measurement from the Inner Detector, the Muon Spectrometer, and their combination together as a function of muon p_T [59].

Table 5.2 Rapidity and period dependent p_T thresholds.

Rapidity Slice	L1_MU0	EF_mu4	EF_mu6
$0 \leq \|y\| < 0.75$	0.0	7.0	9.0
$0.75 \leq \|y\| < 1.5$	0.0	6.0	8.0
$1.5 \leq \|y\| < 2.0$	0.0	5.5	7.5
$2.0 \leq \|y\| < 2.4$	0.0	6.0	8.0

5.5.5 Period Correction

Because we are combining data from three different triggers into a combined weighted histogram, we need to carefully consider the integrated luminosity in each bin. For example, the luminosity periods in which the EF_mu4 and EF_mu6 triggers are used do not contribute at all to the low J/ψ p_T bins because the low J/ψ p_T bins are populated entirely by low p_T muons. We have used a rapidity dependent p_T threshold for each trigger, described in Table 5.2, and calculated the integrated luminosity in each bin. The integrated luminosity in each bin is included in the per event weight.

5.6 Data Fit

A J/ψ mass histogram is created for each of the J/ψ p_T and y bins shown in Table A.4. For each di-muon that passes the selection cuts, the weight described in Equation 5.6 is put into the histogram. The total uncertainty of the weighted yield in each of the mass bins is described by the square root of the sum of the weights squared, $\sqrt{\sum_i w_i^2}$. Examples of the fit for different rapidity and p_T bins are shown in Figure 5.8 in the mass range from 2 to 4 GeV with 80 MeV bins.

The J/ψ candidate mass distribution is then fit with a binned minimum χ^2 fit. (A fit is preferred to simply counting the number above background, since it is more precise.) The χ^2 is the sum of the squared difference between the histogram value and the fitting function over each bin, divided by the uncertainty in the bin content. The J/ψ mass distribution is fit with a linear background function and a single Gaussian function for the J/ψ mesons and $\psi(2S)$ peaks, described in equation 5.11,

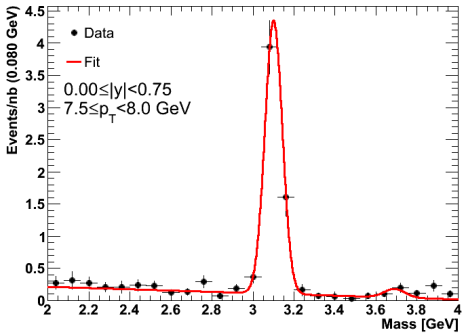

(a) Mass fit for $0 \leq |y| < 0.75$ and $7.5 \leq p_T < 8.0$ GeV.

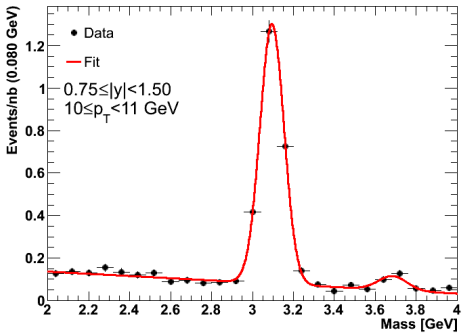

(b) Mass fit for $0.75 \leq |y| < 1.5$ and $10 \leq p_T < 11$ GeV.

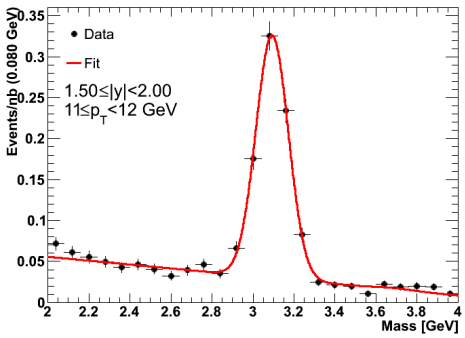

(c) Mass fit for $1.5 \leq |y| < 2$ and $11 \leq p_T < 12$ GeV.

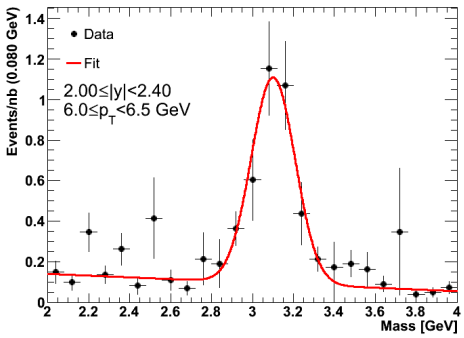

(d) Mass fit for $2 \leq |y| < 2.4$ and $6 \leq p_T < 6.5$ GeV.

Figure 5.8 Examples of J/ψ candidate mass fits with weights.

$$f_{\mu\mu} = N_{\text{bkg}}(1 + b(m_{\mu\mu} - 3.)) + N_{\text{sig}} G(m_{\mu\mu}; m_{J/\psi}, \sigma_{J/\psi}) + N_{\psi(2S)} G(m_{\mu\mu}; m_{\psi(2S)}, \sigma_{\psi(2S)}). \quad (5.11)$$

N_{bkg} and N_{sig} represent the background yield and J/ψ signal yield respectively, and b parameterizes the slope of the background. Note that the linear background equation is the sum of the first two Chebyshev polynomials and that the mass is shifted to the middle of the fit region to reduce correlations between the two background parameters: N_{bkg} and b. The second Gaussian describes the smaller $\psi(2S)$ mass distribution. Its yield is given by $N_{\psi(2S)}$.

The parameters m and σ are the central point and the standard deviation of the Gaussian. There are four such parameters in $f_{\mu\mu}$: $m_{J/\psi}$, $m_{\psi(2S)}$, $\sigma_{J/\psi}$, and $\sigma_{\psi(2S)}$; the mass and resolution for the J/ψ and $\psi(2S)$ distributions.

The χ^2 is minimized using the MINUIT software package [58]. MINUIT attempts to minimize

a given function by varying the parameters of the function. Starting values, initial step sizes, and limits of the parameters need to be chosen well to avoid getting stuck at a local minimum. The final fit results are checked against limits, to ensure that MINUIT found a true minimum.

The fit procedure is as follows. For each p_T and y analysis bin, we have the unweighted histogram and the weighted histogram. First the fit is done to the unweighted histogram and the parameters which minimize the χ^2 are saved. Then the fit is done for the weighted histogram. The starting values and steps for the weighted histogram are taken from the unweighted fit. This is done because the unweighted fit is less sensitive to starting values and step sizes, since in the unweighted histogram every event effectively has a weight of one and J/ψ candidates with large weight can cause problems if the starting values of the fit are too far from the optimal value. This works for every parameter except for N_{sig} and N_{bkg} because these should change when each event is weighted. We choose the starting value for these parameters by taking the average weight multiplied by the unweighted yield, as in equation 5.12.

$$y_{\text{start}} = w_{\text{avg}} y_{\text{unwgt}} \tag{5.12}$$

The mass position and σ for the $\psi(2S)$ peak are fixed to be the same as those of the J/ψ multiplied by the ratio of their masses, e.g. $\sigma_{\psi(2S)} = \frac{m^{\text{PDG}}_{\psi(2S)}}{m^{\text{PDG}}_{J/\psi}} \sigma_{J/\psi}$, in order to reduce the number of degrees of freedom in the fit. The scale is taken from the ratio of the $\psi(2S)$ and the J/ψ masses, but a scale of 1 was also tested, and the choice does not strongly affect the fitted values.

The limits for the J/ψ mass resolution parameter change depending on the rapidity range of the J/ψ since, as the rapidity increases, the resolution of the detector gets worse.

5.7 Uncertainties

There are many sources of uncertainty in the cross-section measurement; they are divided into two types, statistical and systematic uncertainties. Statistical uncertainties are random and come from the inherent precision limitations of the measurement; this type of uncertainty can be improved by increasing the number of observations. Systematic uncertainties reflect a bias inherent in the specific technique used to perform the measurement; this type of uncer-

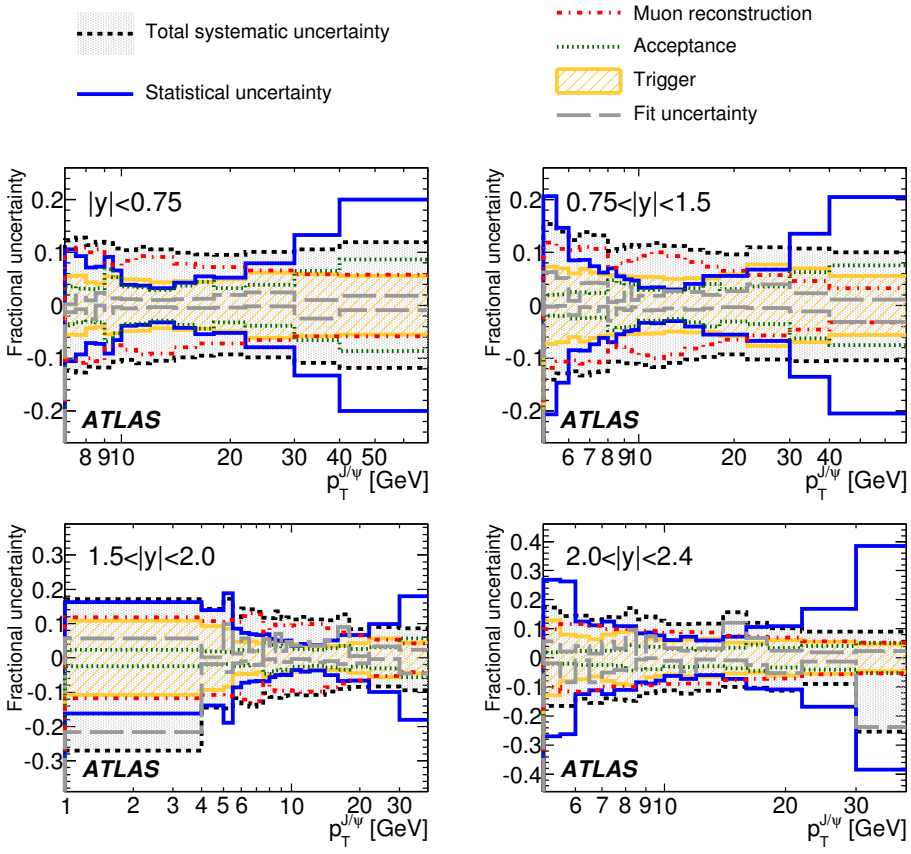

Figure 5.9 Fractional cross-section uncertainties in each p_T and y bin [49].

tainty cannot be improved by increasing the number of observations. Also, to ensure that the method of applying weights to events doesn't bias the weighted yield, several closure tests were performed on Monte Carlo, described in section 5.7.5.1.

We quantified the main sources of systematic uncertainty in the measurement of the double differential cross-section, which are, roughly in order of magnitude, J/ψ spin alignment, luminosity, offline muon reconstruction efficiency, trigger efficiency, acceptance, and fit method. All of the sources of uncertainty are described below in sections 5.7.1, 5.7.2, and 5.7.3, except for the luminosity uncertainty. The luminosity uncertainty is a constant 3.4% [32, 33]. The uncertainties in the cross-section in each of the rapidity ranges are shown in Figure 5.9.

5.7.1 Spin-Alignment Uncertainty

As described in section 2.4 the spin alignment of the produced J/ψ meson is not known for pp collisions at center of mass energy of 7 TeV at the LHC. The three parameters which determine the spin alignment (λ_θ, λ_ϕ, and $\lambda_{\theta\phi}$) were varied, but it was found that $\lambda_{\theta\phi}$ did not strongly affect the acceptance [49]. We use five different polarization assumptions to define an envelope in which the results can vary under all spin-alignment scenarios.

1. Isotropic alignment with $\lambda_\phi = \lambda_\theta = \lambda_{\theta\phi} = 0$.
2. Longitudinal alignment with $\lambda_\theta = -1, \lambda_\phi = \lambda_{\theta\phi} = 0$.
3. Transverse alignment with $\lambda_\theta = +1, \lambda_\phi = \lambda_{\theta\phi} = 0$.
4. Transverse alignment with $\lambda_\theta = +1, \lambda_\phi = +1, \lambda_{\theta\phi} = 0$.
5. Transverse alignment with $\lambda_\theta = +1, \lambda_\phi = -1, \lambda_{\theta\phi} = 0$.

The isotropic spin alignment is used for the nominal cross-section. The acceptance maps for each of the five hypotheses using the L1_MU0 acceptance cuts are shown in Figure 5.10. These distributions were obtained by reweighting the flat distribution from Monte Carlo with equation 2.8 and they show that at high J/ψ p_T there is a big difference in acceptance between longitudinally and transversely polarized J/ψ. We evaluate the cross-section using each of the different spin alignment hypotheses and take the maximal deviation in each of the analysis bins in order to form an envelope around the nominal value.

5.7.2 Weight Uncertainty

The weight uncertainties for each type of weight (acceptance, offline muon reconstruction, and trigger efficiency) are calculated in similar manner. Our knowledge of the acceptance and efficiency maps is limited by statistical uncertainty. The uncertainties are propagated through equation 5.6, and an uncertainty in the weight with respect to acceptance, offline, and trigger efficiency is calculated for each event. Then the average uncertainty over all of the events is calculated for each type of weight, for each p_T and y analysis bin. The fractional systematic uncertainty is the ratio of this average uncertainty to the average overall weight.

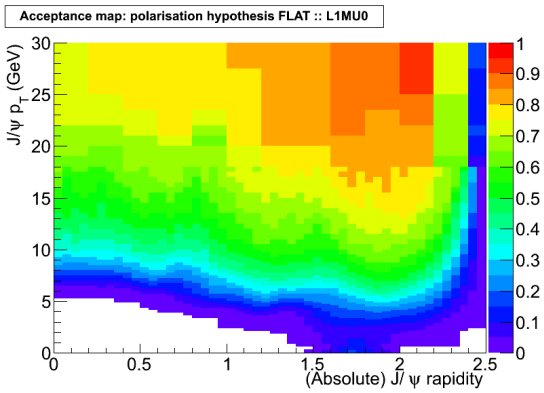

(a) Acceptance map with flat hypothesis.

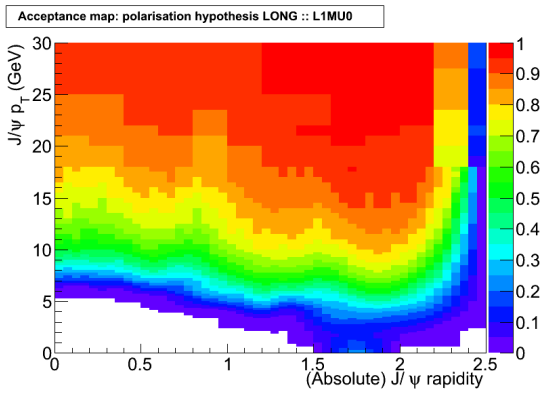

(b) Acceptance map with longitudinal hypothesis.

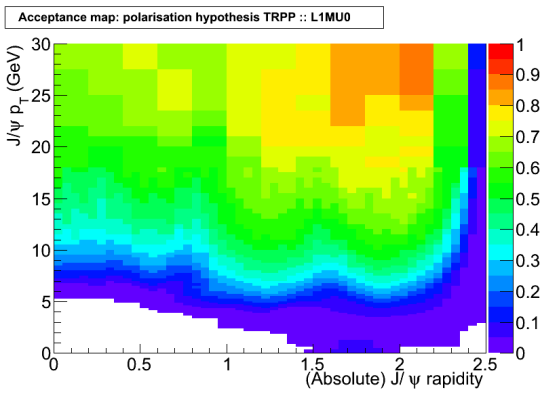

(c) Acceptance map with transverse plus hypothesis.

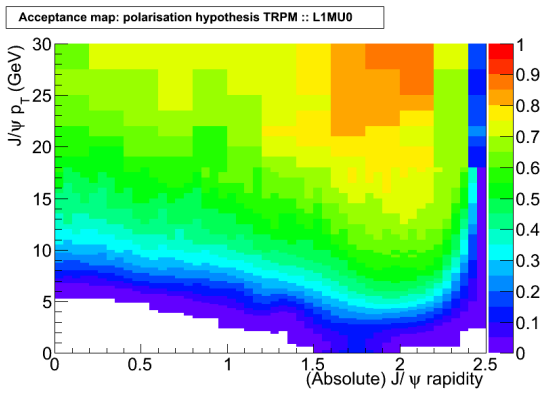

(d) Acceptance map with transverse minus hypothesis.

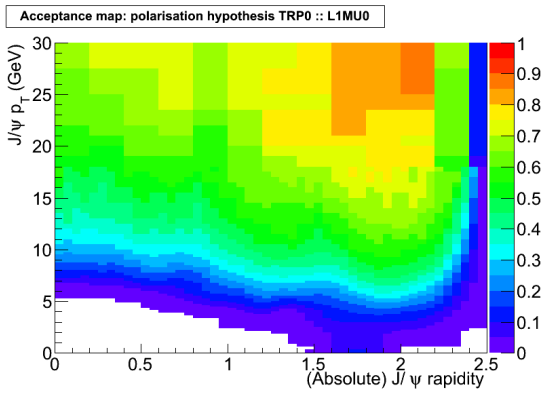

(e) Acceptance map with transverse zero hypothesis.

Figure 5.10 Acceptance maps in period L1_MU0 with five polarization hypotheses.

5.7.2.1 Error Propagation

The partial derivative of equation 5.6 is taken with respect to each of the efficiencies. For the offline efficiency, each is shown in equation 5.13.

$$\begin{aligned}
\frac{\partial w^{-1}}{\partial \epsilon_{\text{off}}{}^{c}_{+}} &= \mathcal{E}^{cc}_{\text{trig}} \epsilon_{\text{off}}{}^{c}_{-} + \mathcal{E}^{ct}_{\text{trig}} \epsilon_{\text{off}}{}^{t}_{-} \\
\frac{\partial w^{-1}}{\partial \epsilon_{\text{off}}{}^{c}_{-}} &= \mathcal{E}^{cc}_{\text{trig}} \epsilon_{\text{off}}{}^{c}_{+} + \mathcal{E}^{tc}_{\text{trig}} \epsilon_{\text{off}}{}^{t}_{+} \\
\frac{\partial w^{-1}}{\partial \epsilon_{\text{off}}{}^{t}_{+}} &= \mathcal{E}^{tc}_{\text{trig}} \epsilon_{\text{off}}{}^{c}_{-} \\
\frac{\partial w^{-1}}{\partial \epsilon_{\text{off}}{}^{t}_{-}} &= \mathcal{E}^{ct}_{\text{trig}} \epsilon_{\text{off}}{}^{c}_{+}
\end{aligned} \tag{5.13}$$

$\mathcal{E}_{\text{trig}}$ refers to the trigger component of the weight, given in equation 5.9, and w^{-1} is the inverse of the event weight, i.e. the probability to reconstruct the J/ψ candidate.

These partial derivatives can be combined to give the total offline uncertainty, in equation 5.14.

$$\Delta(w^{-1}) = \sqrt{\left(\frac{\partial w^{-1}}{\partial \epsilon_{\text{off}}{}^{c}_{+}} \Delta\epsilon_{\text{off}}{}^{c}_{+}\right)^2 + \left(\frac{\partial w^{-1}}{\partial \epsilon_{\text{off}}{}^{c}_{-}} \Delta\epsilon_{\text{off}}{}^{c}_{-}\right)^2 + \left(\frac{\partial w^{-1}}{\partial \epsilon_{\text{off}}{}^{t}_{+}} \Delta\epsilon_{\text{off}}{}^{t}_{+}\right)^2 + \left(\frac{\partial w^{-1}}{\partial \epsilon_{\text{off}}{}^{t}_{-}} \Delta\epsilon_{\text{off}}{}^{t}_{-}\right)^2} \tag{5.14}$$

Similarly, we can obtain the total trigger and acceptance uncertainties in the inverse weight. One more step is needed to find the uncertainty in the weight, again just taking the partial derivative of $\frac{1}{x}$ where x is w^{-1}, see equation 5.15. $\mathcal{E}_{\text{combined}}$ is given in equation 5.7.

$$\Delta w = \Delta(w^{-1}) \frac{w}{\mathcal{E}_{\text{combined}}} \tag{5.15}$$

5.7.2.2 Efficiency Uncertainties

The $\Delta\epsilon's$ in the previous section refer to the uncertainty in the efficiency value. The systematic uncertainties in the acceptance and efficiencies are relatively small compared to the statistical uncertainties. Figure 5.11 shows the offline efficiency and uncertainty obtained from tag-and-probe studies side-by-side.

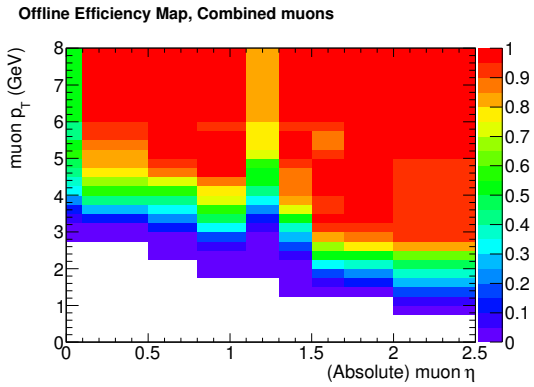

(a) Combined muon offline efficiency.

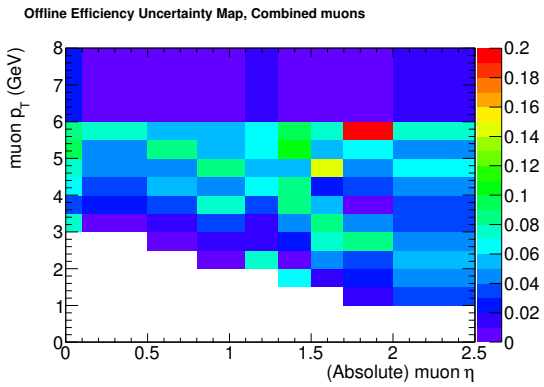

(b) Combined muon offline efficiency uncertainty.

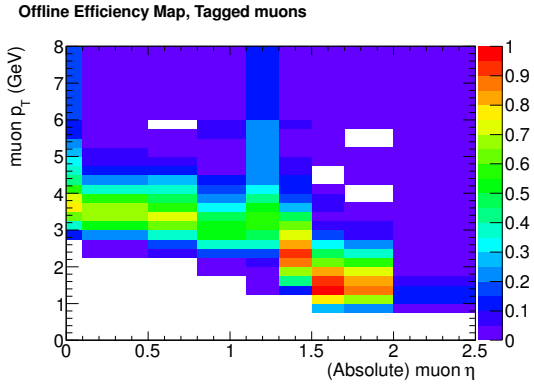

(c) Tagged muon offline efficiency.

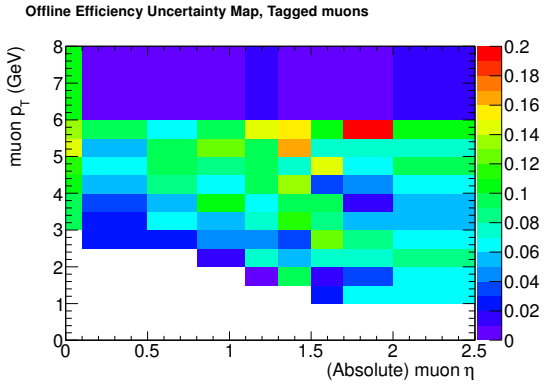

(d) Tagged muon offline efficiency uncertainty.

Figure 5.11 Offline efficiency uncertainty compared to the offline efficiency for combined and tagged muons.

5.7.3 Fit Uncertainty

The J/ψ yields are obtained from fitting the di-muon mass distribution in each of the analysis bins. There are alternative ways to do the fit than the method described in section 5.6 and the range of results using these different methods can be taken as the systematic uncertainty from the fit. We calculate this systematic uncertainty in the following way. In order to create a large sample of mass histograms to perform each fit variation on, we took the mass histogram in each analysis bin as a template. The yield in each mass histogram bin was moved up and down randomly according to equation 5.16:

$$m_{\text{new}} = m_{\text{old}} + r\sigma_m, \tag{5.16}$$

where r represents a randomly chosen value sampled from a unit Gaussian and σ_m represents the uncertainty in the yield in the mass histogram bin. We shook the mass histogram up in this way 256 times and then fit each of the histograms with the different fit variations. The range of values obtained from this fit forms an envelope around the nominal value and represents the fit uncertainty.

There are four different fit variations: the "base" fit function used for the nominal cross-section and three systematic variations. The three systematic variations are removing the $\psi(2S)$ from the nominal fit function and narrowing the mass fit range to 2.6 to 3.6 GeV, using a double Gaussian function for the mass peak, and using a quadratic background function. These three systematic variations test the sensitivity of the fit to the $\psi(2S)$ mass peak, our assumption of a single Gaussian resolution, and our assumption of a linear background shape, respectively.

The average difference in yield is taken in each analysis bin between the three systematic variations and the nominal value. (If the fit fails in one of the random variations, or runs into a parameter limit, that yield is excluded. This doesn't happen in most bins, but in some of the bins with a low number of J/ψ mesons it happens up to 5% of the time.) The ratio of the average difference in yield to the nominal value is the systematic uncertainty for the fit. The average systematic fractional uncertainty from the fitting method is few percent.

Figure 5.12 shows the yield in one of the analysis bins for each of the four variations (three systematic variations and the baseline fit). This shows that the distribution in yield is approximately Gaussian, and that fit variations are biased towards different yields. Figure 5.13 shows the residual of the three systematic variations with the baseline fit, which makes the bias of each fit variation from the nominal value more apparent.

5.7.4 Kinematic Dependence

Differences in the kinematic distribution of the J/ψ between data and Monte Carlo were studied in addition to differences in the p_T dependence between prompt and non-prompt components. A correction to the acceptance maps was made based on the measured non-prompt and prompt fraction to ensure the proper ratio of the two populations. The difference between

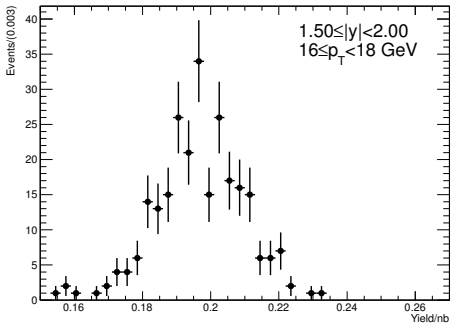

(a) Base value using nominal fit function.

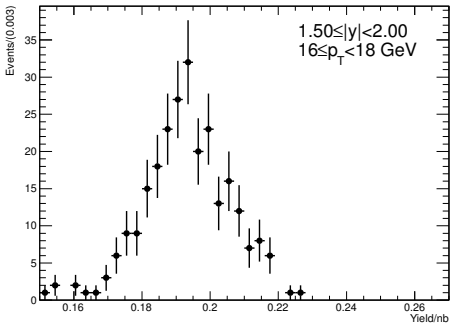

(b) No $\psi(2S)$ variation.

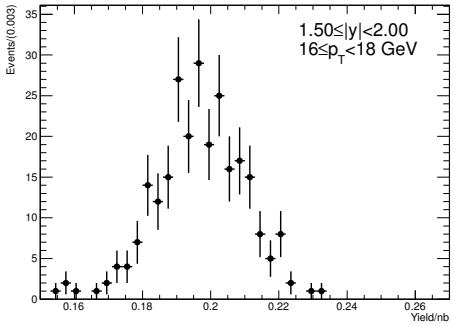

(c) Double Gaussian variation.

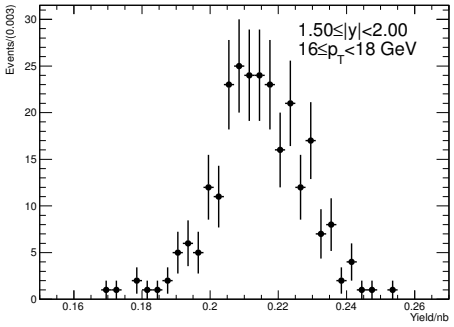

(d) Quadratic background variation.

Figure 5.12 Histograms of the yields from the 256 mass templates for each of the four fit variations, adjusted for the integrated luminosity in the bin.

the cross-section calculated with this correction factor and the nominal value is taken as a systematic uncertainty. This uncertainty is below 1% in most bins and is 1.5% at a maximum.

5.7.5 Systematic Tests

Some systematic cross-checks were done. The cross-checks include: other fit variations (decreasing the size of the mass bins, releasing the J/ψ σ parameter, and restricting the J/ψ mass parameter), fitting using a weighted maximum likelihood fit, using an efficiency calculated only from Monte Carlo with much finer binning, calculating the cross-section in each analysis period independently, and the closure test described below. These test indicated no problem with our method to extract the J/ψ differential cross-section.

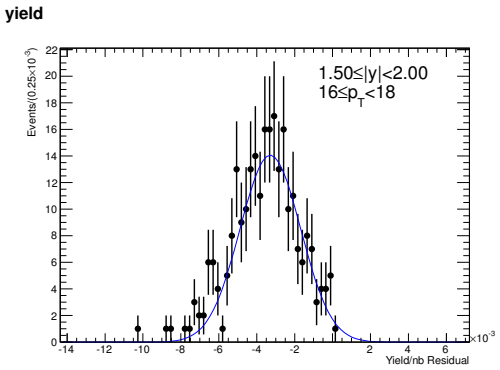

(a) No $\psi(2S)$ variation.

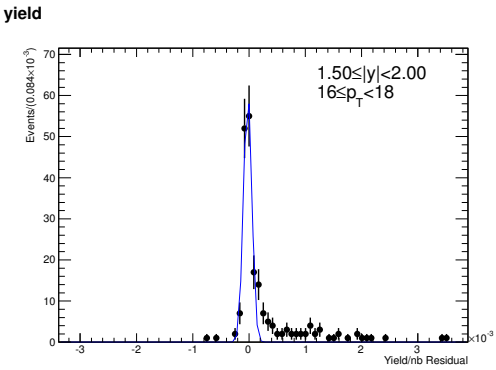

(b) Double Gaussian variation.

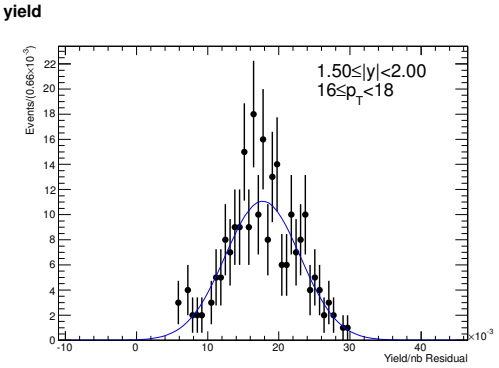

(c) Quadratic background variation.

Figure 5.13 Residuals of the three systematic variations from the nominal fit result ($y_{\text{syst}} - y_{\text{nominal}}$).

5.7.5.1 Closure Test

One can imagine this analysis as consisting of four steps of cuts applied cumulatively: the first is no cuts, the true number of $J/\psi \to \mu\mu$ decays; the second reduces the generated number of decays to the number in which the muons pass the acceptance cuts; the third is the number of decays where the muons were found by the offline muon reconstruction algorithm; and the fourth is the number of decays in which at least one of the muons passed the trigger algorithm used during the run period. At each step we can retrieve the number of J/ψ's in the previous step by applying weights: acceptance, offline efficiency, and trigger efficiency. We can then look at each step using Monte Carlo simulated events, and see if we recover the number of events before any cuts. This is what we call the closure test or tests.

The statistical and relevant systematic uncertainties were taken into account in the same

way as in data. The acceptance, trigger and offline muon reconstruction efficiency systematic uncertainties are used. The Monte Carlo simulates J/ψ's with a known polarization so the spin-alignment uncertainty does not need to be taken into account. As we simply count the number of J/ψ at each step, the fit uncertainty does not need to be taken into account (there is not enough background Monte Carlo for a full fit).

The statistical uncertainties in the yield come from the statistical error in the average weight, $\frac{\sigma}{\sqrt{N}}$, where σ is the standard deviation of the weights for the analysis p_T and y bin, and the uncertainties on the ratio of the yields at different steps is propagated from the yield uncertainties. The acceptance and efficiency uncertainty is described in more detail in section 5.7.2.

The final step closure test results, which combine all three stages of cuts with all three correcting weights, are summarized in Tables 5.3, 5.4, and 5.5 for each of the three trigger types we used. The values in this table are the ratio of the number of produced J/ψ from the first step (no cuts) to the number of J/ψ as calculated from the various efficiency maps applied at the fourth step (all cuts). This value should be 1 if there is closure. The results are consistent with expectation. There is a distinction in these tables between "Not used" and "No luminosity". For the higher threshold triggers, some analysis bins are excluded from the analysis since these trigger cuts don't allow any events in those bins; those bins are labeled "No luminosity". Other bins are excluded, even in the no threshold trigger (L1_MU0), because the acceptance cuts on the muon momentum remove enough J/ψ that a fit is no longer possible in data; those bins are labeled "Not used".

The closure test exposed problems in the analysis at an early stage. Some of the low p_T J/ψ bins did not close, an effect we traced to two causes: the trigger efficiency for the L1_MU0 period was very dependent on the muon charge for low p_T, and some of the bins in muon kinematic space had zero occupancy so that they could not be corrected. We solved these problems by using charge dependent trigger maps and removing some bins from the analysis at high rapidity, and through the carving cuts described in Tables A.1 and A.2.

Table 5.3 Total efficiency closure for L1_MU0.

	$J/\psi \|y\|$ $0-0.75$	$J/\psi \|y\|$ $0.75-1.50$	$J/\psi \|y\|$ $1.50-2.00$	$J/\psi \|y\|$ $2.00-2.40$
40. – 70. GeV	0.40 ± 0.23	1.19 ± 0.49	Not used	Not used
30. – 40. GeV	1.11 ± 0.38	1.09 ± 0.39	1.38 ± 0.68	1.36 ± 0.40
22. – 30. GeV	0.87 ± 0.27	1.02 ± 0.34	0.95 ± 0.41	0.67 ± 0.25
18. – 22. GeV	0.97 ± 0.28	0.94 ± 0.30	0.99 ± 0.41	1.00 ± 0.33
16. – 18. GeV	0.91 ± 0.26	1.01 ± 0.33	1.02 ± 0.40	1.04 ± 0.32
14. – 16. GeV	0.96 ± 0.25	0.94 ± 0.28	0.92 ± 0.34	0.95 ± 0.28
12. – 14. GeV	0.91 ± 0.22	1.02 ± 0.29	1.03 ± 0.33	1.01 ± 0.26
11. – 12. GeV	0.93 ± 0.22	0.99 ± 0.28	1.00 ± 0.30	1.01 ± 0.25
10. – 11. GeV	0.95 ± 0.20	0.97 ± 0.27	1.03 ± 0.29	0.92 ± 0.22
9.5 – 10. GeV	0.99 ± 0.20	0.88 ± 0.23	1.00 ± 0.26	0.83 ± 0.20
9.0 – 9.5 GeV	0.96 ± 0.18	0.91 ± 0.23	0.93 ± 0.24	1.65 ± 0.77
8.5 – 9.0 GeV	0.94 ± 0.15	1.01 ± 0.23	0.99 ± 0.24	0.93 ± 0.19
8.0 – 8.5 GeV	0.91 ± 0.12	1.05 ± 0.21	1.00 ± 0.22	0.86 ± 0.16
7.5 – 8.0 GeV	0.99 ± 0.12	1.06 ± 0.18	1.01 ± 0.20	0.98 ± 0.17
7.0 – 7.5 GeV	Not used	0.97 ± 0.15	0.96 ± 0.17	0.97 ± 0.15
6.5 – 7.0 GeV	Not used	1.05 ± 0.13	1.01 ± 0.16	0.93 ± 0.14
6.0 – 6.5 GeV	Not used	1.04 ± 0.11	0.97 ± 0.13	0.81 ± 0.10
5.5 – 6.0 GeV	Not used	1.08 ± 0.10	0.98 ± 0.12	0.94 ± 0.11
5.0 – 5.5 GeV	Not used	1.03 ± 0.09	1.02 ± 0.11	0.87 ± 0.09
4.0 – 5.0 GeV	Not used	Not used	1.03 ± 0.09	Not used
1.0 – 4.0 GeV	Not used	Not used	1.07 ± 0.06	Not used

5.8 Results

The measured inclusive J/ψ cross-section is shown in Figure 5.14. The 3.4% overall uncertainty from the luminosity measurement is not shown in the figure. The results agree well with CMS's results [61] which are also shown. CMS's measurement was performed with less integrated luminosity than our measurement. The uncertainty in our measurement primarily comes from the systematic uncertainty, except in the very low and high p_T bins. We also calculate the total cross-section for two wide bins, one which includes the entire rapidity range, but has a high p_T cut, and one which includes the entire p_T range, but in a narrow rapidity slice [49]. For $|y| < 2.4$ and $p_T > 7$ GeV, the cross-section times $J/\psi \to \mu\mu$ branching fraction is

$$\begin{aligned}\mathrm{Br}(J/\psi \to \mu\mu)\sigma(pp \to J/\psi X; |y| < 2.4, p_T > 7\mathrm{GeV}) \\ = 81 \pm 1(\mathrm{stat.}) \pm 10(\mathrm{syst.})^{+25}_{-20}(\mathrm{spin}) \pm 3(\mathrm{lumi.})\mathrm{nb}.\end{aligned}$$

Table 5.4 Total efficiency closure for EF_mu4.

	$J/\psi\ \|y\|$ $0-0.75$	$J/\psi\ \|y\|$ $0.75-1.50$	$J/\psi\ \|y\|$ $1.50-2.00$	$J/\psi\ \|y\|$ $2.00-2.40$
40. − 70. GeV	0.40 ± 0.23	1.12 ± 0.47	Not used	Not used
30. − 40. GeV	1.14 ± 0.42	1.13 ± 0.44	1.20 ± 0.58	1.43 ± 0.47
22. − 30. GeV	0.88 ± 0.28	0.97 ± 0.34	0.95 ± 0.42	0.56 ± 0.21
18. − 22. GeV	0.97 ± 0.29	0.96 ± 0.31	0.97 ± 0.40	1.01 ± 0.34
16. − 18. GeV	0.92 ± 0.27	1.01 ± 0.33	1.01 ± 0.39	1.01 ± 0.32
14. − 16. GeV	0.94 ± 0.25	0.93 ± 0.28	0.93 ± 0.34	0.96 ± 0.29
12. − 14. GeV	0.92 ± 0.22	0.99 ± 0.28	1.04 ± 0.33	0.98 ± 0.26
11. − 12. GeV	0.92 ± 0.22	0.98 ± 0.27	1.03 ± 0.30	0.98 ± 0.25
10. − 11. GeV	0.95 ± 0.21	0.96 ± 0.26	1.04 ± 0.29	0.95 ± 0.23
9.5 − 10. GeV	0.99 ± 0.21	0.89 ± 0.23	1.01 ± 0.26	0.81 ± 0.20
9.0 − 9.5 GeV	0.97 ± 0.18	0.94 ± 0.23	0.96 ± 0.24	0.98 ± 0.23
8.5 − 9.0 GeV	0.92 ± 0.14	1.02 ± 0.21	1.00 ± 0.23	0.81 ± 0.17
8.0 − 8.5 GeV	0.90 ± 0.12	1.03 ± 0.19	1.00 ± 0.21	0.80 ± 0.16
7.5 − 8.0 GeV	0.98 ± 0.12	1.01 ± 0.16	1.03 ± 0.20	0.97 ± 0.19
7.0 − 7.5 GeV	1.03 ± 0.11	0.98 ± 0.14	0.95 ± 0.16	0.71 ± 0.11
6.5 − 7.0 GeV	No luminosity	1.02 ± 0.12	0.94 ± 0.13	0.79 ± 0.12
6.0 − 6.5 GeV	No luminosity	1.00 ± 0.10	0.92 ± 0.10	0.67 ± 0.09
5.5 − 6.0 GeV	No luminosity	No luminosity	0.92 ± 0.08	No luminosity

Table 5.5 Total efficiency closure for EF_mu6.

	$J/\psi\ \|y\|$ $0-0.75$	$J/\psi\ \|y\|$ $0.75-1.50$	$J/\psi\ \|y\|$ $1.50-2.00$	$J/\psi\ \|y\|$ $2.00-2.40$
40. − 70. GeV	0.26 ± 0.18	1.06 ± 0.45	Not used	Not used
30. − 40. GeV	1.08 ± 0.41	1.07 ± 0.46	1.13 ± 0.54	1.67 ± 0.77
22. − 30. GeV	0.89 ± 0.30	0.93 ± 0.34	0.92 ± 0.42	0.55 ± 0.24
18. − 22. GeV	0.96 ± 0.29	0.98 ± 0.33	0.98 ± 0.40	1.01 ± 0.35
16. − 18. GeV	0.91 ± 0.27	0.95 ± 0.32	1.07 ± 0.41	0.99 ± 0.32
14. − 16. GeV	0.95 ± 0.27	0.90 ± 0.28	0.93 ± 0.34	0.94 ± 0.29
12. − 14. GeV	0.95 ± 0.23	1.01 ± 0.28	1.06 ± 0.33	0.91 ± 0.24
11. − 12. GeV	0.91 ± 0.20	1.01 ± 0.25	0.98 ± 0.26	0.97 ± 0.24
10. − 11. GeV	0.99 ± 0.18	0.99 ± 0.21	1.01 ± 0.24	0.86 ± 0.19
9.5 − 10. GeV	1.02 ± 0.17	0.88 ± 0.17	1.01 ± 0.22	0.78 ± 0.18
9.0 − 9.5 GeV	1.07 ± 0.20	0.93 ± 0.16	0.94 ± 0.19	0.83 ± 0.18
8.5 − 9.0 GeV	No luminosity	1.08 ± 0.17	0.95 ± 0.17	0.75 ± 0.14
8.0 − 8.5 GeV	No luminosity	0.99 ± 0.14	0.83 ± 0.13	0.79 ± 0.16
7.5 − 8.0 GeV	No luminosity	No luminosity	0.74 ± 0.11	No luminosity

For $1.5 \leq |y| < 2$ and $p_T > 1$ GeV, the cross-section times $J/\psi \to \mu\mu$ branching fraction is

$$\begin{aligned}&\mathrm{Br}(J/\psi \to \mu\mu)\sigma(pp \to J/\psi X; 1.5 \leq |y| < 2, p_T > 1\mathrm{GeV}) \\ &\quad = 510 \pm 70(\mathrm{stat.})^{+80}_{-120}(\mathrm{syst.})^{+920}_{-130}(\mathrm{spin}) \pm 20(\mathrm{lumi.})\mathrm{nb}.\end{aligned}$$

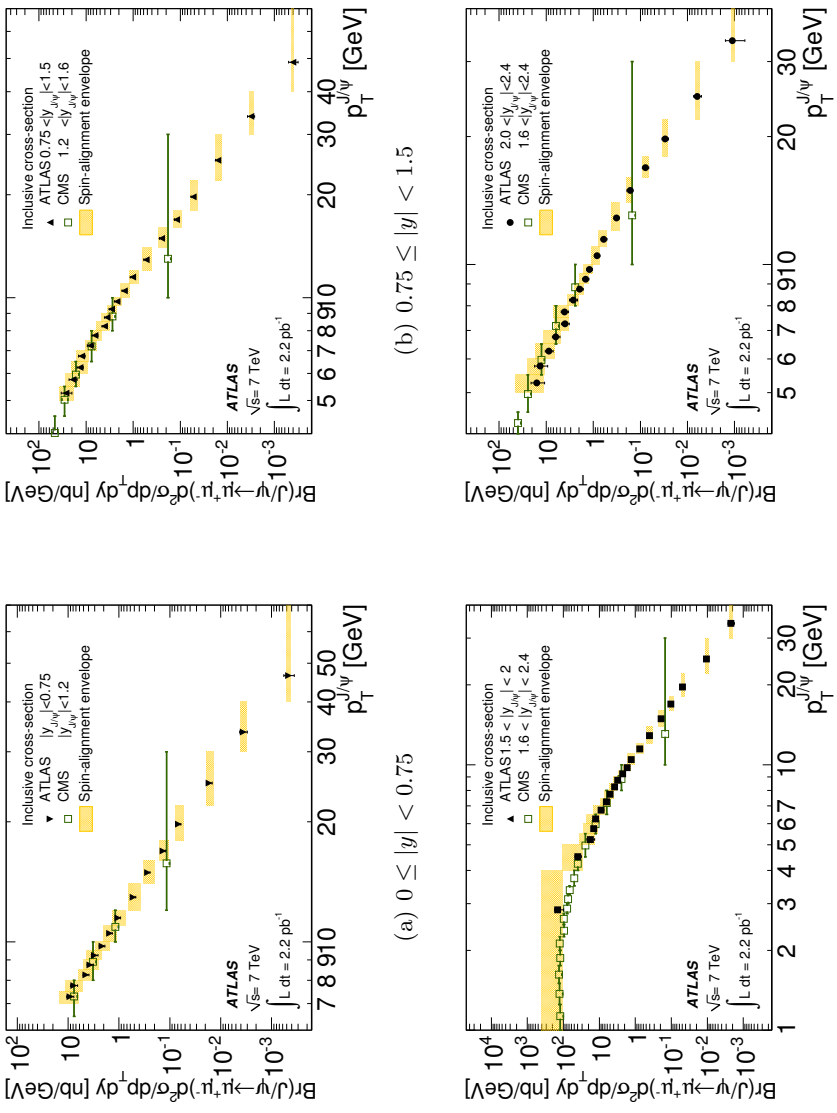

(a) $0 \leq |y| < 0.75$

(b) $0.75 \leq |y| < 1.5$

(c) $1.5 \leq |y| < 2$

(d) $1.5 \leq |y| < 2.4$

Figure 5.14 Inclusive differential cross-section for ATLAS and CMS. The yellow overlaid band is the spin-alignment systematic uncertainty [49].

CHAPTER 6. J/ψ Non-prompt Fraction

In pp collisions at ATLAS J/ψ mesons can be produced either promptly through strong or electromagnetic processes, or non-promptly through the weak decay of a b hadron.[1] The weak decay is much slower than the strong processes. It is so much slower that the distance between the b-hadron production point and the b-hadron decay point into a J/ψ can be measured with the Pixel detector. The measurement of the fraction of non-promptly produced J/ψ meson to the total number of J/ψ mesons we call the fraction measurement, and the quantity will be referred to as $\mathcal{R} = \frac{\sigma(pp\to b\bar{b}X\to J/\psi X')}{\sigma(pp\to J/\psi X'')_{\text{prompt}}+\sigma(pp\to b\bar{b}X\to J/\psi X')}$, where $X(')('')$ is an arbitrary byproduct of the decay [49].

6.1 Pseudo-proper time

The quantity that we use to discriminate prompt from non-prompt J/ψ is the transverse distance between the b-hadron decay vertex and the primary pp collision vertex projected onto the J/ψ momentum. The transverse decay length is denoted by

$$L_{xy} = \frac{(\overrightarrow{v}_{\text{sec}} - \overrightarrow{v}_{\text{prim}}) \cdot \overrightarrow{p}_T^{J/\psi}}{|\overrightarrow{p}_T^{J/\psi}|}. \tag{6.1}$$

Here $\overrightarrow{v}_{\text{sec}}$ and $\overrightarrow{v}_{\text{prim}}$ represent the three-dimensional position of the vertices as found by the track reconstruction algorithms. The track reconstruction algorithms identify vertices by determining where reconstructed ID tracks intersect. Sometimes more than one vertex is found; the average number of vertices in each event range from ≈ 1.5 in the first data taking period studied in this analysis to ≈ 1.9 in the last. In the case where there are multiple vertices, they are ordered according to the sum of the p_T^2 of the ID tracks which belong to them. The

[1] Prompt J/ψ can be produced two ways: directly in the pp collisions, or indirectly through a feed-down decay from heavier charmonium, such as $\chi_{c0}\to\gamma J/\psi$.

vertices can occur anywhere in the "luminous region" which is cigar shaped and has dimensions of about 2.5μm in the transverse plane and 60 mm in the longitudinal plane.

The primary vertex used to calculate L_{xy} is the one built from the J/ψ candidate's ID tracks, however, that vertex is recalculated with the ID tracks from the J/ψ candidate removed. There is no ambiguity in this choice of primary vertex because we require that each of the ID tracks that form the J/ψ candidate were used to reconstruct the same primary vertex. The J/ψ decay vertex comes from an algorithm that fits the two J/ψ muons' ID tracks with a vertex constraint, using a χ^2 fit, and it returns a covariance matrix of the track parameters that went into the fit [62]. In addition, the track reconstruction algorithm calculates an expected uncertainty on the primary vertex position. From these covariance matrices we calculate an expected uncertainty in the measured L_{xy} by propagating the errors according to the following equation:

$$\sigma_f^2 = \sum_{i=1}^{N}\sum_{j=1}^{N}\left(\frac{\partial f}{\partial x_i}\right)\left(\frac{\partial f}{\partial x_j}\right)\sigma_i\sigma_j \mathrm{cov}(i,j), \tag{6.2}$$

where the quantity f is a function of N variables x_i, σ_f is the uncertainty in f and σ_i is the uncertainty in variable x_i, and $\mathrm{cov}(i,j)$ is the covariance between variables x_i and x_j. The biggest contribution to the uncertainty is the uncertainty in the J/ψ decay vertex position. Figure 6.1 shows the L_{xy} and the uncertainty in L_{xy} for an example analysis bin. L_{xy} is on the order of 1 mm, and the L_{xy} uncertainty is on the order of 0.1 mm.

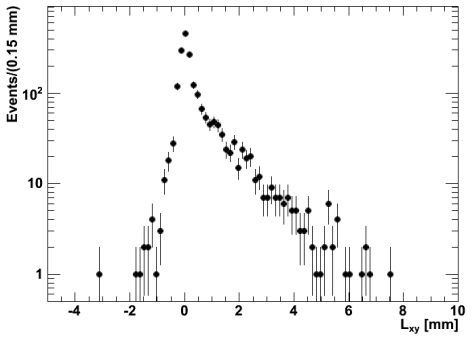

(a) J/ψ L_{xy} for $10 < p_T^{J/\psi} < 11$ GeV and $1.5 < |y| < 2.0$.

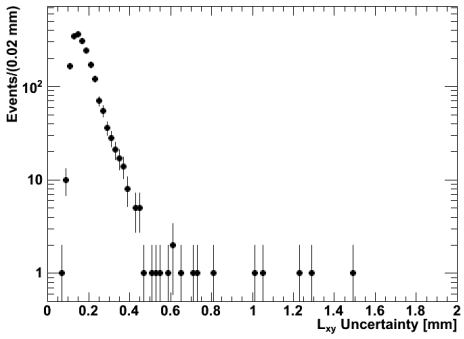

(b) J/ψ L_{xy} uncertainty for $10 < p_T^{J/\psi} < 11$ GeV and $1.5 < |y| < 2.0$.

Figure 6.1 J/ψ L_{xy} and L_{xy} uncertainty.

The probability for the decay of a b hadron as a function of time follows an exponential distribution:

$$\frac{1}{\tau_b}\exp\left(\frac{-t}{\tau_b}\right), \tag{6.3}$$

where τ_b is the lifetime of the b hadron (on the order of 10^{-12} seconds for all b hadrons), and the proper decay time, t, is $\frac{L}{c\beta\gamma}$, where L is the total distance between the b-hadron production and decay points, and $\beta\gamma$ is the Lorentz factor. Then the proper decay time can be found by taking the projection into the transverse plane: $t = \frac{L_{xy}m^b}{p_T^b}$. However, we are measuring the inclusive J/ψ production and do not reconstruct the b hadron completely. Instead of the proper time, we calculate the pseudo-proper time (also referred to as τ),

$$\tau = \frac{L_{xy}m_{\rm PDG}^{J/\psi}}{p_T^{J/\psi}}, \tag{6.4}$$

where $m_{\rm PDG}^{J/\psi}$ is the mass of the J/ψ meson averaged by the Particle Data Group [4]. The τ distribution is approximately exponential at high $p_T^{J/\psi}$, where most of the b-hadron transverse momentum is carried by the J/ψ, and at low $p_T^{J/\psi}$ the exponential distribution is smeared [49]. Using the covariance matrices from the secondary vertex finding tool and the primary vertex finding tool, the expected uncertainty in τ, δ_τ, is calculated, along with the expected uncertainty in the calculated J/ψ invariant mass, δ_m.

The selection of the J/ψ candidates is the same as the selection for the cross-section measurement except for the primary vertex cut described above, the requirement that the reconstructed J/ψ invariant mass is between 2.5 and 3.5, to remove contamination of the τ distribution from $\psi(2S)$, and a different trigger selection that results in an integrated luminosity of 2.3 pb^{-1} (the J/ψ inclusive cross-section measurement used 2.2 pb^{-1}).

The trigger selection for the $\mathcal{R}$ measurement is similar to the selection in the cross-section measurement, however, multiple triggers are used since the trigger efficiencies will cancel. In the first data taking period, the L1_MU0 trigger is used, as in the J/ψ cross-section measurement, and another trigger called here the "minimum-bias" trigger is also used. [2] If either of these

[2] The "minimum-bias" trigger only requires two hits on either side of the "Minimum-Bias Trigger Scintillator", which extends from $2.09 < |\eta| < 3.84$.

two trigger requirements are met, the event is accepted. In the later two periods, if either the EF_mu4, EF_mu6, or EF_mu10 trigger requirements are met, the event is kept. [3] We use the EF_mu10 trigger in addition to the lower threshold triggers because at the end of the last data taking period the EF_mu6 trigger was prescaled, and the EF_mu10 trigger will allow some more events to be kept. Figure 6.2 shows the J/ψ pseudo-proper time in the four different rapidity bins.

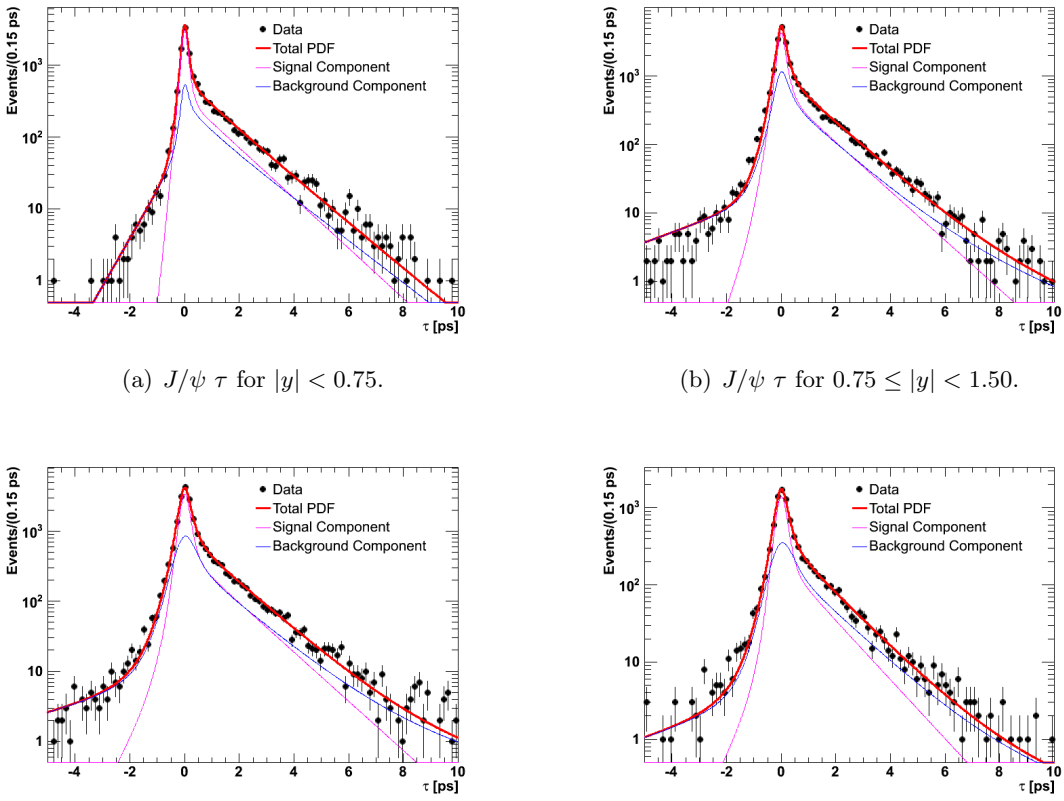

(a) J/ψ τ for $|y| < 0.75$.

(b) J/ψ τ for $0.75 \leq |y| < 1.50$.

(c) J/ψ τ for $1.50 \leq |y| < 2.00$.

(d) J/ψ τ for $2.00 \leq |y| < 2.40$.

Figure 6.2 J/ψ pseudo-proper time with full event selection in different rapidity ranges. The red curve is the fit of the pseudo-proper time described in Section 6.2, and the blue and magenta lines are the background and signal fractions determined by the fit.

[3] In the J/ψ cross-section measurement, the EF_mu4 trigger was used in the second data period, and the EF_mu6 trigger was used in the last data period.

6.2 Mass and Pseudo-Proper Time Fit

We use an unbinned maximum likelihood fit to determine $\mathcal{R}$. "Unbinned" means that the data is not binned (unlike in the cross-section measurement), and the likelihood is defined by the following relation:

$$\ln \mathcal{L} = \sum_{i=1}^{N_{\text{events}}} \ln p(x_i^0, x_i^1, x_i^2, ...; c^0, c^1, c^2). \tag{6.5}$$

N_{events} is the number of J/ψ candidates and p is the estimated probability distribution function (PDF) for reconstructing the event. p depends on certain input parameters of the event, $\{x^k\}$, and certain parameters which may be varied $\{c^k\}$. The parameters $\{c^k\}$ are varied in order to maximize the log-likelihood, $\ln \mathcal{L}$, which is equivalent to maximizing the likelihood. Therefore, the maximum likelihood fit determines which combination of parameters $\{c^k\}$ gives a PDF which most closely matches the data. $\mathcal{R}$ will be one of the parameters which is varied. The maximization is done by the MINUIT software package [58].

For our particular fit there are four input parameters, the invariant mass, pseudo-proper time, and the estimated uncertainties on both: $\{m_{\mu\mu}, \delta_m, \tau, \delta_\tau\}$. The mass and pseudo-proper time are fit simultaneously, so the signal to background ratio determined mostly from the mass PDF is practically used as an input to the τ fit, as described by the following equation:

$$p(m_{\mu\mu}, \tau|\delta_m, \delta_\tau) = f_{\text{sig}} T_{\text{sig}}(\tau|\delta_\tau) M_{\text{sig}}(m_{\mu\mu}|\delta_m) + (1 - f_{\text{sig}}) T_{\text{bkg}}(\tau|\delta_\tau) M_{\text{bkg}}(m_{\mu\mu}|\delta_m). \tag{6.6}$$

f_{sig} is the fraction of signal J/ψ candidates in the fit region, T_{sig} is the signal pseudo-proper time PDF, M_{sig} is the signal mass PDF, T_{bkg} is the background pseudo-proper time PDF, and M_{bkg} is the background mass PDF. The PDF's are described in greater detail in the following subsections. The probability is a function of mass and pseudo-proper time, and the probability distribution is normalized to one with respect to these two variables. The probability is a conditional probability with respect to the uncertainties in mass and pseudo-proper time, however, the prior distribution of the uncertainties is assumed to be uniform and does not play a role in the fit. With more statistics a different prior distribution may be used.

6.2.1 Mass Fit

The mass PDF is similar to the one used for the cross-section analysis: the signal component, M_{sig}, is a Gaussian function, and the background component, M_{bkg}, is a second degree polynomial. The main difference is that the expected uncertainty in the invariant mass is used in the Gaussian function. This number is determined by the secondary vertex fitter as described above. Our expectation of the uncertainty may be wrong (e.g. if the estimation of the ID track parameter uncertainties are biased), so an overall scale factor is assigned to the uncertainty, making the standard deviation of the Gaussian $S_m\delta_m$.

There are four fitted parameters in the mass PDF: the mean J/ψ mass, $m^{J/\psi}$; the mass uncertainty scale factor, S_m; and the two parameters which specify the second-degree polynomial of the Gaussian, c^1 and c^2 (the zeroth degree component is absorbed into the overall normalization).

6.2.2 Pseudo-proper Time Fit

The pseudo-proper time PDF is composed of signal and background components. The signal component consists of prompt and non-prompt terms as shown in Equation 6.7:

$$T_{\text{sig}}(\tau|\delta_\tau) = f_{\text{np}}T_{\text{np}}(\tau|\delta_\tau) + (1 - f_{\text{np}})T_{\text{p}}(\tau|\delta_\tau). \tag{6.7}$$

f_{np} is the non-prompt fraction, T_{np} is the non-prompt PDF, and T_{p} is the prompt PDF. The prompt PDF is a delta function convoluted with a Gaussian resolution function, while the non-prompt PDF is an exponential distribution, like in Equation 6.3, convoluted with the same Gaussian resolution function as used for the prompt component:

$$T_{\text{p}} = R(\tau' - \tau, S_\tau^{\text{sig}}\delta_\tau) \otimes \delta(\tau'), \tag{6.8}$$

$R(\tau'-\tau, S_\tau^{\text{sig}}\delta_\tau)$ is the Gaussian resolution function. The standard deviation of the Gaussian is constructed similarly to the mass PDF; the uncertainty calculated from the track and vertex covariance matrices is multiplied by a scale factor, $\sigma_\tau = S_\tau^{\text{sig}}\delta_\tau$. The non-prompt component is

$$T_{\rm np} = R(\tau' - \tau, S_\tau^{\rm sig}\delta_\tau) \otimes E(\tau'; \tau_b), \tag{6.9}$$

where $E(\tau'; \tau_b) = \frac{1}{\tau_b}\exp(\frac{-\tau'}{\tau_b})$ is the exponential distribution for the non-prompt component, and τ_b is the effective slope of the non-prompt exponential. Sketches of the non-prompt and prompt components of the signal pseudo-proper time PDF are shown in Figures 6.3(a) and 6.3(c).

There are three free parameters in the signal pseudo-proper time fit: the non-prompt fraction, $f_{\rm np}$; the slope of the exponential, τ_b; and the signal τ uncertainty scale factor, $S_\tau^{\rm sig}$.

The background component is an empirical parameterization that matches the background in the sideband mass regions. The long-lived background component is modeled with a double-sided exponential and a single-sided exponential, while the short-lived component is modeled with a delta function. Each component is convoluted with a Gaussian background resolution function:

$$T_{\rm bkg} = R(\tau' - \tau, S_\tau^{\rm bkg}\delta_\tau) \otimes \left((1 - b_d - b_s)\delta(\tau') + b_d \exp\left(\frac{-|\tau'|}{\tau_d}\right) + b_s \exp\left(\frac{-\tau'}{\tau_s}\right)\right). \tag{6.10}$$

b_d is the fraction of the background PDF for the double-sided exponential, b_s is the fraction for the single-sided exponential, τ_d and τ_s are the slopes for each, respectively, and $S^{\rm bkg}$ is the uncertainty scale factor for the background resolution function. These five parameters are free to be varied by the fit. Examples of the single-sided, double-sided, and delta components of the background PDF are shown in Figures 6.3(a), 6.3(b), and 6.3(c).

Figure 6.4 shows an example of the simultaneous mass and pseudo-proper time fit in the bin with $10 < p_T^{J/\psi} < 11$ GeV and $1.5 < |y| < 2.0$. The pseudo-proper time likelihood is projected for two separate mass regions, a signal mass region from $2.9 - 3.3$ GeV, shown in Figure 6.4(a), and a background region from $2.5 - 3.5$ GeV and excluding the signal region, shown in Figure 6.4(b).

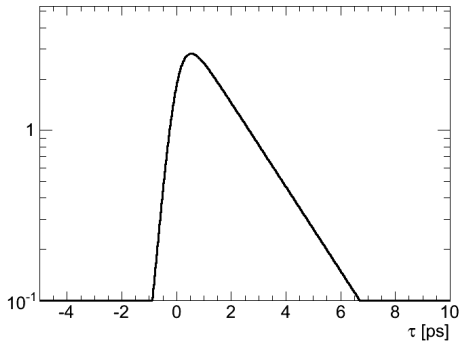

(a) Single-sided exponential convoluted with a Gaussian function.

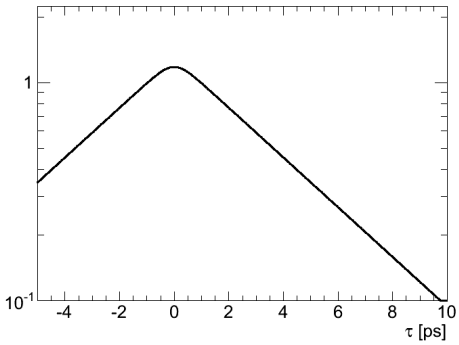

(b) Double-sided exponential convolved with a Gaussian function.

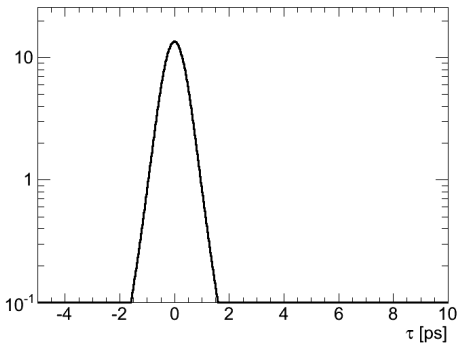

(c) Delta function convoluted with a Gaussian function.

Figure 6.3 The three basic functional components of the J/ψ pseudo-proper time PDF.

6.3 Uncertainties

The relative systematic uncertainty in the $\mathcal{R}$ measurement is less than in the cross-section measurement because most systematic uncertainties tend to affect the prompt and non-prompt components equally and thus cancel. Still some sources of uncertainty remain; the different polarization of the prompt and non-prompt components (and thus the different acceptance), and the uncertainty in the fitting procedure contribute significantly to the systematic uncertainty [49].

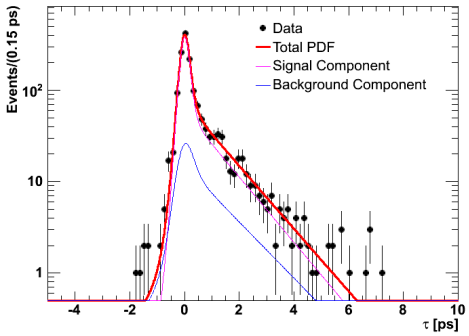

(a) Pseudo-proper time projected into the signal mass region from $2.9 - 3.3$ GeV, in the bin $10 < p_T^{J/\psi} < 11$ GeV and $1.5 < |y| < 2.0$.

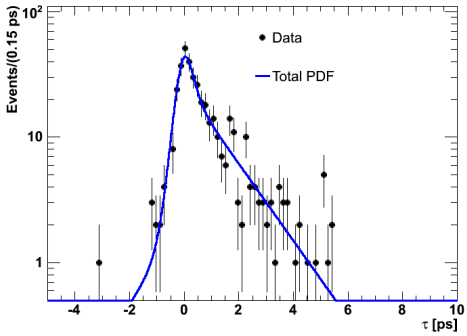

(b) Pseudo-proper time projected into the background mass region from $2.5-2.9$ and $3.3-3.5$ GeV, in the bin $10 < p_T^{J/\psi} < 11$ GeV and $1.5 < |y| < 2.0$.

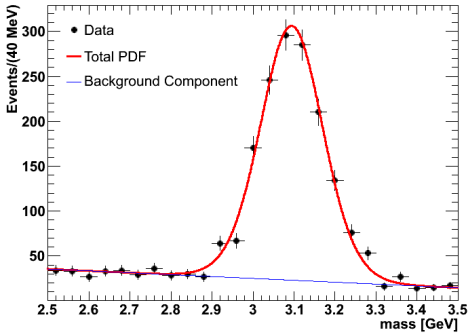

(c) Mass fit in the mass region $2.5 - 3.5$ GeV.

Figure 6.4 PDF's for the simultaneous mass and pseudo-proper time fit in the analysis bin from $10 < p_T^{J/\psi} < 11$ and $1.5 < |y| < 2.0$.

6.3.1 Spin-Alignment Uncertainty

Since the prompt and non-prompt signal components are polarized differently, the acceptance correction for each is different. The nominal $\mathcal{R}$ was calculated assuming the prompt and non-prompt components have an equal acceptance correction. Then an envelope around this nominal value was evaluated similarly to the cross-section in Section 5.7.1. If we take the number of prompt and non-prompt J/ψ as $N_{\rm p}$ and $N_{\rm np}$, respectively, then

$$\frac{N_{\rm p}}{N_{\rm np}} = \frac{1}{f} - 1, \tag{6.11}$$

where f is

$$f = \frac{N_{\mathrm{np}}}{N_{\mathrm{p}} + N_{\mathrm{np}}}. \tag{6.12}$$

The average value of the acceptance under different polarization assumptions is calculated in each analysis bin and the ratio of the average isotropic acceptance to the average of one of the other acceptance choices is α. Then $\mathcal{R}'$ under these polarization assumptions is

$$\mathcal{R}' = \frac{1}{1 + \alpha \frac{N_{\mathrm{p}}}{N_{\mathrm{np}}}}. \tag{6.13}$$

For the uncertainty in the prompt J/ψ meson polarization, and hence acceptance, an envelope with all four spin-alignment scenarios from Section 5.7.1 is made against an isotropic non-prompt spin alignment. This is the largest uncertainty in the $\mathcal{R}$ measurement, roughly 5%.

The possible variation in the non-prompt spin alignment is expected to be much smaller than for prompt J/ψ decays for two reasons: most of the produced b-mesons are pseudoscalar particles which have no spin, and therefore cannot be polarized (only the Λ_b b-baryon has integer spin), and the averaging effect of the admixture of different b-hadron decays. Therefore the non-prompt spin-alignment uncertainty is the difference between the isotropic, central $\mathcal{R}$ value and the $\mathcal{R}$ value calculated from acceptance maps reweighted with the CDF result for $B \to J/\psi$ spin alignment [63]. This only contributes an additional uncertainty of 0.4% at maximum.

6.3.2 Fit Uncertainty

The fit is repeated with different changes to the fitting procedure in order to estimate the systematic uncertainty from our choice of PDF [49].

- The background exponential for the nominal $\mathcal{R}$ value is composed of a symmetric double-sided exponential and a single-sided exponential. We vary the symmetrical double-sided exponential to an asymmetric double-sided exponential, with separate slopes for the positive and negative sides. We further vary the background PDF by using two asymmetric

double-sided exponentials which are constrained for negative τ's to have the same exponential slope. The maximum deviation from the nominal value of $\mathcal{R}$ for these two variations is taken as a systematic uncertainty.

- The single τ Gaussian resolution function used for the nominal value of $\mathcal{R}$ is changed to a double Gaussian resolution. In this variation there are two different scale factors for each Gaussian. The difference from the nominal value is used as the systematic uncertainty in $\mathcal{R}$.

- The nominal J/ψ background mass PDF uses a second-degree polynomial for the nominal value and two variations of this are tested using first-degree and third-degree polynomials. The maximum deviation around the nominal value for these two variations is taken as a systematic uncertainty.

6.3.3 Kinematic Dependence

Differences in the momentum spectra between prompt and non-prompt J/ψ lead to different average acceptances in an analysis bin. A correction factor is derived from the acceptance maps with and without momentum reweighting to take into account the differences between prompt and non-prompt J/ψ. The difference between $\mathcal{R}$ calculated with this correction factor and without is taken as a systematic uncertainty [49].

6.3.4 Systematic Tests

Several cross-checks are done to ensure that the results are consistent and no problem is found with the method to extract $\mathcal{R}$, and no corresponding systematic uncertainty is assigned [49].

- The fit mass range is expanded to include the region from $3.8 - 4.0$ GeV but still exclude the $\psi(2S)$ region from $3.5 - 3.8$ GeV.

- For the nominal $\mathcal{R}$ measurement, the primary vertex is chosen as the one reconstructed with both of the muon tracks (among others), and when the two muon tracks form two

different primary vertices, the event is rejected; two different choices of primary vertex are used: the primary vertex with the highest summed p_T^2 of the tracks that form it, but never rejecting any events, and using the primary vertex with the highest summed p_T^2 again, but rejecting events when this vertex was not reconstructed with the two muon tracks.

- Pull distributions were made using parameterized Monte Carlo trial experiments called Toy Monte Carlo. The pull is defined as

$$\Delta = \frac{\mathcal{R}_{\text{extracted}} - \mathcal{R}_{\text{generated}}}{\sigma(\mathcal{R}_{\text{extracted}})}, \tag{6.14}$$

where $\mathcal{R}_{\text{generated}}$ is the non-prompt fraction with which the Toy Monte Carlo was generated and $\mathcal{R}_{\text{extracted}}$ and $\sigma(\mathcal{R}_{\text{extracted}})$ are the value and the uncertainty determined by the fit. The mass and τ PDF was used to generate 100 "experiments" in each of the analysis bins, with approximately the same number of events in each bin as in data. Each bin is then fit with the mass and τ maximum likelihood fit as in data, and the pull is computed for each "experiment." The mean and sigma of the pull is consistent with zero and one, as expected for no bias.

6.4 Results

The $\mathcal{R}$ measurement is combined with the inclusive J/ψ cross-section measurement and we can extract the non-prompt and prompt differential cross-sections. Where it is applicable, the p_T analysis bins in the inclusive cross-section measurement are merged to align the cross-section analysis bins with the $\mathcal{R}$ analysis bins. The relative systematic uncertainties in each of the two measurements are combined under the assumption that they are uncorrelated (since the acceptance, reconstruction, and trigger uncertainties do not apply to the $\mathcal{R}$ measurement, and the fit is different), while the statistical uncertainties are assumed to be correlated [49].

6.4.1 $\mathcal{R}$ Measurement

The $\mathcal{R}$ measurement is shown in Figure 6.5. The results agree well with CMS's [61] and CDF's [64] similar results, however the ATLAS measurement has a finer rapidity binning and an increased p_T range. ATLAS's and CDF's agreement indicates that $\mathcal{R}$ does not depend strongly on collision energy. $\mathcal{R}$ increases from about 10% at the lowest p_T bin from $1-4$ GeV to about 60% in highest p_T bin from $30-70$ GeV. This indicates that the non-prompt cross-section does not fall as rapidly as the prompt cross-section as a function of p_T. The shape does not depend strongly on the rapidity.

6.4.2 Non-prompt Cross-Section

The total integrated cross-section for non-prompt J/ψ meson is measured in the range of $|y| < 2.4$ and $p_T > 7$ GeV to be

$$\begin{aligned}\mathrm{Br}(J/\psi \to \mu\mu)\sigma(pp \to J/\psi X; |y| < 2.4, p_T > 7\mathrm{GeV}) \\ = 23.0 \pm 0.6(\mathrm{stat.}) \pm 2.8(\mathrm{syst.}) \pm 0.2(\mathrm{spin}) \pm 0.8(\mathrm{lumi.})\mathrm{nb},\end{aligned}$$

and for $1.5 \leq |y| < 2$ and $p_T > 1$ GeV, the cross-section is

$$\begin{aligned}\mathrm{Br}(J/\psi \to \mu\mu)\sigma(pp \to J/\psi X; 1.5 \leq |y| < 2, p_T > 1\mathrm{GeV}) \\ = 61 \pm 24(\mathrm{stat.}) \pm 19(\mathrm{syst.}) \pm 1(\mathrm{spin}) \pm 2(\mathrm{lumi.})\mathrm{nb}.\end{aligned}$$

The theoretical prediction of the non-prompt J/ψ cross-section was made using Fixed Order Next-to-Leading-Logarithm (FONLL) calculations [65, 66]. FONLL v1.3.2 was used with the CTEQ6.6 [67] parton density function set. Uncertainty bands for the prediction come from the input b-quark mass (varied within 4.75 ± 0.25 GeV), renormalization and factorization scales (independently varied within $0.5 < \mu_{R,F} < 2$ with the constraint that $0.5 < \frac{\mu_R}{\mu_F} < 2$), and the parton density function uncertainties. The comparison with data is shown in Figure 6.6. Good agreement is seen across the full range of rapidity and p_T [49], as was also seen by CDF [64].

6.4.3 Prompt Cross-Section

The total integrated cross-section for prompt J/ψ meson is measured in the range of $|y| < 2.4$ and $p_T > 7$ GeV to be

$$\begin{aligned}\mathrm{Br}(J/\psi \to \mu\mu)\sigma(pp \to J/\psi X; |y| < 2.4, p_T > 7\mathrm{GeV}) \\ = 59 \pm 1(\mathrm{stat.}) \pm 8(\mathrm{syst.})^{+9}_{-6}(\mathrm{spin}) \pm 2(\mathrm{lumi.})\mathrm{nb.},\end{aligned}$$

and for $1.5 \leq |y| < 2$ and $p_T > 1$ GeV, the cross-section is

$$\begin{aligned}\mathrm{Br}(J/\psi \to \mu\mu)\sigma(pp \to J/\psi X; 1.5 \leq |y| < 2, p_T > 1\mathrm{GeV}) \\ = 450 \pm 70(\mathrm{stat.})^{+90}_{-110}(\mathrm{syst.})^{+740}_{-110}(\mathrm{spin}) \pm 20(\mathrm{lumi.})\mathrm{nb}.\end{aligned}$$

The prompt J/ψ cross-section is compared to two theoretical models: the Color Evaporation Model (CEM) and the Color Singlet Model (CSM). The Color Octet Model (COM) prediction is not compared to data here, because new changes to the ATLAS Monte Carlo tune required a retuning of the Long-Distance-Matrix-Elements, which wasn't ready at the time of this writing.

The CEM prediction [68] was not calculated with any theoretical uncertainties: the charm quark mass is set to 1.2 GeV and the renormalization and factorization scales are set to $\mu_0 = 2\sqrt{p_T^2 + m_c^2 + k_T^2}$ (where p_T is the transverse momentum of the J/ψ, m_c is the charm quark mass, and k_T is a phenomenological parameter set to 1.5 GeV). The CEM prediction includes feed-down contributions from χ_c and $\psi(2S)$. The normalization of the CEM prediction is a little lower than the measured value, but the most prominant difference with data is in the shape of the curve over the measured p_T range [49].

The CSM prediction was calculated using NLO and a partial NNLO (NNLO*) perturbative QCD [69, 70]. The CSM prediction uses a charm quark mass of 1.5 GeV and the renormalization and factorization scales are set to $\mu_0 = \sqrt{p_T^2 + m_c^2}$. The theoretical uncertainties in the renormalization and factorization scales were calculated by varying the scales up and down by a factor of 2. Feed-down from χ_c and $\psi(2S)$ was taken into account, however, the feed-down correction factor is not well known under LHC conditions. A 10% correction was applied to account for the contribution from $\psi(2S) \to J/\psi\pi\pi$ and a 40% correction was applied to

account for radiative χ_c decays. The feed-down correction factors are assigned a 100% uncertainty, which is not included in the CSM theoretical uncertainty. The comparison of data with theory is shown in Figure 6.7. While the CSM prediction is much improved by including the NNLO* calculations, it still does not match the measured cross-section. The most prominent difference is the overall normalization of the CSM prediction, which is quite low, however, the cross-section increased by approximately an order of magnitude between NLO and NNLO*, so it is possible that adding more orders to the QCD perturbative calculations will remove the discrepancy with the experimental measurement [49].

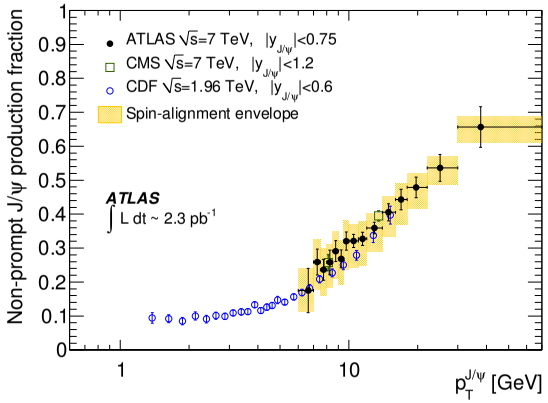

(a) $0 \leq |y| < 0.75$

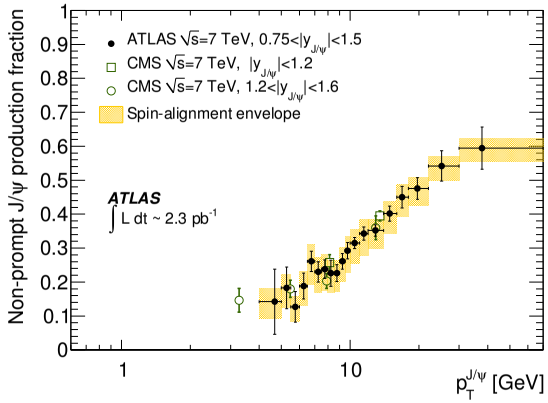

(b) $0.75 \leq |y| < 1.5$

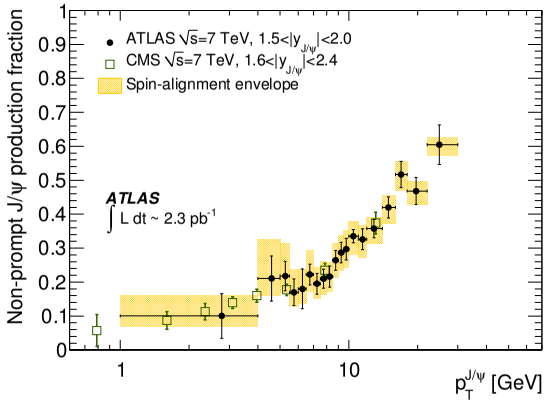

(c) $1.5 \leq |y| < 2$

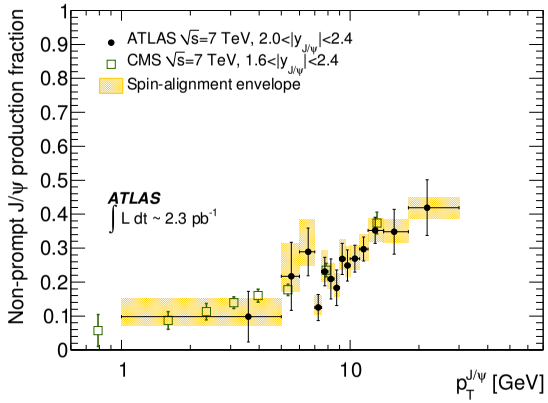

(d) $1.5 \leq |y| < 2.4$

Figure 6.5 $\mathcal{R}$ measurement for the ATLAS, CMS, and CDF [64] experiments. The overlaid yellow band is the spin-alignment systematic uncertainty for the ATLAS measurement [49].

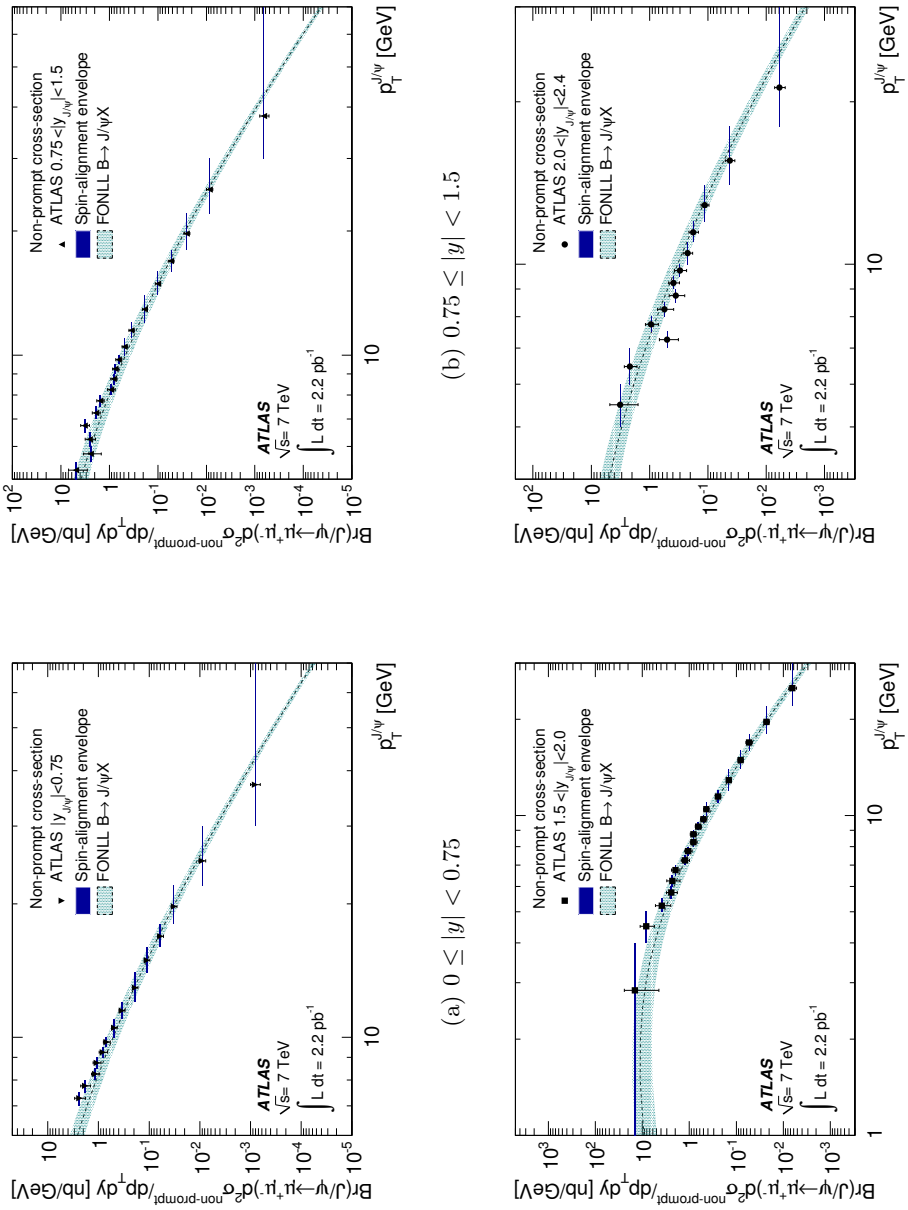

(a) $0 \leq |y| < 0.75$

(b) $0.75 \leq |y| < 1.5$

(c) $1.5 \leq |y| < 2$

(d) $1.5 \leq |y| < 2.4$

Figure 6.6 The non-prompt J/ψ cross-section compared to predictions from FONLL. The overlaid dark blue band is the spin-alignment uncertainty, and the overlaid blue band represents the theoretical uncertainty in the FONLL prediction. The luminosity uncertainty of 3.4% is not shown [49].

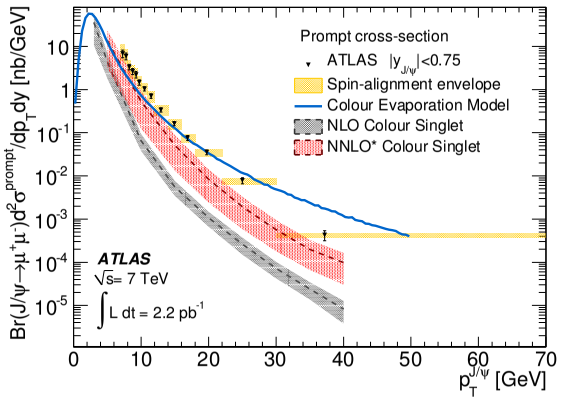

(a) $0 \leq |y| < 0.75$

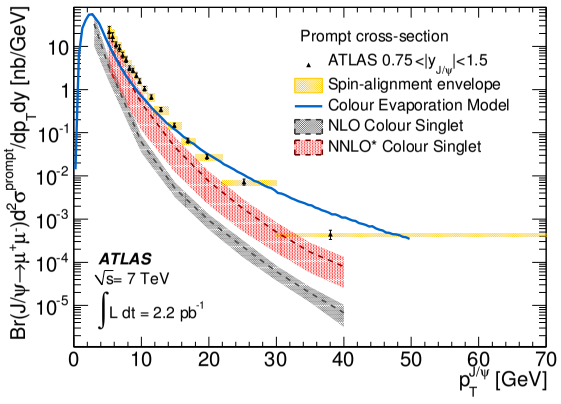

(b) $0.75 \leq |y| < 1.5$

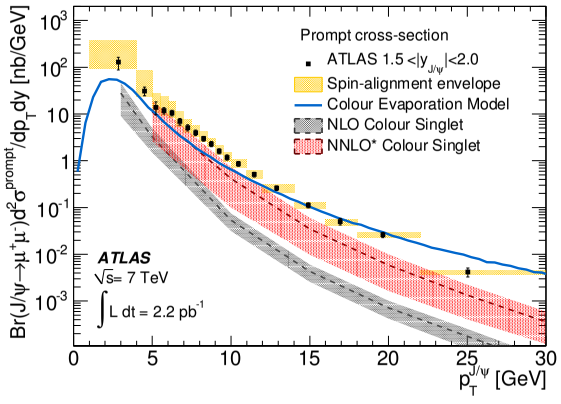

(c) $1.5 \leq |y| < 2$

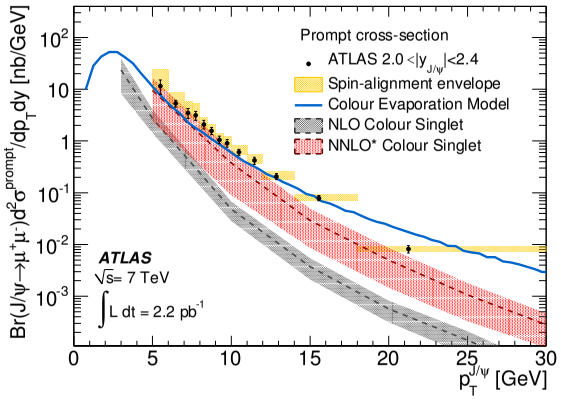

(d) $1.5 \leq |y| < 2.4$

Figure 6.7 The prompt J/ψ cross-section compared to predictions from NLO and NNLO* Color Singlet Model and Color Evaporation Model calculations. The overlaid yellow band is the spin-alignment uncertainty, while the overlaid red and gray bands represent the theoretical uncertainty. The luminosity uncertainty of 3.4% is not shown [49].

CHAPTER 7. Conclusion and Outlook

Two measurements have been presented in this thesis: the inclusive differential J/ψ cross-section with respect to p_T and rapidity and the ratio of the non-prompt to prompt J/ψ cross-sections with the ATLAS detector at $\sqrt{s} = 7$ TeV with an integrated luminosity of 2.3 pb^{-1}. These measurements were performed in the range $|y| < 2.4$ and $1 < p_T < 70$ GeV. The inclusive J/ψ cross-section measurement agrees well with the measurements performed at the same energy by CMS [61] and LHCb [71]. The non-prompt production fraction agrees well with the measurements at CMS [61] and CDF [64]. The CDF measurement was performed at a lower energy, indicating that the non-prompt production fraction does not depend strongly on the collision center-of-mass energy.

The J/ψ non-prompt cross-section shows impressive agreement with the theoretical prediction across the entire range that was measured while the J/ψ prompt cross-section was compared to different theoretical calculations and significant deviations were observed in both the shape and normalization. Although the non-prompt cross-section agrees very well with the theoretical predictions as described in Section 2.3.4, only the b-quark production is described perturbatively; the fragmentation of the b quark into different varieties of b hadrons is modeled by a fragmentation function derived from data. For the theoretical prediction of the prompt cross-section, the production of both valence quarks is modeled perturbatively. This is because b hadrons are composed of a b quark and other much lighter quarks (up, down, or strange), while the J/ψ meson is composed of two heavy quarks (relative to the QCD energy scale).

Measuring the prompt and non-prompt J/ψ cross-section provides an important input towards improving the theoretical description of J/ψ production in hadron colliders at never before explored center-of-mass energies and J/ψ transverse momentum. The systematic uncertainties in the cross-section measurement can be greatly reduced by measuring the production

polarization of the J/ψ meson. The polarization measurement itself will put a strong constraint on theoretical models, since the Color Octet Model predicts the J/ψ meson will be strongly transversely polarized at high p_T. A measurement of the J/ψ production polarization is currently being performed at ATLAS with an integrated luminosity of ≈ 100 pb^{-1}. The study will measure the angular correlation of the two muons from the J/ψ decay in the J/ψ rest frame, and determine the three polarization parameters in Equation 2.8.[1] The statistical uncertainty in the lower J/ψ p_T bins will not be much further reduced because as the instantaneous luminosity increases, the lower threshold muon trigger efficiencies will be sharply reduced due to prescaling of the low p_T triggers [73].

In addition to J/ψ production cross-section measurements, ATLAS has a rich quarkonia physics program. The recent $\Upsilon(1S)$ cross-section measurement is reported in a paper that was submitted for publication. The theoretical description of Υ production is very similar to J/ψ production; the main difference is the higher mass of the b quark. The experimental measurement placed higher cuts on the muon p_T since the Υ mesons have a higher mass than the J/ψ. This resulted in a higher offline reconstruction efficiency since it depends strongly on muon p_T. However, the background shape depended significantly on the di-muon p_T due to the different muon p_T cuts and the different mass of the Υ mesons. A similar discrepancy with the Color Singlet Model QCD NLO predictions was found. A comparison of data with NRQCD predictions showed differences in shape in the $\Upsilon(1S)$ p_T spectrum [72, 74].

Measuring χ_b and χ_c production can also constrain theoretical models of quarkonia. About $30-40\%$ of J/ψ decays are expected to come from feed-down decays $\chi_c \to J/\psi\gamma$. However, the energy of the radiated photon is expected to be quite low which makes the full reconstruction of the χ_c decay difficult. First studies are now underway to attempt to reconstruct $\chi_c \to J/\psi\gamma$. In the longer term future, χ_b production may be measured through the double J/ψ decay $\chi_b \to J/\psi J/\psi$. About 10 events per fb^{-1} are expected [73].

It is an exciting time for particle physics: in June 2011, the integrated luminosity recorded by the ATLAS detector reached the milestone of 1 fb^{-1} [75] and the LHC set a world record for

[1] Preliminary studies with generated Monte Carlo indicate that with 10 pb^{-1} the polarization parameters can be determined with a precision in the range of $0.02 - 0.06$, however, this study did not determine all the parameters in Equation 2.8 but instead integrated over the ϕ direction.

beam intensity at a hadron collider with an instantaneous luminosity of $4.67 \times 10^{32} \mathrm{cm}^{-2}\mathrm{s}^{-1}$ [76]. The LHC experiments are expected to collect more data until 2012 after which the LHC will undergo a long-term shutdown to upgrade the accelerator magnets to reach the design center-of-mass energy of 14 TeV [77]. Many studies are in progress, and will shed more light on the puzzle of J/ψ meson production.

APPENDIX A. Additional Material

This appendix contains supplementary material for some of the chapters.

J/ψ Cross-Section Measurement

Tables A.1 and A.2 show the carving cuts used in the cross-section analysis.

Table A.1 Offline muon reconstruction carving cuts.

Muon η Range	Muon p_T cut
$0.0 \leq \lvert\eta\rvert < 0.1$	$p_T > 4.0$
$0.1 \leq \lvert\eta\rvert < 0.7$	$p_T > 3.2$
$0.7 \leq \lvert\eta\rvert < 1.1$	$p_T > 2.6$
$1.1 \leq \lvert\eta\rvert < 1.3$	$p_T > 4.0$
$1.3 \leq \lvert\eta\rvert < 1.5$	$p_T > 2.0$
$1.5 \leq \lvert\eta\rvert < 2.0$	$p_T > 1.0$
$2.0 \leq \lvert\eta\rvert < 2.5$	$p_T > 2.0$

Table A.2 Trigger carving cuts.

Muon η Range	Muon p_T cut
$-2.5 \leq \eta < -2.0$	$p_T > 2.0$
$-2.0 \leq \eta < -1.5$	$p_T > 1.5$
$-1.5 \leq \eta < -1.3$	$p_T > 2.0$
$-1.3 \leq \eta < -1.1$	$p_T > 4.0$
$-1.1 \leq \eta < -0.7$	$p_T > 2.6$
$-0.7 \leq \eta < -0.1$	$p_T > 3.2$
$-0.1 \leq \eta < 0.1$	$p_T > 4.0$
$0.1 \leq \eta < 0.7$	$p_T > 3.2$
$0.7 \leq \eta < 1.1$	$p_T > 3.5$
$1.1 \leq \eta < 1.5$	$p_T > 4.0$
$1.5 \leq \eta < 2.0$	$p_T > 3.0$
$2.0 \leq \eta < 2.4$	$p_T > 4.0$
$2.4 \leq \eta < 2.5$	$p_T > \infty$

Table A.4 shows the bin boundaries used in the cross-section analysis.

Table A.3 Bins for the cross-section analysis.

J/ψ p_T	$\lvert J/\psi$ rapidity$\rvert$ $0 - 0.75$	$\lvert J/\psi$ rapidity$\rvert$ $0.75 - 1.50$	$\lvert J/\psi$ rapidity$\rvert$ $1.50 - 2.00$	$\lvert J/\psi$ rapidity$\rvert$ $2.00 - 2.40$
$40 - 70$ GeV	Used	Used	Not used	Not used
$30 - 40$ GeV	Used	Used	Used	Used
$22 - 30$ GeV	Used	Used	Used	Used
$18 - 22$ GeV	Used	Used	Used	Used
$16 - 18$ GeV	Used	Used	Used	Used
$14 - 16$ GeV	Used	Used	Used	Used
$12 - 14$ GeV	Used	Used	Used	Used
$11 - 12$ GeV	Used	Used	Used	Used
$10 - 11$ GeV	Used	Used	Used	Used
$9.5 - 10.$ GeV	Used	Used	Used	Used
$9.0 - 9.5$ GeV	Used	Used	Used	Used
$8.5 - 9.0$ GeV	Used	Used	Used	Used
$8.0 - 8.5$ GeV	Used	Used	Used	Used
$7.5 - 8.0$ GeV	Used	Used	Used	Used
$7.0 - 7.5$ GeV	Used	Used	Used	Used
$6.5 - 7.0$ GeV	Not used	Used	Used	Used
$6.0 - 6.5$ GeV		Used	Used	Used
$5.5 - 6.0$ GeV		Used	Used	Used
$5.0 - 5.5$ GeV		Used	Used	Used
$4.0 - 5.0$ GeV		Not used	Used	Not used
$1.0 - 4.0$ GeV			Used	

J/ψ $\mathcal{R}$ Measurement

Table A.4 shows the bin boundaries used in the $\mathcal{R}$ measurement.

Table A.4 Bins for the $\mathcal{R}$ analysis.

J/ψ p_T	$\lvert J/\psi$ rapidity$\rvert$ $0-0.75$	$\lvert J/\psi$ rapidity$\rvert$ $0.75-1.50$	$\lvert J/\psi$ rapidity$\rvert$ $1.50-2.00$	$\lvert J/\psi$ rapidity$\rvert$ $2.00-2.40$
$40-70$ GeV	Used	Used	Not used	Not used
$30-40$ GeV				
$22-30$ GeV	Used	Used	Used	Used
$18-22$ GeV	Used	Used	Used	
$16-18$ GeV	Used	Used	Used	Used
$14-16$ GeV	Used	Used	Used	
$12-14$ GeV	Used	Used	Used	Used
$11-12$ GeV	Used	Used	Used	Used
$10-11$ GeV	Used	Used	Used	Used
$9.5-10.$ GeV	Used	Used	Used	Used
$9.0-9.5$ GeV	Used	Used	Used	Used
$8.5-9.0$ GeV	Used	Used	Used	Used
$8.0-8.5$ GeV	Used	Used	Used	Used
$7.5-8.0$ GeV	Used	Used	Used	Used
$7.0-7.5$ GeV	Used	Used	Used	Used
$6.5-7.0$ GeV	Used	Used	Used	Used
$6.0-6.5$ GeV		Used	Used	
$5.5-6.0$ GeV	Not used	Used	Used	Used
$5.0-5.5$ GeV		Used	Used	
$4.0-5.0$ GeV		Used	Used	Used
$1.0-4.0$ GeV		Not used	Used	

APPENDIX B. Results

This appendix contains tables with the final inclusive cross-section, $\mathcal{R}$, non-prompt cross-section, and prompt cross-section measurements.

Inclusive J/ψ Cross-Section

Inclusive J/ψ production cross-sections as a function of J/ψ p_T within each rapidity slice. The first uncertainty is statistical, the second is systematic, and the third encapsulates any possible variation due to spin alignment from the unpolarized, isotropic central value [49].

Table B.1 Inclusive J/ψ production cross-sections as a function of J/ψ p_T within $|y| < 0.75$.

p_T (GeV)	$\langle p_T \rangle$ (GeV)	$\frac{d^2\sigma}{dp_T dy}\cdot\mathrm{Br}(J/\psi \to \mu^+\mu^-)$ [pb/GeV] $\lvert y\rvert < 0.75$ Value	± (stat.)	± (syst.)	± (spin)
40.0-70.0	46.6	0.462	±0.093	$\pm^{0.055}_{0.055}$	$\pm^{0.046}_{0.049}$
30.0-40.0	33.6	3.60	±0.48	$\pm^{0.38}_{0.39}$	$\pm^{0.43}_{0.52}$
22.0-30.0	25.0	16.9	±1.4	$\pm^{1.7}_{1.7}$	$\pm^{2.2}_{3.0}$
18.0-22.0	19.7	67.7	±3.6	$\pm^{6.4}_{6.3}$	$\pm^{10.9}_{14.5}$
16.0-18.0	16.9	136.2	±7.5	$\pm^{13.1}_{13.1}$	$\pm^{26.5}_{32.1}$
14.0-16.0	14.9	274	±12	$\pm^{27}_{27}$	$\pm^{60}_{70}$
12.0-14.0	12.9	528	±17	$\pm^{56}_{56}$	$\pm^{127}_{141}$
11.0-12.0	11.5	1051	±39	$\pm^{116}_{116}$	$\pm^{288}_{293}$
10.0-11.0	10.5	1528	±59	$\pm^{160}_{160}$	$\pm^{471}_{430}$
9.5-10.0	9.8	2170	±140	$\pm^{230}_{230}$	$\pm^{740}_{600}$
9.0-9.5	9.2	3040	±280	$\pm^{360}_{360}$	$\pm^{1240}_{840}$
8.5-9.0	8.8	3720	±270	$\pm^{450}_{440}$	$\pm^{1310}_{1150}$
8.0-8.5	8.3	4500	±320	$\pm^{510}_{530}$	$\pm^{1730}_{1410}$
7.5-8.0	7.8	7780	±720	$\pm^{1000}_{990}$	$\pm^{3540}_{2470}$
7.0-7.5	7.3	9220	±980	$\pm^{1140}_{1150}$	$\pm^{5770}_{2960}$

Table B.2 Inclusive J/ψ production cross-sections as a function of J/ψ p_T within $0.75 \leq |y| < 1.5$.

p_T (GeV)	$\langle p_T \rangle$ (GeV)	$\frac{d^2\sigma}{dp_T dy} \cdot \mathrm{Br}(J/\psi \to \mu^+\mu^-)$ [pb/GeV] $0.75 \leq \lvert y \rvert < 1.5$ Value	± (stat.)	± (syst.)	± (spin)
40.0-70.0	48.8	0.407	±0.084	$\pm^{0.041}_{0.043}$	$\pm^{0.022}_{0.017}$
30.0-40.0	33.9	3.16	±0.43	$\pm^{0.34}_{0.34}$	$\pm^{0.27}_{0.39}$
22.0-30.0	25.2	15.9	±1.1	$\pm^{1.8}_{1.6}$	$\pm^{1.7}_{2.4}$
18.0-22.0	19.7	53.3	±3.0	$\pm^{5.2}_{5.0}$	$\pm^{6.7}_{9.6}$
16.0-18.0	16.9	119.2	±6.7	$\pm^{11.9}_{11.7}$	$\pm^{17.0}_{23.1}$
14.0-16.0	14.9	249	±10	$\pm^{26}_{26}$	$\pm^{40}_{52}$
12.0-14.0	12.9	531	±16	$\pm^{60}_{58}$	$\pm^{94}_{118}$
11.0-12.0	11.5	1022	±35	$\pm^{121}_{120}$	$\pm^{187}_{234}$
10.0-11.0	10.5	1542	±51	$\pm^{176}_{174}$	$\pm^{283}_{348}$
9.5-10.0	9.7	2210	±100	$\pm^{250}_{240}$	$\pm^{420}_{490}$
9.0-9.5	9.3	2880	±140	$\pm^{330}_{320}$	$\pm^{610}_{640}$
8.5-9.0	8.7	3600	±200	$\pm^{390}_{390}$	$\pm^{1040}_{800}$
8.0-8.5	8.2	4080	±280	$\pm^{420}_{440}$	$\pm^{1870}_{900}$
7.5-8.0	7.7	6500	±400	$\pm^{860}_{810}$	$\pm^{1620}_{1770}$
7.0-7.5	7.2	8190	±610	$\pm^{1090}_{1040}$	$\pm^{2220}_{2300}$
6.5-7.0	6.7	12400	±1100	$\pm^{1700}_{1700}$	$\pm^{3900}_{3600}$
6.0-6.5	6.2	13500	±1100	$\pm^{1700}_{1700}$	$\pm^{7100}_{4000}$
5.5-6.0	5.8	19200	±2800	$\pm^{2700}_{2500}$	$\pm^{8600}_{5700}$
5.0-5.5	5.3	26800	±5600	$\pm^{4100}_{3800}$	$\pm^{10600}_{7900}$

Table B.3 Inclusive J/ψ production cross-sections as a function of J/ψ p_T within $1.5 \leq |y| < 2$.

p_T (GeV)	$\langle p_T \rangle$ (GeV)	$\frac{d^2\sigma}{dp_T dy} \cdot \mathrm{Br}(J/\psi \to \mu^+\mu^-)$ [pb/GeV] $1.5 \leq \lvert y \rvert < 2$ Value	± (stat.)	± (syst.)	± (spin)
30.0-40.0	34.1	2.22	±0.40	$\pm^{0.19}_{0.21}$	$\pm^{0.13}_{0.22}$
22.0-30.0	25.0	10.6	±1.1	$\pm^{1.0}_{0.9}$	$\pm^{0.8}_{1.2}$
18.0-22.0	19.6	48.9	±3.2	$\pm^{4.1}_{4.2}$	$\pm^{4.9}_{6.5}$
16.0-18.0	16.9	103.0	±6.9	$\pm^{13.0}_{9.4}$	$\pm^{12.0}_{15.5}$
14.0-16.0	14.9	193	±10	$\pm^{21}_{19}$	$\pm^{28}_{32}$
12.0-14.0	12.9	404	±15	$\pm^{45}_{43}$	$\pm^{74}_{75}$
11.0-12.0	11.5	754	±31	$\pm^{90}_{83}$	$\pm^{168}_{147}$
10.0-11.0	10.5	1297	±46	$\pm^{146}_{139}$	$\pm^{316}_{241}$
9.5-10.0	9.7	1674	±85	$\pm^{198}_{183}$	$\pm^{450}_{296}$
9.0-9.5	9.2	2260	±110	$\pm^{260}_{250}$	$\pm^{640}_{370}$
8.5-9.0	8.7	3110	±160	$\pm^{420}_{360}$	$\pm^{980}_{450}$
8.0-8.5	8.3	3790	±210	$\pm^{440}_{430}$	$\pm^{1490}_{450}$
7.5-8.0	7.7	5040	±350	$\pm^{590}_{520}$	$\pm^{2260}_{900}$
7.0-7.5	7.2	6350	±430	$\pm^{860}_{860}$	$\pm^{3130}_{1430}$
6.5-7.0	6.8	8910	±610	$\pm^{1270}_{1270}$	$\pm^{5420}_{1990}$
6.0-6.5	6.3	12760	±920	$\pm^{1840}_{1690}$	$\pm^{9970}_{2620}$
5.5-6.0	5.7	14300	±1200	$\pm^{1700}_{1700}$	$\pm^{14000}_{3100}$
5.0-5.5	5.2	17600	±3300	$\pm^{3000}_{2600}$	$\pm^{17300}_{4100}$
4.0-5.0	4.5	39400	±5500	$\pm^{5700}_{5700}$	$\pm^{69300}_{9700}$
1.0-4.0	2.8	143000	±23000	$\pm^{25000}_{39000}$	$\pm^{274000}_{39000}$

Table B.4 Inclusive J/ψ production cross-sections as a function of J/ψ p_T within $2 \leq |y| < 2.4$.

p_T (GeV)	$\langle p_T \rangle$ (GeV)	$\frac{d^2\sigma}{dp_T dy} \cdot \mathrm{Br}(J/\psi \to \mu^+\mu^-)$ [pb/GeV] $2 \leq \lvert y \rvert < 2.4$ Value	± (stat.)	± (syst.)	± (spin)
30.0-40.0	33.6	1.12	±0.43	$\pm^{0.10}_{0.28}$	$\pm^{0.06}_{0.10}$
22.0-30.0	24.9	6.2	±1.1	$\pm^{0.6}_{0.6}$	$\pm^{0.6}_{0.7}$
18.0-22.0	19.7	29.9	±3.3	$\pm^{3.1}_{3.4}$	$\pm^{3.7}_{3.8}$
16.0-18.0	16.9	77.8	±8.2	$\pm^{9.4}_{8.0}$	$\pm^{14.1}_{9.9}$
14.0-16.0	14.9	164	±12	$\pm^{26}_{16}$	$\pm^{33}_{21}$
12.0-14.0	12.9	320	±19	$\pm^{38}_{36}$	$\pm^{79}_{40}$
11.0-12.0	11.5	598	±43	$\pm^{69}_{73}$	$\pm^{174}_{71}$
10.0-11.0	10.5	829	±51	$\pm^{96}_{92}$	$\pm^{286}_{87}$
9.5-10.0	9.7	1208	±94	$\pm^{155}_{138}$	$\pm^{440}_{166}$
9.0-9.5	9.2	1450	±130	$\pm^{210}_{180}$	$\pm^{480}_{210}$
8.5-9.0	8.7	1930	±160	$\pm^{260}_{260}$	$\pm^{620}_{350}$
8.0-8.5	8.3	2650	±290	$\pm^{460}_{390}$	$\pm^{910}_{570}$
7.5-8.0	7.7	4070	±450	$\pm^{570}_{580}$	$\pm^{2920}_{650}$
7.0-7.5	7.3	3990	±500	$\pm^{560}_{550}$	$\pm^{2630}_{690}$
6.5-7.0	6.8	6290	±700	$\pm^{830}_{980}$	$\pm^{5140}_{1360}$
6.0-6.5	6.3	8800	±1100	$\pm^{1300}_{1200}$	$\pm^{7900}_{2200}$
5.5-6.0	5.8	13500	±3600	$\pm^{1900}_{2200}$	$\pm^{11400}_{2700}$
5.0-5.5	5.3	15900	±4300	$\pm^{2800}_{2600}$	$\pm^{28800}_{4300}$

$\mathcal{R}$ Measurement

Non-prompt to inclusive production cross-section fraction $\mathcal{R}$ as a function of J/ψ p_T for each rapidity slice under the assumption that prompt and non-prompt J/ψ production is isotropically polarized. The spin alignment envelope spans the range of possible prompt cross-sections under various polarisation hypotheses, plus the range of non-prompt cross-sections within $\lambda_\theta = \pm 0.1$. The first uncertainty is statistical, the second uncertainty is systematic, and the third is the uncertainty due to spin alignment [49].

Table B.5 Non-prompt to inclusive production cross-section fraction $\mathcal{R}$ as a function of J/ψ p_T for $|y| < 0.75$.

p_T (GeV)	$\langle p_T \rangle$ (GeV)	Non-prompt to inclusive production fraction $\lvert y\rvert < 0.75$			
		$\mathcal{R}$	± (stat.)	± (syst.)	± (spin)
30.0-70.0	37.7	0.656	±0.059	±0.008	$\pm^{0.030}_{0.045}$
22.0-30.0	25.0	0.536	±0.039	±0.008	$\pm^{0.032}_{0.050}$
18.0-22.0	19.7	0.479	±0.030	±0.004	$\pm^{0.040}_{0.063}$
16.0-18.0	16.9	0.443	±0.030	±0.005	$\pm^{0.048}_{0.073}$
14.0-16.0	14.9	0.405	±0.024	±0.008	$\pm^{0.046}_{0.072}$
12.0-14.0	12.9	0.359	±0.017	±0.003	$\pm^{0.044}_{0.069}$
11.0-12.0	11.5	0.327	±0.019	±0.003	$\pm^{0.051}_{0.078}$
10.0-11.0	10.5	0.321	±0.018	±0.007	$\pm^{0.050}_{0.077}$
9.5-10.0	9.8	0.320	±0.026	±0.006	$\pm^{0.062}_{0.083}$
9.0-9.5	9.2	0.268	±0.025	±0.008	$\pm^{0.054}_{0.076}$
8.5-9.0	8.8	0.291	±0.030	±0.005	$\pm^{0.058}_{0.079}$
8.0-8.5	8.3	0.258	±0.032	±0.017	$\pm^{0.054}_{0.074}$
7.5-8.0	7.8	0.236	±0.030	±0.007	$\pm^{0.061}_{0.076}$
7.0-7.5	7.3	0.259	±0.038	±0.002	$\pm^{0.066}_{0.080}$
6.0-7.0	6.6	0.175	±0.057	±0.032	$\pm^{0.064}_{0.062}$

Table B.6 Non-prompt to inclusive production cross-section fraction $\mathcal{R}$ as a function of J/ψ p_T for $0.75 \leq |y| < 1.50$.

p_T (GeV)	$\langle p_T \rangle$ (GeV)	Non-prompt to inclusive production fraction $0.75 \leq \lvert y \rvert < 1.50$ $\mathcal{R}$	± (stat.)	± (syst.)	± (spin)
30.0-70.0	37.8	0.594	±0.060	±0.016	$\pm^{0.029}_{0.040}$
22.0-30.0	25.1	0.542	±0.042	±0.015	$\pm^{0.029}_{0.042}$
18.0-22.0	19.7	0.476	±0.031	±0.006	$\pm^{0.033}_{0.052}$
16.0-18.0	16.9	0.450	±0.031	±0.006	$\pm^{0.036}_{0.058}$
14.0-16.0	14.9	0.401	±0.022	±0.003	$\pm^{0.035}_{0.058}$
12.0-14.0	12.9	0.352	±0.016	±0.005	$\pm^{0.033}_{0.054}$
11.0-12.0	11.5	0.343	±0.018	±0.007	$\pm^{0.041}_{0.064}$
10.0-11.0	10.5	0.315	±0.016	±0.004	$\pm^{0.040}_{0.061}$
9.5-10.0	9.8	0.292	±0.023	±0.008	$\pm^{0.043}_{0.064}$
9.0-9.5	9.2	0.261	±0.021	±0.009	$\pm^{0.040}_{0.060}$
8.5-9.0	8.8	0.226	±0.021	±0.013	$\pm^{0.036}_{0.055}$
8.0-8.5	8.2	0.226	±0.022	±0.032	$\pm^{0.036}_{0.055}$
7.5-8.0	7.8	0.238	±0.023	±0.015	$\pm^{0.043}_{0.062}$
7.0-7.5	7.2	0.230	±0.025	±0.017	$\pm^{0.041}_{0.061}$
6.5-7.0	6.8	0.261	±0.029	±0.007	$\pm^{0.051}_{0.069}$
6.0-6.5	6.3	0.188	±0.033	±0.019	$\pm^{0.042}_{0.057}$
5.5-6.0	5.8	0.127	±0.038	±0.024	$\pm^{0.030}_{0.043}$
5.0-5.5	5.3	0.183	±0.049	±0.036	$\pm^{0.039}_{0.058}$
4.0-5.0	4.7	0.142	±0.094	±0.018	$\pm^{0.039}_{0.049}$

Table B.7 Non-prompt to inclusive production cross-section fraction $\mathcal{R}$ as a function of J/ψ p_T for $1.5 \leq |y| < 2$.

p_T (GeV)	$\langle p_T \rangle$ (GeV)	Non-prompt to inclusive production fraction $1.5 \leq \lvert y \rvert < 2$ $\mathcal{R}$	± (stat.)	± (syst.)	± (spin)
22.0-30.0	24.9	0.605	±0.058	±0.005	$\pm^{0.021}_{0.032}$
18.0-22.0	19.7	0.468	±0.038	±0.012	$\pm^{0.029}_{0.041}$
16.0-18.0	16.9	0.517	±0.038	±0.007	$\pm^{0.039}_{0.048}$
14.0-16.0	14.9	0.420	±0.029	±0.011	$\pm^{0.035}_{0.047}$
12.0-14.0	12.9	0.357	±0.022	±0.015	$\pm^{0.034}_{0.045}$
11.0-12.0	11.5	0.326	±0.026	±0.017	$\pm^{0.042}_{0.054}$
10.0-11.0	10.5	0.335	±0.019	±0.004	$\pm^{0.043}_{0.055}$
9.5-10.0	9.7	0.297	±0.028	±0.015	$\pm^{0.053}_{0.053}$
9.0-9.5	9.2	0.287	±0.026	±0.015	$\pm^{0.051}_{0.052}$
8.5-9.0	8.8	0.264	±0.023	±0.018	$\pm^{0.049}_{0.050}$
8.0-8.5	8.2	0.216	±0.022	±0.022	$\pm^{0.042}_{0.044}$
7.5-8.0	7.8	0.210	±0.024	±0.014	$\pm^{0.052}_{0.047}$
7.0-7.5	7.3	0.195	±0.025	±0.017	$\pm^{0.049}_{0.044}$
6.5-7.0	6.8	0.222	±0.028	±0.013	$\pm^{0.069}_{0.048}$
6.0-6.5	6.3	0.180	±0.034	±0.048	$\pm^{0.057}_{0.042}$
5.5-6.0	5.8	0.170	±0.034	±0.019	$\pm^{0.068}_{0.041}$
5.0-5.5	5.3	0.218	±0.043	±0.006	$\pm^{0.097}_{0.050}$
4.0-5.0	4.6	0.210	±0.042	±0.051	$\pm^{0.115}_{0.051}$
1.0-4.0	2.8	0.100	±0.053	±0.039	$\pm^{0.061}_{0.031}$

Table B.8 Non-prompt to inclusive production cross-section fraction $\mathcal{R}$ as a function of J/ψ p_T for $2 \leq |y| < 2.4$.

p_T (GeV)	$\langle p_T \rangle$ (GeV)	Non-prompt to inclusive production fraction $2 \leq \lvert y \rvert < 2.4$ $\mathcal{R}$	± (stat.)	± (syst.)	± (spin)
18.0-30.0	21.7	0.419	±0.058	±0.058	$\pm^{0.032}_{0.031}$
14.0-18.0	15.6	0.348	±0.044	±0.049	$\pm^{0.038}_{0.032}$
12.0-14.0	12.9	0.352	±0.034	±0.018	$\pm^{0.037}_{0.033}$
11.0-12.0	11.5	0.297	±0.034	±0.010	$\pm^{0.045}_{0.034}$
10.0-11.0	10.5	0.269	±0.037	±0.014	$\pm^{0.040}_{0.033}$
9.5-10.0	9.7	0.249	±0.045	±0.008	$\pm^{0.055}_{0.032}$
9.0-9.5	9.2	0.268	±0.037	±0.027	$\pm^{0.057}_{0.033}$
8.5-9.0	8.7	0.183	±0.041	±0.032	$\pm^{0.042}_{0.024}$
8.0-8.5	8.2	0.209	±0.042	±0.042	$\pm^{0.046}_{0.028}$
7.5-8.0	7.8	0.231	±0.037	±0.020	$\pm^{0.063}_{0.031}$
7.0-7.5	7.2	0.125	±0.035	±0.016	$\pm^{0.037}_{0.019}$
6.0-7.0	6.6	0.289	±0.047	±0.052	$\pm^{0.096}_{0.041}$
5.0-6.0	5.5	0.217	±0.077	±0.065	$\pm^{0.096}_{0.044}$
1.0-5.0	3.6	0.098	±0.065	±0.036	$\pm^{0.053}_{0.027}$

Non-prompt Cross-Section

Non-prompt J/ψ production cross-sections as a function of J/ψ p_T for each rapidity slice under the assumption that prompt and non-prompt J/ψ production is unpolarised, and the spin alignment envelope spans the range of non-prompt cross-sections within $\lambda_\theta = \pm 0.1$. The first uncertainty is statistical, the second uncertainty is systematic, and the third is the spin alignment [49].

Table B.9 Non-prompt J/ψ production cross-sections as a function of J/ψ p_T for $|y| < 0.75$.

p_T (GeV)	$\langle p_T \rangle$ (GeV)	$\frac{d^2\sigma^{non-prompt}}{dp_T dy} \cdot \mathrm{Br}(J/\psi \to \mu^+\mu^-)$ [nb/GeV] $\|y\| < 0.75$ Value	± (stat.)	± (syst.)	± (spin)
30.0-70.0	37.2	0.0008	±0.0001	±0.0001	±0.0000
22.0-30.0	25.0	0.0091	±0.0010	±0.0011	±0.0002
18.0-22.0	19.7	0.032	±0.003	±0.003	±0.001
16.0-18.0	16.9	0.060	±0.005	±0.006	±0.002
14.0-16.0	14.9	0.111	±0.008	±0.011	±0.003
12.0-14.0	12.9	0.19	±0.01	±0.02	±0.004
11.0-12.0	11.5	0.34	±0.02	±0.04	±0.01
10.0-11.0	10.5	0.49	±0.03	±0.05	±0.01
9.5-10.0	9.8	0.69	±0.07	±0.08	±0.02
9.0-9.5	9.3	0.8	±0.1	±0.1	±0.02
8.5-9.0	8.8	1.1	±0.1	±0.1	±0.03
8.0-8.5	8.3	1.2	±0.2	±0.1	±0.03
7.5-8.0	7.8	1.8	±0.3	±0.3	±0.06
7.0-7.5	7.3	2.4	±0.4	±0.4	±0.08

Table B.10 Non-prompt J/ψ production cross-sections as a function of J/ψ p_T for $0.75 \leq |y| < 1.5$.

p_T (GeV)	$\langle p_T \rangle$ (GeV)	$\frac{d^2\sigma^{non-prompt}}{dp_T dy} \cdot \mathrm{Br}(J/\psi \to \mu^+\mu^-)$ [nb/GeV] $0.75 \leq \lvert y \rvert < 1.5$ Value	± (stat.)	± (syst.)	± (spin)
30.0-70.0	38.0	0.0007	±0.0001	±0.0001	±0.0000
22.0-30.0	25.2	0.0086	±0.0009	±0.0010	±0.0001
18.0-22.0	19.7	0.025	±0.002	±0.003	±0.001
16.0-18.0	16.9	0.054	±0.005	±0.006	±0.001
14.0-16.0	14.9	0.100	±0.007	±0.011	±0.002
12.0-14.0	12.9	0.19	±0.01	±0.02	±0.00
11.0-12.0	11.5	0.35	±0.02	±0.04	±0.01
10.0-11.0	10.5	0.49	±0.03	±0.05	±0.01
9.5-10.0	9.8	0.65	±0.06	±0.07	±0.02
9.0-9.5	9.3	0.75	±0.07	±0.08	±0.02
8.5-9.0	8.8	0.81	±0.09	±0.09	±0.02
8.0-8.5	8.3	0.9	±0.1	±0.1	±0.02
7.5-8.0	7.8	1.6	±0.2	±0.2	±0.04
7.0-7.5	7.2	1.9	±0.3	±0.3	±0.05
6.5-7.0	6.8	3.3	±0.5	±0.5	±0.09
6.0-6.5	6.3	2.5	±0.5	±0.4	±0.07
5.5-6.0	5.8	2.4	±0.8	±0.5	±0.07
5.0-5.5	5.3	4.9	±1.7	±1.2	±0.15

Table B.11 Non-prompt J/ψ production cross-sections as a function of J/ψ p_T for $1.5 \leq |y| < 2$.

p_T (GeV)	$\langle p_T \rangle$ (GeV)	$\frac{d^2\sigma^{non-prompt}}{dp_T dy} \cdot \mathrm{Br}(J/\psi \to \mu^+\mu^-)$ [nb/GeV] $1.5 \leq \lvert y \rvert < 2$ Value	± (stat.)	± (syst.)	± (spin)
22.0-30.0	25.0	0.0064	±0.0009	±0.00081	±0.0001
18.0-22.0	19.6	0.023	±0.002	±0.002	±0.0000
16.0-18.0	16.9	0.053	±0.005	±0.007	±0.001
14.0-16.0	14.9	0.081	±0.007	±0.009	±0.001
12.0-14.0	12.9	0.14	±0.01	±0.01	±0.002
11.0-12.0	11.5	0.25	±0.02	±0.03	±0.01
10.0-11.0	10.5	0.43	±0.03	±0.05	±0.01
9.5-10.0	9.8	0.50	±0.05	±0.05	±0.01
9.0-9.5	9.3	0.65	±0.07	±0.07	±0.01
8.5-9.0	8.8	0.82	±0.08	±0.10	±0.02
8.0-8.5	8.3	0.82	±0.10	±0.10	±0.02
7.5-8.0	7.8	1.1	±0.1	±0.1	±0.02
7.0-7.5	7.3	1.2	±0.2	±0.2	±0.03
6.5-7.0	6.8	2.0	±0.3	±0.3	±0.05
6.0-6.5	6.3	2.3	±0.5	±0.6	±0.05
5.5-6.0	5.7	2.4	±0.5	±0.4	±0.06
5.0-5.5	5.2	3.8	±1.0	±0.9	±0.09
4.0-5.0	4.5	8.3	±2.0	±1.9	±0.21
1.0-4.0	2.8	14.3	±7.9	±5.5	±0.37

Table B.12 Non-prompt J/ψ production cross-sections as a function of J/ψ p_T for $2 \leq |y| < 2.4$.

p_T (GeV)	$\langle p_T \rangle$ (GeV)	$\frac{d^2\sigma^{non-prompt}}{dp_T dy} \cdot \mathrm{Br}(J/\psi \to \mu^+\mu^-)$ [nb/GeV] $2 \leq \lvert y \rvert < 2.4$ Value	± (stat.)	± (syst.)	± (spin)
18.0-30.0	21.3	0.0059	±0.0010	±0.0007	±0.0001
14.0-18.0	15.6	0.042	±0.006	±0.005	±0.0004
12.0-14.0	12.9	0.11	±0.01	±0.01	±0.002
11.0-12.0	11.5	0.18	±0.02	±0.02	±0.003
10.0-11.0	10.5	0.22	±0.03	±0.03	±0.003
9.5-10.0	9.7	0.30	±0.06	±0.04	±0.005
9.0-9.5	9.2	0.39	±0.06	±0.06	±0.01
8.5-9.0	8.8	0.35	±0.09	±0.06	±0.01
8.0-8.5	8.3	0.6	±0.1	±0.1	±0.01
7.5-8.0	7.8	0.9	±0.2	±0.2	±0.01
7.0-7.5	7.3	0.5	±0.2	±0.1	±0.01
6.0-7.0	6.5	2.2	±0.4	±0.4	±0.02
5.0-6.0	5.5	3.2	±1.3	±1.0	±0.04

Prompt Cross-Section

Prompt J/ψ production cross-sections as a function of J/ψ p_T for each rapidity slice. The central value assumes unpolarised prompt and non-prompt production, and the spin alignment envelope spans the range of possible prompt cross-sections under various polarisation hypotheses. The first quoted uncertainty is statistical, the second uncertainty is systematic, and the third is spin alignment uncertainty [49].

Table B.13 Prompt J/ψ production cross-sections as a function of J/ψ p_T for $|y| < 0.75$.

p_T (GeV)	$\langle p_T \rangle$ (GeV)	$\frac{d^2\sigma^{prompt}}{dp_T\,dy}\cdot\mathrm{Br}(J/\psi \to \mu^+\mu^-)$ [nb/GeV] $\|y\| < 0.75$ Value	± (stat.)	± (syst.)	± (spin)
30.0-70.0	37.2	0.0004	±0.0001	$\pm^{0.0001}_{0.0001}$	$\pm^{0.0000}_{0.0000}$
22.0-30.0	25.0	0.0078	±0.0009	$\pm^{0.0009}_{0.0009}$	$\pm^{0.0010}_{0.0014}$
18.0-22.0	19.7	0.035	±0.003	$\pm^{0.004}_{0.004}$	$\pm^{0.006}_{0.008}$
16.0-18.0	16.9	0.076	±0.006	$\pm^{0.008}_{0.008}$	$\pm^{0.015}_{0.018}$
14.0-16.0	14.9	0.163	±0.010	$\pm^{0.016}_{0.016}$	$\pm^{0.036}_{0.042}$
12.0-14.0	12.9	0.34	±0.01	$\pm^{0.04}_{0.04}$	$\pm^{0.08}_{0.09}$
11.0-12.0	11.5	0.71	±0.03	$\pm^{0.08}_{0.08}$	$\pm^{0.19}_{0.20}$
10.0-11.0	10.5	1.04	±0.05	$\pm^{0.11}_{0.11}$	$\pm^{0.32}_{0.29}$
9.5-10.0	9.8	1.5	±0.1	$\pm^{0.2}_{0.2}$	$\pm^{0.5}_{0.4}$
9.0-9.5	9.2	2.2	±0.2	$\pm^{0.3}_{0.3}$	$\pm^{0.9}_{0.6}$
8.5-9.0	8.8	2.6	±0.2	$\pm^{0.4}_{0.4}$	$\pm^{0.9}_{0.8}$
8.0-8.5	8.3	3.3	±0.3	$\pm^{0.4}_{0.4}$	$\pm^{1.3}_{1.0}$
7.5-8.0	7.8	5.9	±0.6	$\pm^{0.9}_{0.9}$	$\pm^{2.7}_{1.9}$
7.0-7.5	7.3	6.8	±0.8	$\pm^{1.1}_{1.1}$	$\pm^{4.3}_{2.2}$

Cross-section for different J/ψ polarizations

The following four tables show the ratio of the inclusive J/ψ cross-section of the four different systematic polarization variations with the isotropic polarization assumption used for the nominal cross-section. More details on the polarization variations can be found in Section 5.7.1.

Table B.14 Prompt J/ψ production cross-sections as a function of J/ψ p_T for $0.75 \leq |y| < 1.5$.

p_T (GeV)	$\langle p_T \rangle$ (GeV)	$\frac{d^2\sigma^{prompt}}{dp_T dy} \cdot \mathrm{Br}(J/\psi \to \mu^+\mu^-)$ [nb/GeV] $0.75 \leq \lvert y \rvert < 1.5$ Value	± (stat.)	± (syst.)	± (spin)
30.0-70.0	38.0	0.0004	±0.0001	$\pm^{0.0001}_{0.0001}$	$\pm^{0.0000}_{0.0000}$
22.0-30.0	25.2	0.0073	±0.0008	$\pm^{0.0008}_{0.0008}$	$\pm^{0.0008}_{0.0011}$
18.0-22.0	19.7	0.028	±0.002	$\pm^{0.003}_{0.003}$	$\pm^{0.004}_{0.005}$
16.0-18.0	16.9	0.066	±0.005	$\pm^{0.007}_{0.007}$	$\pm^{0.009}_{0.013}$
14.0-16.0	14.9	0.149	±0.008	$\pm^{0.016}_{0.016}$	$\pm^{0.024}_{0.031}$
12.0-14.0	12.9	0.34	±0.01	$\pm^{0.04}_{0.04}$	$\pm^{0.06}_{0.08}$
11.0-12.0	11.5	0.67	±0.03	$\pm^{0.08}_{0.08}$	$\pm^{0.12}_{0.15}$
10.0-11.0	10.5	1.06	±0.04	$\pm^{0.12}_{0.12}$	$\pm^{0.19}_{0.24}$
9.5-10.0	9.7	1.57	±0.09	$\pm^{0.17}_{0.17}$	$\pm^{0.30}_{0.35}$
9.0-9.5	9.3	2.1	±0.1	$\pm^{0.2}_{0.2}$	$\pm^{0.5}_{0.5}$
8.5-9.0	8.7	2.8	±0.2	$\pm^{0.3}_{0.3}$	$\pm^{0.8}_{0.6}$
8.0-8.5	8.2	3.2	±0.2	$\pm^{0.3}_{0.3}$	$\pm^{1.4}_{0.7}$
7.5-8.0	7.7	5.0	±0.3	$\pm^{0.6}_{0.6}$	$\pm^{1.2}_{1.4}$
7.0-7.5	7.2	6.3	±0.5	$\pm^{0.8}_{0.8}$	$\pm^{1.7}_{1.8}$
6.5-7.0	6.7	9.2	±0.9	$\pm^{1.4}_{1.4}$	$\pm^{2.9}_{2.6}$
6.0-6.5	6.2	11.0	±1.0	$\pm^{1.4}_{1.4}$	$\pm^{5.8}_{3.2}$
5.5-6.0	5.8	16.8	±2.6	$\pm^{3.0}_{2.9}$	$\pm^{7.5}_{5.0}$
5.0-5.5	5.3	21.9	±4.7	$\pm^{4.8}_{4.6}$	$\pm^{8.7}_{6.5}$

Table B.15 Prompt J/ψ production cross-sections as a function of J/ψ p_T for $1.5 \leq |y| < 2$.

p_T (GeV)	$\langle p_T \rangle$ (GeV)	$\frac{d^2\sigma^{prompt}}{dp_T dy} \cdot \mathrm{Br}(J/\psi \to \mu^+\mu^-)$ [nb/GeV] $1.5 \leq \lvert y \rvert < 2$ Value	± (stat.)	± (syst.)	± (spin)
22.0-30.0	25.0	0.0042	±0.0007	$\pm^{0.0005}_{0.0005}$	$\pm^{0.0003}_{0.0005}$
18.0-22.0	19.6	0.026	±0.003	$\pm^{0.002}_{0.002}$	$\pm^{0.003}_{0.004}$
16.0-18.0	16.9	0.050	±0.005	$\pm^{0.007}_{0.005}$	$\pm^{0.006}_{0.008}$
14.0-16.0	14.9	0.112	±0.008	$\pm^{0.012}_{0.011}$	$\pm^{0.016}_{0.019}$
12.0-14.0	12.9	0.26	±0.01	$\pm^{0.03}_{0.02}$	$\pm^{0.05}_{0.04}$
11.0-12.0	11.5	0.51	±0.03	$\pm^{0.05}_{0.05}$	$\pm^{0.11}_{0.10}$
10.0-11.0	10.5	0.86	±0.04	$\pm^{0.10}_{0.09}$	$\pm^{0.21}_{0.16}$
9.5-10.0	9.7	1.18	±0.08	$\pm^{0.13}_{0.12}$	$\pm^{0.32}_{0.21}$
9.0-9.5	9.2	1.61	±0.09	$\pm^{0.17}_{0.17}$	$\pm^{0.46}_{0.26}$
8.5-9.0	8.7	2.3	±0.1	$\pm^{0.3}_{0.2}$	$\pm^{0.7}_{0.3}$
8.0-8.5	8.3	3.0	±0.2	$\pm^{0.3}_{0.3}$	$\pm^{1.2}_{0.4}$
7.5-8.0	7.7	4.0	±0.3	$\pm^{0.5}_{0.4}$	$\pm^{1.8}_{0.7}$
7.0-7.5	7.2	5.1	±0.4	$\pm^{0.7}_{0.7}$	$\pm^{2.5}_{1.2}$
6.5-7.0	6.8	6.9	±0.5	$\pm^{1.0}_{1.0}$	$\pm^{4.2}_{1.6}$
6.0-6.5	6.3	10.5	±0.9	$\pm^{1.2}_{1.1}$	$\pm^{8.2}_{2.2}$
5.5-6.0	5.7	11.8	±1.1	$\pm^{1.5}_{1.5}$	$\pm^{11.6}_{2.6}$
5.0-5.5	5.2	13.8	±2.7	$\pm^{3.4}_{3.2}$	$\pm^{13.5}_{3.2}$
4.0-5.0	4.5	31.1	±4.6	$\pm^{4.5}_{4.5}$	$\pm^{54.7}_{7.7}$
1.0-4.0	2.8	129	±22	$\pm^{25}_{35}$	$\pm^{246}_{35}$

Table B.16 Prompt J/ψ production cross-sections as a function of J/ψ p_T for $2 \leq |y| < 2.4$.

p_T (GeV)	$\langle p_T \rangle$ (GeV)	$\frac{d^2\sigma^{prompt}}{dp_T\,dy} \cdot \mathrm{Br}(J/\psi \to \mu^+\mu^-)$ [nb/GeV] $2 \leq \lvert y \rvert < 2.4$ Value	± (stat.)	± (syst.)	± (spin)
18.0-30.0	21.2	0.008	±0.001	$\pm^{0.001}_{0.001}$	$\pm^{0.001}_{0.001}$
14.0-18.0	15.6	0.079	±0.007	$\pm^{0.007}_{0.005}$	$\pm^{0.012}_{0.007}$
12.0-14.0	12.9	0.21	±0.02	$\pm^{0.02}_{0.02}$	$\pm^{0.05}_{0.03}$
11.0-12.0	11.5	0.42	±0.04	$\pm^{0.05}_{0.06}$	$\pm^{0.12}_{0.05}$
10.0-11.0	10.5	0.61	±0.05	$\pm^{0.07}_{0.07}$	$\pm^{0.21}_{0.06}$
9.5-10.0	9.7	0.91	±0.09	$\pm^{0.13}_{0.12}$	$\pm^{0.33}_{0.12}$
9.0-9.5	9.2	1.1	±0.1	$\pm^{0.1}_{0.1}$	$\pm^{0.3}_{0.2}$
8.5-9.0	8.7	1.6	±0.2	$\pm^{0.2}_{0.2}$	$\pm^{0.5}_{0.3}$
8.0-8.5	8.3	2.1	±0.3	$\pm^{0.3}_{0.3}$	$\pm^{0.7}_{0.5}$
7.5-8.0	7.7	3.1	±0.4	$\pm^{0.5}_{0.4}$	$\pm^{2.2}_{0.5}$
7.0-7.5	7.3	3.5	±0.5	$\pm^{0.6}_{0.5}$	$\pm^{2.3}_{0.6}$
6.0-7.0	6.5	5.6	±0.6	$\pm^{0.6}_{0.6}$	$\pm^{3.3}_{0.9}$
5.0-6.0	5.5	11.5	±2.5	$\pm^{2.5}_{2.6}$	$\pm^{12.1}_{2.0}$

Table B.17 Ratio of the longitudinally polarized ($\lambda_\theta = -1, \lambda_\phi = \lambda_{\theta\phi} = 0$) J/ψ cross-section the isotropically polarized J/ψ cross-section.

	J/ψ rapidity $0 - 0.75$	J/ψ rapidity $0.75 - 1.50$	J/ψ rapidity $1.50 - 2.00$	J/ψ rapidity $2.00 - 2.40$
40. – 70. GeV	0.89	0.96	0.88	0.98
30. – 40. GeV	0.86	0.88	0.90	0.91
22. – 30. GeV	0.82	0.85	0.89	0.89
18. – 22. GeV	0.79	0.82	0.87	0.87
16. – 18. GeV	0.76	0.81	0.85	0.87
14. – 16. GeV	0.75	0.79	0.83	0.87
12. – 14. GeV	0.73	0.78	0.81	0.87
11. – 12. GeV	0.72	0.77	0.81	0.88
10. – 11. GeV	0.72	0.77	0.81	0.90
9.5 – 10. GeV	0.72	0.78	0.82	0.93
9.0 – 9.5 GeV	0.72	0.78	0.84	0.95
8.5 – 9.0 GeV	0.69	0.78	0.86	1.00
8.0 – 8.5 GeV	0.69	0.78	0.88	1.06
7.5 – 8.0 GeV	0.68	0.73	0.95	0.85
7.0 – 7.5 GeV	0.68	0.72	0.77	0.86
6.5 – 7.0 GeV	Not used	0.71	0.78	0.87
6.0 – 6.5 GeV	Not used	0.71	0.79	0.89
5.5 – 6.0 GeV	Not used	0.70	0.83	0.83
5.0 – 5.5 GeV	Not used	0.71	0.77	0.81
4.0 – 5.0 GeV	Not used	Not used	0.75	Not used
1.0 – 4.0 GeV	Not used	Not used	0.73	Not used

Table B.18 Ratio of the transversely polarized ($\lambda_\theta = +1, \lambda_\phi = \lambda_{\theta\phi} = 0$) J/ψ cross-section the isotropically polarized J/ψ cross-section.

	J/ψ rapidity $0 - 0.75$	J/ψ rapidity $0.75 - 1.50$	J/ψ rapidity $1.50 - 2.00$	J/ψ rapidity $2.00 - 2.40$
40. – 70. GeV	1.07	1.05	1.07	1.00
30. – 40. GeV	1.08	1.09	1.06	1.06
22. – 30. GeV	1.13	1.11	1.08	1.09
18. – 22. GeV	1.16	1.13	1.10	1.12
16. – 18. GeV	1.19	1.14	1.12	1.18
14. – 16. GeV	1.22	1.15	1.14	1.20
12. – 14. GeV	1.24	1.16	1.18	1.25
11. – 12. GeV	1.27	1.18	1.22	1.29
10. – 11. GeV	1.31	1.18	1.24	1.35
9.5 – 10. GeV	1.34	1.17	1.27	1.36
9.0 – 9.5 GeV	1.41	1.15	1.28	1.33
8.5 – 9.0 GeV	1.35	1.10	1.31	1.32
8.0 – 8.5 GeV	1.38	1.03	1.39	1.34
7.5 – 8.0 GeV	1.46	1.24	1.45	1.72
7.0 – 7.5 GeV	1.62	1.24	1.49	1.66
6.5 – 7.0 GeV	Not used	1.23	1.61	1.82
6.0 – 6.5 GeV	Not used	1.15	1.78	1.90
5.5 – 6.0 GeV	Not used	1.17	1.98	1.84
5.0 – 5.5 GeV	Not used	1.23	1.98	2.81
4.0 – 5.0 GeV	Not used	Not used	2.76	Not used
1.0 – 4.0 GeV	Not used	Not used	2.91	Not used

Table B.19 Ratio of the transversely polarized ($\lambda_\theta = +1, \lambda_\phi = +1, \lambda_{\theta\phi} = 0$) J/ψ cross-section the isotropically polarized J/ψ cross-section.

	J/ψ rapidity $0 - 0.75$	J/ψ rapidity $0.75 - 1.50$	J/ψ rapidity $1.50 - 2.00$	J/ψ rapidity $2.00 - 2.40$
40. – 70. GeV	1.07	1.03	1.07	1.01
30. – 40. GeV	1.09	1.08	1.06	1.05
22. – 30. GeV	1.13	1.10	1.07	1.07
18. – 22. GeV	1.16	1.12	1.09	1.08
16. – 18. GeV	1.18	1.14	1.10	1.08
14. – 16. GeV	1.20	1.15	1.11	1.08
12. – 14. GeV	1.22	1.17	1.13	1.08
11. – 12. GeV	1.24	1.18	1.14	1.07
10. – 11. GeV	1.24	1.17	1.13	1.06
9.5 – 10. GeV	1.24	1.17	1.12	1.04
9.0 – 9.5 GeV	1.24	1.17	1.11	1.03
8.5 – 9.0 GeV	1.29	1.17	1.10	1.01
8.0 – 8.5 GeV	1.30	1.17	1.08	0.98
7.5 – 8.0 GeV	1.30	1.23	1.04	1.10
7.0 – 7.5 GeV	1.31	1.24	1.17	1.09
6.5 – 7.0 GeV	Not used	1.25	1.17	1.08
6.0 – 6.5 GeV	Not used	1.26	1.15	1.07
5.5 – 6.0 GeV	Not used	1.27	1.12	1.11
5.0 – 5.5 GeV	Not used	1.27	1.18	1.14
4.0 – 5.0 GeV	Not used	Not used	1.20	Not used
1.0 – 4.0 GeV	Not used	Not used	1.23	Not used

Table B.20 Ratio of the transversely polarized ($\lambda_\theta = +1, \lambda_\phi = -1, \lambda_{\theta\phi} = 0$) J/ψ cross-section the isotropically polarized J/ψ cross-section.

	J/ψ rapidity $0 - 0.75$	J/ψ rapidity $0.75 - 1.50$	J/ψ rapidity $1.50 - 2.00$	J/ψ rapidity $2.00 - 2.40$
40. – 70. GeV	1.10	1.05	1.07	1.01
30. – 40. GeV	1.12	1.08	1.04	1.04
22. – 30. GeV	1.12	1.10	1.06	1.05
18. – 22. GeV	1.15	1.12	1.07	1.04
16. – 18. GeV	1.17	1.14	1.08	1.00
14. – 16. GeV	1.19	1.16	1.08	0.99
12. – 14. GeV	1.21	1.18	1.08	0.97
11. – 12. GeV	1.21	1.18	1.07	0.93
10. – 11. GeV	1.18	1.18	1.04	0.90
9.5 – 10. GeV	1.16	1.19	1.01	0.86
9.0 – 9.5 GeV	1.13	1.21	0.98	0.85
8.5 – 9.0 GeV	1.24	1.29	0.94	0.82
8.0 – 8.5 GeV	1.23	1.46	0.89	0.78
7.5 – 8.0 GeV	1.19	1.25	0.82	0.84
7.0 – 7.5 GeV	1.11	1.27	0.97	0.83
6.5 – 7.0 GeV	Not used	1.31	0.92	0.78
6.0 – 6.5 GeV	Not used	1.53	0.85	0.75
5.5 – 6.0 GeV	Not used	1.45	0.79	0.80
5.0 – 5.5 GeV	Not used	1.40	0.85	0.73
4.0 – 5.0 GeV	Not used	Not used	0.77	Not used
1.0 – 4.0 GeV	Not used	Not used	0.81	Not used

BIBLIOGRAPHY

[1] D.W. Griffiths, *Introduction to Elementary Particles*, 1987, Westview Press.

[2] M.E. Peskin and D.V. Schroeder, *An Introduction to Quantum Field Theory*, 1995, Westview Press.

[3] C. Quigg, *Gauge Theories of the Strong, Weak, and Electromagnetic Interactions*, 1997, Westview Press.

[4] Particle Data Group, C. Amsler, et al., Review of Particle Physics, *Physics Letters B*, Vol. 667, Iss. 1–5, (2008).

[5] D.H. Perkins, *Introduction to High Energy Physics, 4^{th} edition*, 2000, Cambridge University Press.

[6] CDF Collaboration, F. Abe, et al., J/ψ and $\psi(2S)$ Production in $p\bar{p}$ Collisions at $\sqrt{s} = 1.8$ TeV, *Physical Review Letters*, Vol. 79, No. 4 (1997) 572–577.

[7] PHENIX Collaboration, A. Adare, et al., Ground and excited charmonium state production in $p + p$ collisions at $\sqrt{s} = 200$ GeV, *Phys. Rev. D, submitted*, arXiv:1105.1966v1.

[8] J-P. Lansberg, On the mechanisms of heavy-quarkonium hadroproduction, arXiv:0811.4005v1 [hep-ph].

[9] C.B. Mariotto, M.B. Gay Ducati, and G. Ingelman, Soft and hard QCD dynamics in hadroproduction of charmonium, *European Journal of Physics C*, 23 (2002) 527, arXiv:hep-ph/0111379.

[10] J-P. Lansberg, J/ψ, ψ' and Υ Production at Hadron Colliders: A Review, *International Journal of Modern Physics A*, Vol. 21, Nos. 19 & 20 (2006) 3857–3915.

[11] V. Barger, W.Y. Keung, and R.J.N. Phillips, Hadroproduction of ψ and Υ, *Zeitschrift für Physik C*, Particles and Fields 6, 169–174 (1980).

[12] CDF Collaboration, F. Abe, et al., J/ψ and $\psi(2S)$ production in $p\bar{p}$ collisions at $\sqrt{s} = 1.8$ TeV, *Physical Review Letters*, Vol. 79 (1997) 572.

[13] CDF Collaboration, F. Abe, et al., Production of J/ψ mesons from χ_c meson decays in $p\bar{p}$ collisions at $\sqrt{s} = 1.8$ TeV, *Physical Review Letters*, Vol. 79 (1997) 578;

[14] CDF Collaboration, F. Abe, et al., Quarkonia Production at CDF, *International Journal of Modern Physics A*, Vol. 12 (1997) 3867.

[15] D0 Collaboration, S. Abachi, et al., *Physics Letters B*, Vol. 370 (1996) 239, FERMILAB-Conf-96/249-E.

[16] C-H. Chang, Hadronic Production of J/ψ Associated with a Gluon, *Nuclear Physics B*, Vol. 172 (1979) 425.

[17] G. Bodwin, E. Braaten, G. Peter Lepage, Rigorous QCD Analysis of Inclusive Annihilation and Production of Heavy Quarkonium, *Physical Review D*, Vol. 51 (1995) 1125–1171, arXiv:hep-ph/9407339.

[18] M. Krämer, Quarkonium Production at High-Energy Colliders, *Prog. Part. Nucl. Phys.* Vol. 47 (2001) 141–201, arXiv:hep-ph/0106120.

[19] CDF Collaboration, F. Abe, et al., J/ψ, $\psi(2S)$ to μ^+ μ^- and B to J/ψ,$\psi(2S)$ Cross-Sections, Fermilab-Conf-94/136-E, arXiv:hep-ex/9412013.

[20] E. Braaten and S. Fleming, Color-Octet Fragmentation and the ψ' Surplus at the Tevatron, *Physical Review Letters* Vol. 74 (1995) 3327, arXiv:hep-ph/9411365.

[21] E. Braaten, B.A. Kniehl, and J. Lee, Polarization of Prompt J/ψ at the Tevatron, *Physical Review D* 62 (2000), arXiv:hep-ph/9911436.

[22] M. Cacciari, P. Nason, and R. Vogt, QCD Predictions for Charm and Bottom Quark Production at RHIC, *Physical Review Letters* Vol. 95 (2005) 122001, arXiv:hep-ph/0502203v1.

[23] M. Cacciari, M. Greco, and P. Nason, The p_T Spectrum in Heavy-Flavour Hadroproduction, *JHEP* 07 (1998) 9805, arXiv:hep-ph/9803400v1.

[24] M. Cacciari, S. Frixione, M. Mangano, P. Nason, and G. Ridolfi, QCD analysis of first b cross section data at 1.96 TeV, *JHEP* 07 (2004) 033, arXiv:hep-ph/0312132.

[25] M. Cacciari and P. Nason, Is There a Significant Excess in Bottom Hadroproduction at the Tevatron?, *Physical Review Letters* Vol. 89 (2002) 122003.

[26] M. Cacciari and P. Nason, Charm cross sections for the Tevatron Run II, *JHEP* 09 (2003) 06.

[27] V.G. Kartvelishvili, A.K. Likhoded, and V.A. Petrov, On the fragmentation functions of heavy quarks into hadrons, *Physical Review Letters B* 78 (1978) 615–617.

[28] CDF Collaboration, D. Acosta, et al., Measurement of the J/ψ Meson and b-Hadron Production Cross Sections in $p\bar{p}$ Collisions at $\sqrt{s} = 1960$ GeV, *Physical Review D* 71 (2005) 032001, arXiv:hep-ex/0412071.

[29] P. Faccioli, C. Lourenco, J. Seixas, and H.K. Wohri, Towards the Experimental Clarification of Quarkonium Production, *European Journal of Physics C*, 69 (2010) 657, arXiv:1006.2738/hep-ph.

[30] T. Taylor, Incident at the CERN LHC *Teion Kogaku*, 45 (2010) 344–351.

[31] L. Evans and P. Bryant, LHC Machine, *Journal of Instrumentation*, 3 (2008) S08001.

[32] The ATLAS Collaboration, G. Aad, et al., Luminosity Determination in pp Collisions at $\sqrt{s} = 7$ TeV using the ATLAS Detector at the LHC, *European Journal of Physics (submitted)*, arXiv:1101.2185v1 [hep-ex].

[33] The ATLAS Collaboration, G. Aad, et al., Updated Luminosity Determination in pp Collisions at $\sqrt{s} = 7$ TeV using the ATLAS Detector, ATLAS-CONF-2011-011.

[34] A. Martinez, Studies with Muons in ATLAS: TileCal Level-2 Trigger and MSSM Higgs Discovery Reach, Universitat de Valencia Thesis.

[35] The ALICE Collaboration, K. Aamodt, et al., The ALICE experiment at the CERN LHC, *Journal of Instrumentation*, 3 (2008) S08002.

[36] The ATLAS Collaboration, G. Aad, et al., The ATLAS experiment at the CERN LHC, *Journal of Instrumentation*, 3 (2008) S08003.

[37] The CMS Collaboration, S. Chatrchyan, et al., The CMS experiment at the CERN LHC, *Journal of Instrumentation*, 3 (2008) S08004.

[38] The LHCb Collaboration, A. Augusto Alves Jr, et al., The LHCb Detector at the LHC, *Journal of Instrumentation*, 3 (2008) S08005.

[39] K. Kleinknecht, *Detectors for Particle Radiation, second edition*, Cambridge University Press, 1998.

[40] G. Aad, et al., ATLAS pixel detector electronics and sensors, *JINST*, 3 (2008) P07007.

[41] John Joseph, et al., ATLAS Silicon ReadOut Driver (ROD) Users Manual, *http://www-eng.lbl.gov/ jmjoseph/Atlas-SiROD/Manuals/.*

[42] ATLAS Collaboration, T. Vickey, et al., A read-out driver for silicon detectors in ATLAS, 12^{th} *Workshop on Electronics for LHC and Future Experiments (LECC 2006).*

[43] ATLAS Collaboration, K. Einsweiler, ATLAS On-detector Electronics Architecture, Internal Report.

[44] M. Mathes, Development and Charaterization of Diamond and 3D-Silicon Pixel Detectors with ATLAS-Pixel Readout Electronics, Bonn University Thesis, BONN-IR-2008-15.

[45] J. Biesiada, J. Dopke, H.M. Gray, S-C. Hsu, P.D. Jackson, A. Korn, A. Nelson, K. Schmieden, A. Schreiner, J.S. Virzi, M. Wittgen, The Implementation and Performance of ROD DSP Software in the ATLAS Pixel Detector, *ATL-INDET-INT-2010-006.*

[46] Texas Instruments, TMS320C6201 fixed-point digital signal processor review H, *Literature Number: SPRS051H.*

[47] Texas Instruments, TMS320C6713 floating-point digital signal processor review L, *Literature Number: SPRS186L.*

[48] D. Salvatore, et al., The GNAM system in the ATLAS online monitoring framework, *Nucl. Physics B* 172 (2007) 317–320.

[49] The ATLAS Collaboration, G. Aad, et al., Measurement of the differential cross-sections of inclusive, prompt and non-prompt J/ψ production in proton-proton collisions at $\sqrt{s} = 7$ TeV, *Nuclear Physics B*, Vol. 850, Iss. 3, (2011) 387–444, arXiv:1104.3038v1.

[50] The ATLAS Collaboration, G. Aad, et al., Measurement of the differential cross-sections of inclusive, prompt and non-prompt J/ψ production in proton-proton collisions at $\sqrt{s} = 7$ TeV: Internal ATLAS Note, *ATL-COM-PHYS-2010-1035.*

[51] H. Burkhardt and P. Grafstrom, Absolute Luminosity from Machine Parameters, LHC-PROJECT-Report-1019, 2007.

[52] W. Kozanecki, et al., Interaction-Point Phase-Space Characterization using Single-Beam and Luminous-Region Measurements at PEP-II, Nucl. Instrum. Meth. A607 (2009) 293–321.

[53] T. Sjostrand, S. Mrenna, P.Z. Skands, PYTHIA 6.4 Physics and Manual, *JHEP*, 0605 (2003) 026, arXiv:hep-ph/0603175.

[54] The ATLAS Collaboration, G. Aad, et al., ATLAS Monte Carlo tunes for MC09, ATL-PHYS-PUB-2010-002, CERN, Geneva, Mar. (2010).

[55] A. Sherstnev and R.S. Thorne, Parton Distributions for LO Generators, *European Journal of Physics*, 55 (2008) 553, arXiv:0711.2473 [hep-ph].

[56] The ATLAS Collaboration, G. Aad, et al., The ATLAS Simulation Infrastructure, *European Journal of Physics*, 70 (2010) 823, arXiv:1005.4568 [physics.ins-det].

[57] P. Nason, et al., Bottom Production, *1999 CERN Workshop on SM Physics (and more) at the LHC*, arXiv:hep-ph/0003142.

[58] F. James, MINUIT Reference Manual, CERN Program Library Long Writeup D506.

[59] D. Froidevaux and P. Sphicas, General-Purpose Detectors for the Large Hadron Collider, *Annual Review of Nuclear and Particle Science* Vol. 56 (2006) 375–440.

[60] The ATLAS Collaboration, G. Aad, et al., A measurement of ATLAS muon efficiency using J/ψ decays, ATLAS-CONF-2011-021, CERN, Geneva, Mar. (2011).

[61] The CMS Collaboration, V. Khachatryan, et al., Prompt and non-prompt J/ψ production in pp collisions at $\sqrt{s} = 7$ TeV, CMS-BPH-10-002, arXiv:1011.4193 [hep-ex].

[62] V. Kostyukhin, VKalVrt - package for vertex reconstruction in ATLAS, ATL-PHYS-2003-031.

[63] CDF Collaboration, T. Aaltonen, et al., Polarizations of J/ψ and $\psi(2S)$ Mesons Produced in $p\bar{p}$ Collisions at 1.96 TeV, *Physical Review Letters* Vol. 99 (2007) 132001, arXiv:0704.0638 [hep-ex].

[64] CDF Collaboration, D. Acosta, et al., Measurement of the J/ψ Meson and b-hadron Production Cross-Sections in $p\bar{p}$ Collisions at $\sqrt{s} = 1960$ GeV, *Physical Review D* 71 (2005) 032001, arXiv:hep-ex/0412071.

[65] M. Cacciari, M. Greco, and P. Nason, The p_T Spectrum in Heavy-Flavour Hadroproduction, *JHEP* 9805 (1998) 007, arXiv:hep-ph/9803400.

[66] M. Cacciari, M. Greco, and P. Nason, The p_T Spectrum in Heavy-Flavour Photoproduction, *JHEP* 0103 (2001) 006, arXiv:hep-ph/0102134.

[67] J. Pumplin, D.R. Stump, J. Huston, H.L. Lai, P.M. Nadolsky, and W.K. Tung, New Generation of Parton Distribution with Uncertainties from Global QCD Analysis, *JHEP* 0207 (2002) 012, arXiv:hep-ph/0201195.

[68] A.D. Frawley, T. Ullrich, R. Vogt, Heavy flavor in heavy-ion collisions at RHIC and RHIC II, *Phys. Rept* 462 (2008) 125–175, arXiv:0806.1013 [hep-ph].

[69] P. Artoisenet, J.M. Campbell, J-P. Lansberg, F. Maltoni, and F. Tramontano, Upsilon production at the Tevatron and the LHC, *Physical Review Letters* Vol. 101 (2008) 152001, arXiv:0806.3282 [hep-ph].

[70] N. Brambilla, et al., Heavy quarkonium: progress, puzzles, and opportunities, *European Journal of Physics C* 71 (2011) 1534, arXiv:1010.5827 [hep-ph].

[71] LHCb Collaboration, A. Augusto Alves Jr, et al., Measurement of the J/ψ production cross-section at $\sqrt{s} = 7$ TeV in LHCb, *35th International Conference on High Energy Physics*, LHCb-CONF-2010-010.

[72] ATLAS Collaboration, A. Korn, $J/\psi \to \mu\mu$ from 7 TeV pp collisions in ATLAS: performance with first data, *35th International Conference on High Energy Physics*, ATL-PHYS-PROC-2011-005.

[73] ATLAS Collaboration, G. Aad, et al., Expected Performance of the ATLAS Experiment, Detector, Trigger, and Physics, arXiv:0901.0512v4 [hep-ex], CERN-OPEN-2008-020.

[74] ATLAS Collaboration, G. Aad, et al., Measurement of the $\Upsilon(1S)$ Production Cross-Section in pp Collisions at $\sqrt{s} = 7$ TeV in ATLAS, *Physics Letters B (submitted)*, arXiv:1106.5325v1 [hep-ex].

[75] CERN Press Release, http://press.web.cern.ch/press/PressReleases/Releases2011/PR06.11E.html.

[76] CERN Press Release, http://press.web.cern.ch/press/PressReleases/Releases2011/PR02.11E.html.

[77] CERN Press Release, http://press.web.cern.ch/press/PressReleases/Releases2011/PR01.11E.html.